

## 国際化推進共同研究概要

No. 1

21EA-1

タイトル : Dynamical mechanisms of stratospheric control on the tropical troposphere and ocean

研究代表者 : UEYAMA Rei

所内世話人 : 江口 菜穂

研究概要 : 2019年9月初旬、南半球極域で成層圏突然昇温（SSW）イベントが発生しました。このイベントは、南半球極渦の崩壊には至りませんでしたが、成層圏の南北循環を大幅に強化し、熱帯湧昇を増加させ、熱帯下部成層圏の気温を低下させました。本研究課題から、この SSW によって太平洋と大西洋での熱帯暴風とサイクロンの発達を含む、熱帯対流活動が強化されたことがわかりました。特に大西洋上で急速に発達した熱帯低気圧Dorian が SSW 前後で急速に発達する様子を、高鉛直分解能な雲データを用いて、明らかにしました。

# Dynamical Mechanisms of Stratospheric Control on the Tropical Troposphere and Ocean

Rei Ueyama (NASA Ames Research Center)

## I. Abstract

In early September 2019, a large stratospheric sudden warming (SSW) event occurred in the southern hemisphere (SH) polar region. This event did not lead to a breakdown of the SH polar vortex, but significantly enhanced the stratospheric Brewer-Dobson circulation with increased tropical upwelling and thus decreased temperatures in the tropical lower stratosphere. In this observational study, we find that tropical convective activity was enhanced due to this SSW, including the development of tropical storms and cyclones over the Pacific and Atlantic ocean basins.

## II. Introduction

Stratospheric sudden warming (SSW) events have been known to increase the stratospheric mean meridional circulation (also known as the Brewer-Dobson circulation) with enhanced upwelling in the tropics. Cooling of the tropical lower stratosphere associated with enhanced tropical upwelling destabilizes the tropical tropopause layer (TTL) and supports the development of deep tropical convection and cyclones (Kodera et al., 2015; Eguchi et al., 2015). A statistical relationship between northern hemisphere (NH) SSW events and tropical cyclones in the summer southern hemisphere (SH) has been demonstrated recently in large ensemble mean numerical experiments (Yoshida and Mizuta, 2021). They showed that SSW-induced cooling of the tropical stratosphere results in increased convective precipitation over tropical cyclone genesis regions (e.g., South China Sea, eastern tropical Pacific, Caribbean Sea).

In this study, we demonstrate how and to what extent tropical cyclone activity was impacted by the strong SSW in September 2019.

## III. Method/Data

We analyzed JRA-55 reanalysis data, NOAA outgoing longwave radiation (OLR) data, surface precipitation measurements from Global Precipitation Climatology Project (GPCP), and satellite-derived global convective cloud top altitudes (Pfister et al, 2022). Our approach for calculating the convective cloud top altitudes is based on the assumption that rainfall, properly thresholded, can define the area where convection is occurring. These rainfall data, coupled with the infrared satellite information, can then define both the regions where the mass-transporting convective cores occur, and their altitude.

## IV. Results

The longitudinal variation in upwelling along 10°–20°N associated with the 2019 SSW is illustrated in Figure 1. Tropical temperatures decreased in the upper stratosphere at the end of August 2019, coincident with the start of the SSW. At this initial stage, cooling in the tropical stratosphere has not yet reached down to the 100 hPa level. During this time, anomalously low temperatures are located over limited areas of South China Sea and the Pacific where convection is

active (as indicated by low OLR values). Tropical stratospheric cooling extends downward to the tropopause level in early September over the ascending branch of the Hadley circulation. At this time, upwelling in the troposphere also increases (Fig. 1b). Furthermore, longitudinal variations in 100 hPa temperatures appear to correspond to variations in convective activity in the northern tropics ( $10^{\circ}$ – $25^{\circ}$ N).

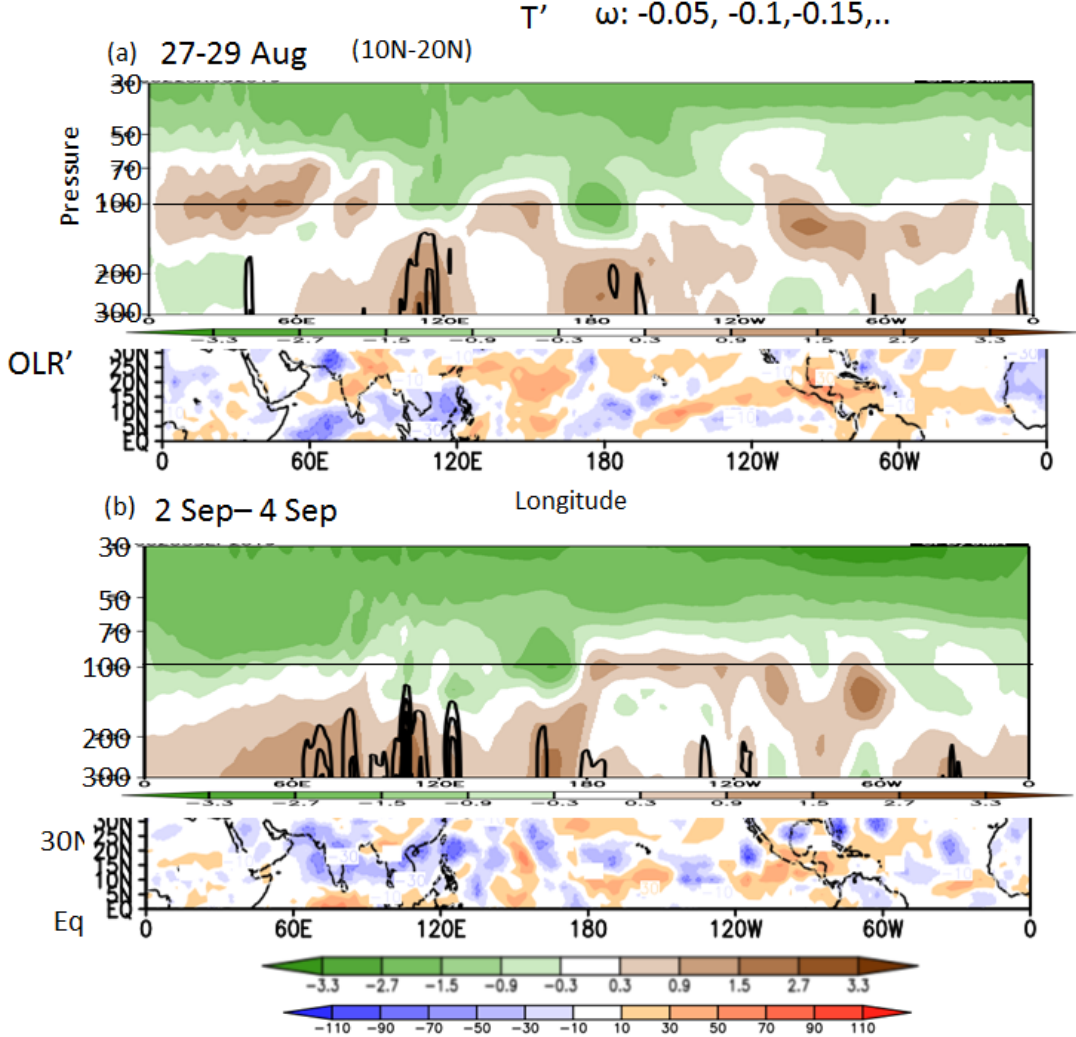


**Figure 1: (a)** Top panel shows the 3-day (27-29 August) mean height-longitude section of anomalous temperature (color shading) and pressure velocity averaged over  $10$ – $20^{\circ}$ N. Bottom panel shows the 3-day mean OLR field in the northern tropics. **(b)** Same as (a) but for 2-4 September mean.

The longitude-time section of anomalous OLR and relative vorticity at 850 hPa averaged over  $15$ – $25^{\circ}$ N shown in Figure 2 illustrates a coherent and rapid change in convective activity around 1 September. Convection organizes into tropical disturbances and cyclones, which move westward over the Pacific and Atlantic Ocean sectors in September.

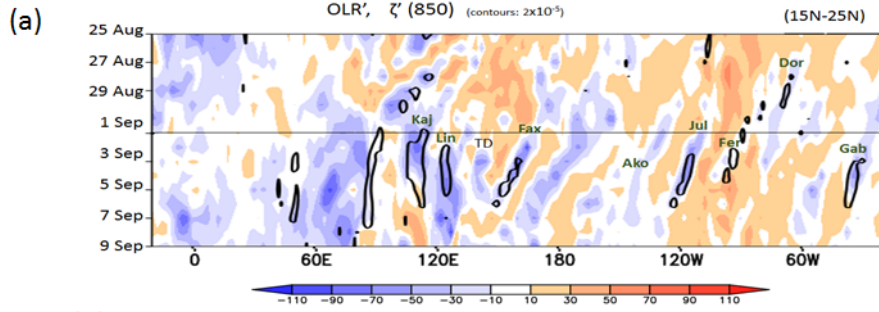


**Figure 2: Longitude-time section of anomalous OLR and relative vorticity at 850 hPa averaged over 15-25°N.**

A clear example of the impact of stratospheric temperatures on tropical cyclone activity was seen in the case of hurricane Dorian, which generated over the Caribbean Sea on 24 August. The relationship between tropical stratospheric cooling and the development of hurricane Dorian is illustrated in Figure 3. While the cyclone initiation occurred prior to the development of SSW, hurricane intensity increased from category 4 to 5 between 1 and 2 of September, coinciding with timing of rapid cooling of the tropical lower stratosphere over the Caribbean Sea. At this time, strong enhancement in the upwelling is observed at the 125 hPa level. There is remarkable agreement between the temporal variations in 125 hPa pressure velocity and in the occurrence of deep ( $>14$  km) convective cloud top height throughout this period. The distribution of convective cloud top height indicates that the enhanced upwelling occurred in association with the increase in clouds reaching the TTL (cloud top pressure higher than 140 hPa). It is also worth noting that the diurnal cycle in cloud top height is significant before 29 August, but non-diurnal variations increase in early September.

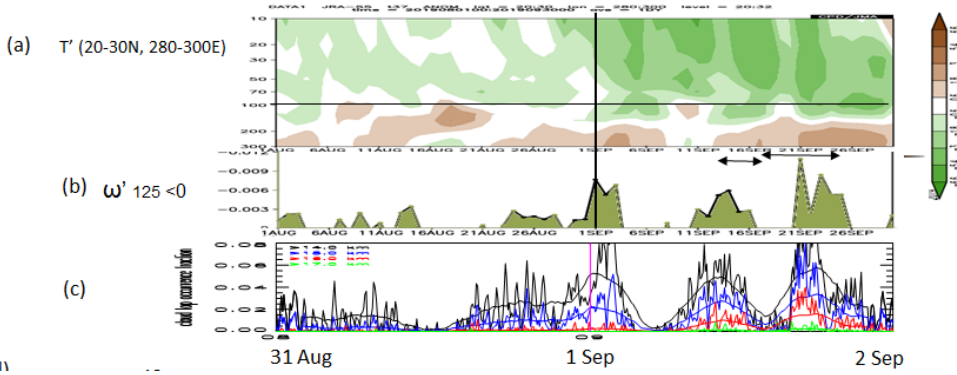


**Figure 3: Time-height sections of (a) temperature anomalies and (b) pressure velocity anomalies at 125 hPa averaged over the Caribbean region (80W-60W, 20-30N). (c) Convective cloud top occurrence fraction over the same domain as (a) and (b).**

## V. Discussion/Summary

In this study, we found that the SSW event in September 2019 was associated with an increase in deep tropical convective activity along the ascending branch of the Hadley circulation in the NH over 10°–25°N. Here we showed an example of the SSW impact on the intensification of a tropical cyclone over the Caribbean Sea. Similar examples were also found over other ocean basins in the northern tropical latitudes such as the Pacific, India and African sectors. This impact of SSW on deep convective activity and tropical cyclones along the ascending branch of the Hadley circulation is similar to that found in association with other strong SSW events in the northern polar regions (e.g., January 2009 and 2010; Kodera et al., 2015). We have shown that the influence of stratospheric cooling first manifests itself on the deep convection penetrating into the TTL. The difficulty in simulating the intensification of hurricane Dorian in many models (Ryglicki et al., 2021) may be related to model deficiencies in simulating the connection between tropical deep convection and the large-scale stratospheric circulation.

## VI. References

- Eguchi, N., K. Kodera, and T. Nasuno, 2015: A global non-hydrostatic model study of a downward coupling through the tropical tropopause layer during a stratospheric sudden warming, *Atmos. Chem. Phys.*, **15**, 297-304, doi:10.5194/acp-15-297-2015.
- Kodera, K., B. M. Funatsu, C. Claud, and N. Eguchi, 2015: The role of convective overshooting clouds in tropical stratosphere-troposphere dynamical coupling, *Atmos. Chem. Phys.*, **15**, 6767-6774, doi:10.5194/acp-15-6767-2015.
- Kodera, K., N. Eguchi, R. Ueyama, Y. Kuroda, C. Kobayashi, B.M. Funatsu, and C. Claud, 2019: Implication of tropical lower stratospheric cooling in recent trends in tropical circulation and deep convective activity. *Atmos. Chem. Phys.*, **19**, 2655-2669, doi:10.5194/acp-19-2655-2019.
- Pfister, L., Ueyama R., Jensen E., and Schoeberl, M., 2022: A method for obtaining high frequency, global, IR-based convective cloud tops for studies of the tropical tropopause layer, in preparation.
- Ryglicki, D. R., Velden, C. S., Reasor, P. D., Hodyss, D., & Doyle, J. D., 2021: Observations of Atypical Rapid Intensification Characteristics in Hurricane Dorian (2019), *Monthly Weather Review* (published online ahead of print 2021). <https://journals.ametsoc.org/view/journals/mwre/aop/MWR-D-20-0413.1/MWR-D-20-0413.1.xml>.
- Yoshida, K., & Mizuta, R., 2021: Do sudden stratospheric warmings boost convective activity in the tropics? *Geophysical Research Letters*, **48**, e2021GL093688. <https://doi.org/10.1029/2021GL093688>.

## **VII. List of Publications**

- Kodera, K., Eguchi, N., Ueyama, R., Funatsu, B., Gaetani, M., and Taylor, C. (2021), The impact of tropical tropopause cooling on Sahelian extreme deep convection, *J. Meteor. Soc. Japan*, 99,  
<https://doi.org/10.2151/jmsj.2021-055>.

## **VIII. Research meeting and discussion**

Several virtual meetings (participants: Rei Ueyama, Nawo Eguchi, and Kunihiko) were help to discuss the relationship between sudden stratospheric warmings and tropical cyclones, and NICAM simulation results of the stratosphere-troposphere exchange mechanism.

## **IX. Additional information**

Rei Ueyama is still on a reduced work schedule due to COVID-19 caregiving. NASA has granted excused leave to employees with COVID-19 caregiving responsibilities through the end of January 2022. All travel is still restricted so meeting in person was not possible this past year. However, we have maintained communication via email and virtual meetings. We have used the funds to purchase a data server for storing and archiving our research data.

## **X. Other members of the joint research team**

Nawo Eguchi	RIAM, Kyushu University
Kunihiko Kodera	Meteorological Research Institute

## 国際化推進共同研究概要

No. 2

21NU-1

タイトル : Numerical simulation of EC and EBW in QUEST

研究代表者 : BERTELLI Nicola

所内世話人 : 出射 浩

研究概要 :

QUEST では3年間で閉じ込め磁場を 0.25 T から 0.5 T に増強する計画を進めている。0.5 T では現在、非誘導電流立ち上げ実験に用いられている 28 GHz ECH システムを用い、第二高調波中心加熱が行えるようになる。加えて内側に基本波加熱共鳴層が存在する。低密度、高密度プラズマにおける 0.5 T 実験時の基本波加熱・第二高調波加熱による入射ビームの 1 回通過吸収が評価された。有効なアップシフト共鳴で高効率な電流駆動が見込める。また、Petra-M により有限要素シミュレーションも進められている。

## Numerical simulation of EC and EBW in QUEST

BERTELLI Nicola

(Princeton University, U.S.A)

Extra-ordinary mode fundamental ( 1<sup>st</sup> ) and second ( 2<sup>nd</sup> ) harmonic heating scenario has been considered for the 0.5 T ECHCD experiment, based on the ray tracing analysis. Figure 1 shows ray trajectories at top view and transmitted power evolution along ray propagation with parallel refractive indexes  $N_{\parallel a} = 0.15, 0.25$  and  $0.35$  in low density plasma. Bulk (with  $T_{eb0} = 0.5$  keV) and highly energetic (with  $T_{eh0} = 60$  keV) electron components are taken into consideration in the ray tracing. The incident ray from the low field side (LHS) starts to be damped as third harmonic absorption of the energetic electron, and is damped as 2<sup>nd</sup> harmonic absorption of energetic and bulk electrons. In addition, it is damped as 1<sup>st</sup> absorption when it come closer to the Doppler shifted resonance, and reflected back outside due to the cutoff. The total single pass absorption reaches to 80-90 %.

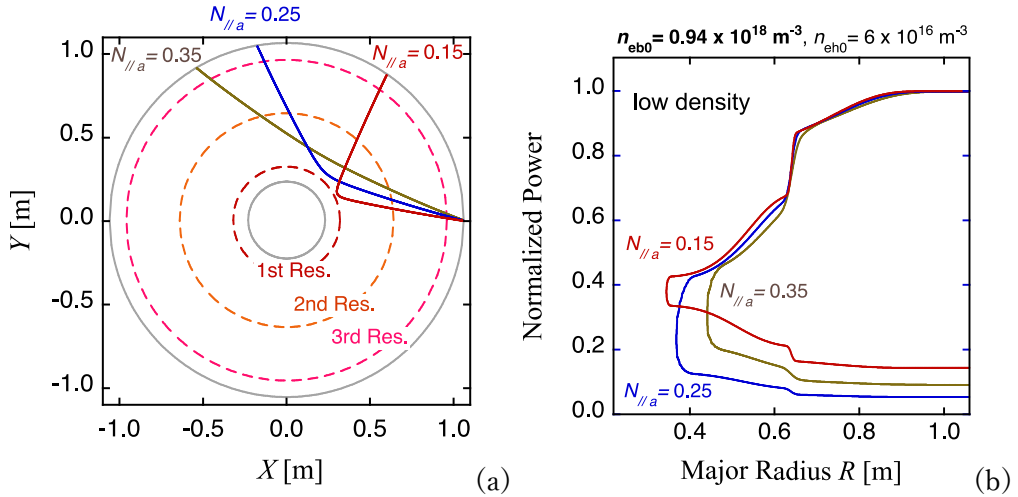


Fig.1 (a) Ray trajectories at top view and (b) transmitted power evolution along ray propagation with parallel refractive indexes  $N_{\parallel a} = 0.15, 0.25$  and  $0.35$  in low density plasma. At the top view of (a), fundamental (1<sup>st</sup> ), second (2<sup>nd</sup> ) and third (3<sup>rd</sup> ) resonance field radii are shown.

In high density case, it reflected back outside before coming to the 1<sup>st</sup> absorption area. Figure 2 shows ray trajectories at top view and the transmitted power evolution along ray

propagation with parallel refractive indexes  $N_{\parallel a} = 0.15, 0.25$  and  $0.35$  in high density plasma. Here two (bulk and highly energetic) electron components are also considered as in the low-density case. The ray is strongly damped as 2<sup>nd</sup> harmonic resonance in the absorption area of the bulk electrons. The resonance area for the energetic electrons strongly shifts to the high field side (HFS) due to the relativistic effect and expands to both of the HFS and LHS sides due to the Doppler shift effect. The strong damping results from the up-shifted resonance absorption of the highly energetic electrons due to the Doppler shift effect as well as the bulk electron absorption. The non-inductive plasma current driven by the ECHCD will be evaluated with the Fokker-Planck code.

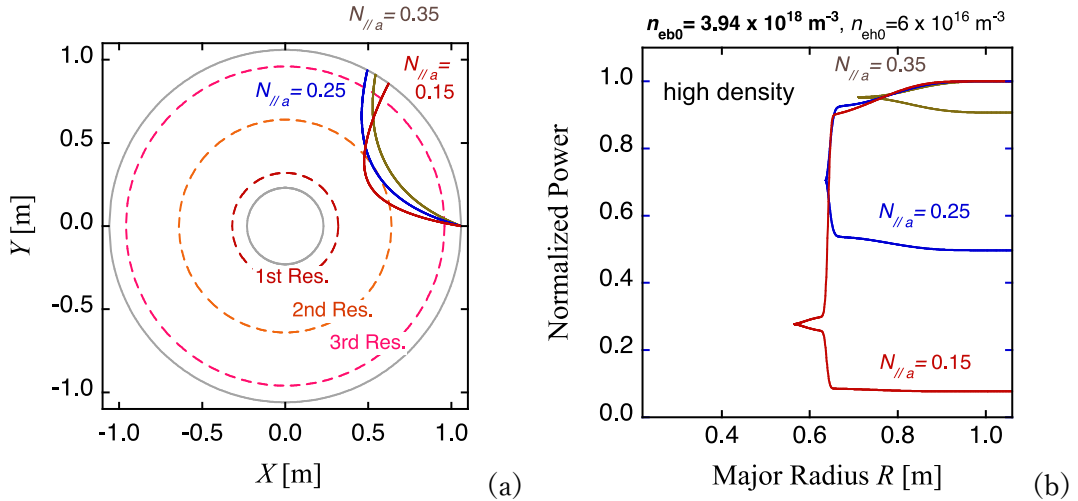


Fig.2 (a) Ray trajectories at top view and (b) transmitted power evolution

along ray propagation with parallel refractive indexes  $N_{\parallel a} = 0.15, 0.25$  and  $0.35$

Full 3D NSTX-U device geometry including realistic antenna geometry and 3D scrape-off-layer (SOL) plasma is also modeled to simulate NSTX-Upgrade plasmas using Petra-M finite-element-method (FEM). The antenna geometry and the 3D NSTX-U geometry are from the NSTX-U CAD models. Petra-M code is a state-of-the-art generic electromagnetic simulation tool for modelling RF wave propagation based on MFEM [<http://mfem.org>], open-source scalable C++ finite element method library. In Kyushu University, a commercial software of COMSOL has been prepared for FEM simulations.

## 国際化推進共同研究概要

No. 3

21NU-2

タイトル：Design of Electron Cyclotron Emission Diagnostic for Electron Temperature and its Fluctuation Measurements

研究代表者：SUNG Choongki

所内世話人：文 賛鎬

### 研究概要：

トカマク装置 PLATO における新プラズマ診断法として電子サイクロトロン放射(ECE)と相関ECE(CECE)計測の実現可能性を調べた。実際 PLATO の放電パラメータの代わりに、持永らによる輸送研究の平衡値で放物線状の空間分布を仮定した。即ち、 $B_T = 0.3 \text{ T}$ 、 $T_e = 130 \text{ eV}$ 、 $n_e = 1 \times 10^{19} \text{ m}^{-3}$  の値を用いて最初にプラズマのアクセス可能性を決定した。また、アクセス可能な周波数の総光学的厚さ ( $\tau_m$ ) を計算した。PLATO プラズマは、基本波 0 モードと第 2 高調波 X モードの両方でアクセス可能なすべての周波数にわたってアクセス可能な外層の深さが薄く、光学的厚さが  $\tau_m < 1$  の低密度であると判断した。これは、ECE/CECE が現在 PLATO の診断法として実行可能ではないことを示した。一方、アクセシビリティと  $\tau_m$  値を改善するために必要な  $B_T$  と  $T_e$  値をシミュレーションした。その結果、PLATO トカマクは ECE/CECE 測定には  $B_T$  を約 1.1 T まで、 $T_e$  を最大 1 KeV まで増やす必要があることが分かった。従って、ECE/CECE 測定のためには、デバイスアップグレードして  $T_e$  と  $B_T$  を増やす必要があると考えられた。

## CECE Feasibility for PLATO Tokamak

Pocholo Nebres, Choongki Sung

Fusion and Plasma Dynamics Laboratory, KAIST, Daejeon, ROK

Correlation electron cyclotron emission or CECE, is a plasma diagnostic technique which allows for the measurement of small amplitude ( $\sim 1\%$ ) temperature fluctuations which can be masked by thermal noise, in addition to the ability to measure local electron temperature. These small amplitude fluctuations are often believed to be related to turbulent transport in fusion plasmas [1]. This study aims to determine the feasibility of CECE for use as a diagnostic system for the PLATO tokamak.

For the study, a simulation was done using code written in Python. The accessibility of the plasma created in the simulation is first checked. The total optical depth of the accessible frequencies for the fundamental ordinary mode and 2<sup>nd</sup> harmonic extraordinary mode is then determined to check whether the plasma has sufficient optical thickness for use in CECE or not.

The ordinary mode cyclotron frequencies are cut off when the cyclotron frequency is less than the plasma frequency ( $\nu_c < \nu_p$ ). As such, only the cyclotron frequencies greater than or equal to the plasma frequencies can be detected in CECE, assuming that the detector views the plasma from the outboard edge. For the extraordinary mode frequencies, the signal cutoffs occur when the frequency is greater than the hybrid frequency  $\nu_h$  and less than the right-hand cutoff  $\nu_r$  (or  $\nu_h < \nu < \nu_r$ ). The signal also experiences a cutoff when the frequency is less than the left-hand cutoff frequency  $\nu_l$  [1].

The plasma parameters used for the calculations are:  $B_T = 0.3$  Tesla,  $T_e = 130$  eV, and  $n_e = 1 \times 10^{19} \text{ m}^{-3}$ . These values are the literature values for a simulation of equilibrium conditions by the PLATO team [2]. A parabolic decay of off-center values has been assumed to account for the spatial variation of the plasma parameters. Plasma center values have a factor of 1.0 to reflect the literature values.

The accessibility was first determined. CECE feasibility was then determined by using the total optical depth of the accessible region for the ordinary and extraordinary mode waves. The desired optical depth should be  $\tau_m \gg 1$  so that the measured temperature is the blackbody/local electron temperature [1].

Plasma parameter values and center frequencies are shown in Table 1 and Table 2, respectively.

**Tab. 1** Plasma Center Parameters

$T_e$ (eV)	130
$n_e$ ( $\text{m}^{-3}$ )	$1 \times 10^{19}$
$B_T$ (Tesla)	0.3
Minor Radius ( $a$ ; mtr)	0.18
Major Radius ( $R_0$ ; mtr)	0.7

**Tab. 2** Plasma Frequencies at  $r/a = 0$  (in GHz)

$\nu_c$	8.4	$\nu_h$	29.6
$2\nu_c$	16.8	$\nu_p$	28.4
$3\nu_c$	25.2	$\nu_L$	24.2
		$\nu_R$	32.6

**Tab. 3** Optical Depth  $\tau_m$  Data for  $m = 1$  and  $m = 2$

Fundamental Ordinary Mode ( $m = 1$ )	
$\tau_m$ Range	$0.0002 \rightarrow 0.0027$
Accessible Frequencies	6.68 → 6.72 GHz
Accessible $r/a$	0.97 → 1.0

**2<sup>nd</sup> Harmonic Extraordinary Mode ( $m = 2$ )**

2 <sup>nd</sup> Harmonic Extraordinary Mode ( $m = 2$ )	
$\tau_m$ Range	$0.002 \rightarrow 0.023$
Accessible Frequencies	13.36 → 13.52 GHz
Accessible $r/a$	0.94 → 1.0

Figure 1 shows the accessibility plot for the plasma parameters used in the simulation. The accessible frequencies for the ordinary and extraordinary modes are marked along with the frequency range that can be detected. The x-axis is the plasma  $r/a$  parameter, ranging from -1 to +1, with  $r/a = 0$  as the plasma center and - and + indicate high and low field side, respectively. Only the low field side is shown starting from  $r/a = 0.8 - 1.0$  since the accessible window for both modes is very narrow, only to within 6% distance from the plasma outer layer. In the accessible frequency range, the total optical depth range for the ordinary mode fundamental frequencies is  $\tau_m = 0.0002 - 0.0027$  while for the  $m = 2$  extraordinary mode frequencies the total optical depth range is  $\tau_m = 0.002 - 0.023$ . Optical thickness values of less than 1 are defined as optically thin [1]. These are summarized in Table 3.

The small  $B_T$  value contributes to the small accessible window as it is directly proportional to the cyclotron frequency. The high electron density also produces a high plasma frequency. These two factors generate a plasma with large cutoff regions and small accessible windows.

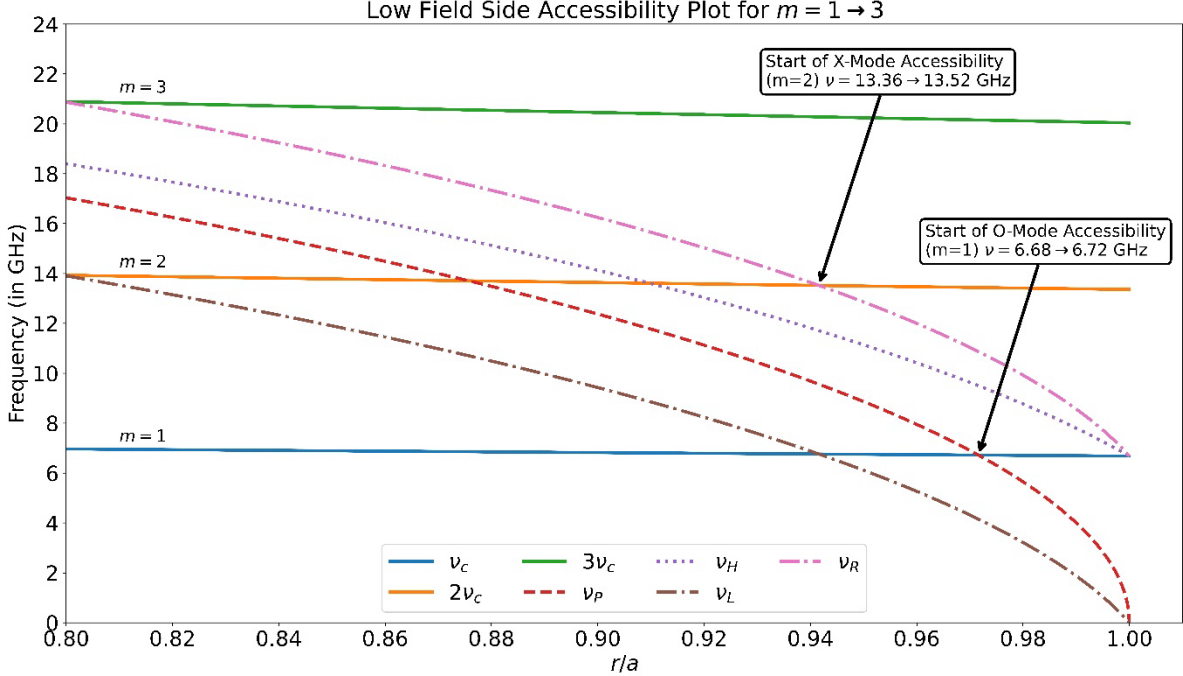


**Fig. 1** Accessibility plot for the simulated PLATO plasma. Only the low-field side accessibility is presented due to the narrow accessible layer (last ~6% outer layer depth of the plasma).

The total optical depth for either mode is much less than 1 for the simulated parameters, indicating that the plasma is optically thin at the accessible outer layer regions. For optically thin plasmas, additional consideration must be taken to account for the refraction of the ECE ray through the plasma [1], since the signal is not well-localized compared to an optically thick case where the intensity observed is directly related to the local electron temperature. Since the absorption coefficient and the total optical depth are position-dependent ( $\omega_p$  and  $\Omega(s)$ ), regardless of the frequency and position that could be observed, the optical depth will be less than 1, signifying an optically thin plasma. The plasma created in PLATO using the simulated conditions is called an ‘over-dense plasma’.

The plasma parameters can be changed such that there is full accessibility on the low field side for both the X- and O-mode frequencies. Increasing the  $B_T$  to 1.1T allows for full accessibility of the plasma across all frequencies. The increased  $B_T$  shifts the cyclotron frequency of the plasma and its harmonics upward to above the corresponding cutoffs as shown in figure 2. Since the absorption coefficient and the total optical depth are directly proportional to  $T_e$ , increasing the temperature will also increase  $\tau_m$ . Figure 3 shows the total optical depth plot of several  $T_e$  values with  $B_T = 1.1\text{T}$  and the density kept at the original value of  $n_e = 1 \times 10^{19} \text{ m}^{-3}$ . “Optically thick” is defined as having  $\tau_m \gg 1$  [1], but a value of at least  $\tau_m = 2$  is usually acceptable for use in CECE. For ECE, a value of at least  $\tau_m = 1$  is also acceptable. Increasing the  $T_e$  to 1 KeV increases the optical depth of the plasma to around  $\tau_m = 1$  for the fundamental O-mode wave from the center of the plasma to around  $r/a = 0.35$ . This mode is acceptable for use only in ECE, since the optical depth is around 1. For the 1 KeV 2<sup>nd</sup> harmonic X-mode wave,  $\tau_m$  ranges from 2 ~ 3 from the plasma center to  $r/a = 0.5$ . The 2 KeV fundamental O-mode wave is optically thick with  $\tau_m = 2 - 2.3$  from the plasma center to  $r/a \sim 0.35$  and the 2 KeV 2<sup>nd</sup> harmonic X-mode and the 5 KeV fundamental O-mode waves are optically thick, with  $\tau_m$  ranging from 2 – 6, in the low-field side of the plasma up to around  $r/a = 0.7$  from the center of the plasma. The 5 KeV 2<sup>nd</sup> harmonic X-mode wave has acceptable optical depth, with  $\tau_m$  ranging from 2 – 14, at up to around  $r/a = 0.8$  from the center of the plasma. Increasing the magnetic field and temperature parameters to  $B_T = 1.1$  Tesla and  $T_e = 1$  KeV are sufficient to enable ECE and CECE diagnostics in PLATO.

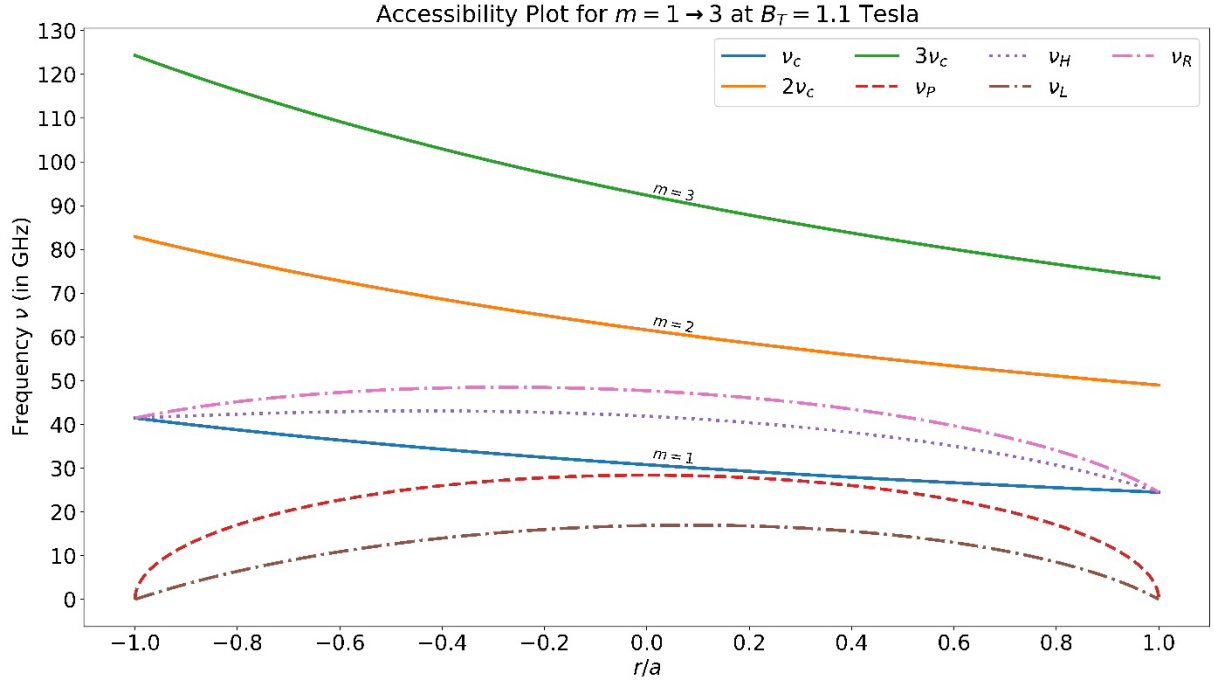


**Fig. 2** Accessibility plot for the first three harmonics when  $B_T$  is increased to 1.1 Tesla and all other parameters are maintained. All frequencies are accessible; no frequency is cut off. The following plasma parameters were used:  $B_T = 1.1$  T,  $n_e = 1 \times 10^{19}$  m $^{-3}$ , and  $T_e = 130$  eV.

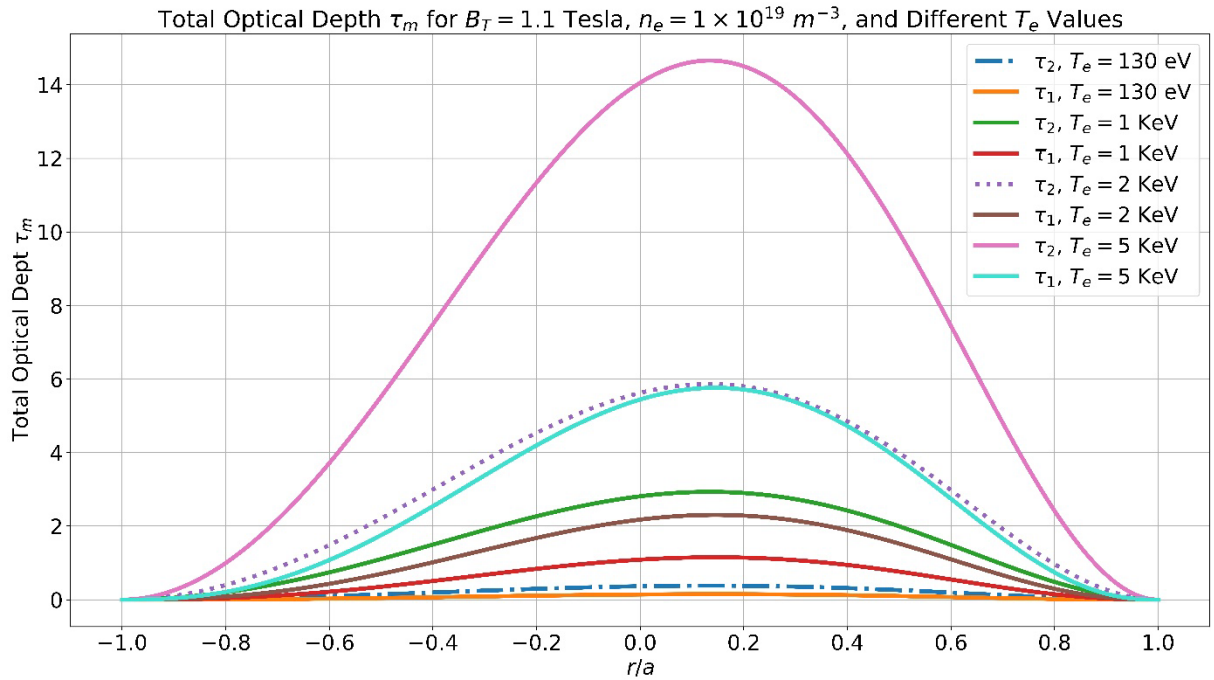


**Fig. 3** Total optical depth  $\tau_m$  vs.  $r/a$  plot for several values of  $T_e$ . The absence of discontinuities in the plot indicates full accessibility of the harmonic frequencies. The following values were used for the  $B_T$  and  $n_e$  parameters:  $B_T = 1.1$  Tesla,  $n_e = 1 \times 10^{19}$  m $^{-3}$ .

The current PLATO parameters produce an over-dense plasma which makes it not suitable for ECE and CECE measurements. The researchers would like to suggest to the PLATO team to consider increasing the toroidal magnetic field and the plasma temperature in any planned future upgrades to PLATO, so that CECE diagnostic can also be employed as one of its diagnostic techniques.

## **REFERENCES**

- [1] Hutchinson, I. (2002). Principles of Plasma Diagnostics (2nd ed.). Cambridge: Cambridge University Press.
- [2] Mochinaga, Shota, et al. "Transport Simulation of PLATO Tokamak Plasma Using Integrated Code TASK." Plasma and Fusion Research (2021): 1403093-1 to 6.

## 国際化推進共同研究概要

No. 4

21NU-3

タイトル : Plasma start-up and sustainment in spherical tokamak configuration  
by RF

研究代表者 : SHEVCHENKO Vladimir

所内世話人 : 出射 浩

### 研究概要 :

令和3年2月2–4日の3日間で国際 WS を遠隔開催した。英国から5名、米国から2名、国内から9名の参加があった。英国、米国、国内からの参会者が参加できるよう、日本時間で 21 時からとなった。QUEST 実験の最近の進展・検討に加え、国内外実験の進展・検討、新たなシミュレーション解析などが議論された。英国から3件、米国から2件、国内で8件の研究成果発表があり、主に非誘導プラズマ電流立ち上げに関し、活発な議論があった。

# RF-only ST plasma start-up, ramp-up and sustainment

Hiroshi Idei

Vladimir Shevchenko

A Summary of the Workshop which was held remotely via Zoom on 2-4 February 2022 and was as following:

## 10<sup>th</sup> Workshop Agenda, RIAM 2022

### **2 February**

JST 21:00 / GMT 12:00 / EST 7:00 [ + 10 min. ]

Vladimir Shevchenko / Hanada

#### **WS purpose and agenda**

JST 21:10 / GMT 12:10 / EST 7:10 [ + 40 min. ]

Vladimir Shevchenko

#### **ECRH Technology on ST40**

JST 21:50 / GMT 12:50 / EST 7:50 [ + 30 min. ]

Erasmus du Toit

#### **Overview of ECRH and EBW modelling for ST40**

JST 22:20 / GMT 13:20 / EST 8:20 [ + 40 min. ]

Simon Freely

#### **Microwave current drive studies at UKAEA**

---

### **3 February**

JST 21:00 / GMT 12:00 / EST 7:00 [ + 30 min. ]

Hitoshi Tanaka

#### **LATE - Recent result and future plan**

JST 21:30 / GMT 12:30 / EST 7:30 [ + 30 min. ]

Nicola Bertelli

#### **Update of the 3-D full wave Petra-M simulation modeling of NSTX-U HHFW**

JST 22:00 / GMT 13:00 / EST 8:00 [ + 30 min. ]

Akira Ejiri

#### **Plasma current start-up by using the lower hybrid wave and its modeling on TST-2**

JST 22:30 / GMT 13:30 / EST 8:30 [ + 30 min. ]

Yongtae Ko

#### **Development of a capacitively coupled combine antenna for off-midplane launch of lower-hybrid waves in TST-2**

JST 23:00 / GMT 14:00 / EST 8:30 [ + 30 min. ]

Masayuki Ono

## **Accessibility enhanced ECH and ECCD for plasma current start-up and ramp-up**

---

**4 February**

JST 21:00 / GMT 12:00 / EST 7:00 [ + 30 min. ]

Hiroshi Idei

**Recent Topics on 28-GHz ECHCD in QUEST**

JST 21:30 / GMT 12:30 / EST 6:30 [ + 30 min. ]

Shin Kubo

**Study of excited EBW detection by sub-Tera-Hz scattering in the QUEST**

JST 22:00 / GMT 13:00 / EST 6:50 [ + 20 min. ]

Makoto Hasegawa

**Long-time operation with high temperature wall (<400 C) on QUEST**

JST 22:20/ GMT 13:20 / EST 7:10 [ + 20 min. ]

Qilin Yue

**Preliminary results of Hydrogen Recycling with Fast Ejecting System of Targeted Sample (FESTA) on QUEST**

JST 22:40 / GMT 13:40 / EST 7:40 [ + 20 min. ]

Kengo Kuroda

**Improved results of CHI discharge on remodeled system in QUEST**

JST 23:00 / GMT 14:00 / EST 8:00 [ + 10 min. ]

Vladimir Shevchenko / Hanada

**Closing**

**The presentation summaries are as following:**

Vladimir Shevchenko:

## **ECRH Technology on ST40**

Two 1 MW gyrotrons have been ordered for ST40. These gyrotrons can operate either at 105 GHz or 140 GHz with RF pulse duration up to 2 seconds. Transmission lines as well as gyrotrons are designed and manufactured by GYCOM Ltd., Nizhny Novgorod, Russia. Transmission lines are based on corrugated cylindrical waveguide elements 63.5 mm in diameter. During operation these lines are kept under vacuum higher than  $10^{-4}$  mbar. An input HE<sub>1,1</sub> mode is formed by mirrors in a matching optics unit. Each transmission line includes a miter bend combined with a directional coupler, two waveguide switches, a universal quasi-optical polarizer, several miter bends, expansion joints, vacuum pumping ports, a dielectric waveguide isolation (DC-break) and a vacuum gate. Some elements of the transmission line are cooled by water. Corrugated waveguides are manufactured from aluminum in sections of 1 m long. These sections are connected to each other and to other transmission line elements by special connectors, ensuring elements alignment and vacuum tightness.

During assembly any part of the transmission line can be connected to a short-pulse load to configure operating regimes of the gyrotron and to check performance of individual elements. The short-pulse load can operate with pulse durations not exceeding 100 ms. For full pulse length measurements RF power from any gyrotron can be directed to a shared long-pulse dummy load using two waveguide switches.

The lower field side launcher is designed to study a wide variety of ECRH and CD scenarios including conventional ECRH at second EC harmonic using extra-ordinary (X2) or ordinary (O2) modes at both 140 and 105 GHz. It also allows excitation of the EBW mode by launching of a fundamental O mode (O1) with further mode conversion into an X mode (X1) at the mirror-polarizer attached to the central post. The slow X1 mode experiences a subsequent mode conversion into EBW mode at the upper hybrid resonance and then EBW propagates back to the EC resonance. This scheme allows experimental studies of non-inductive plasma start-up, current ramp-up and sustainment.

Erasmus du Toit:

## **Overview of ECRH and EBW modelling for ST40**

A dual-frequency ECRH system is currently under development at ST40. The system will employ two GYCOM gyrotrons with a maximum output power of 1 MW each and a pulse length of 2s. Both gyrotrons can be tuned to operate at either 105GHz or 140GHz, which allows for a study of non-inductive plasma start-up, current ramp-up and sustainment.

Operations in 2022 will use a fixed low field side (LFS) launcher that allows the study of conventional ECRH at the 2<sup>nd</sup> EC harmonic using extra-ordinary (X2) or ordinary (O2) modes. Both frequencies available have good accessibility to the 2<sup>nd</sup> harmonic resonance, while modelling shows that good absorption is expected across a range of densities, as shown in figure 1.

Plasma start-up and current drive will be studied in later experiments using electron Bernstein waves (EBWs), by using the LFS launcher in an O-X-B successfully demonstrated on MAST<sup>1</sup>. An O-mode beam is launched from the LFS and converted to X-mode via a grooved mirror polarizer located on the centre post. The X-mode propagates back into the plasma and undergoes mode conversion to EBWs at the UHR, which are subsequently absorbed.

Modelling results show strong absorption of EBWs across a range of parameters, with current drive efficiencies up to 0.15A/W expected.

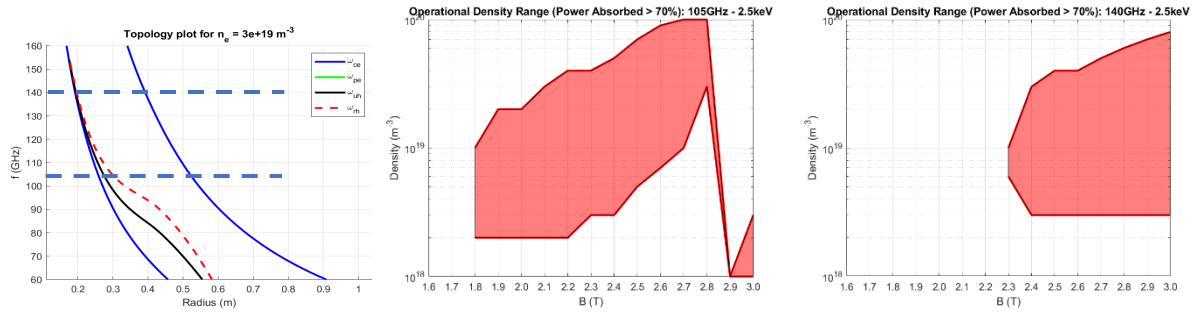


Figure 1 – Topology plot for ST40 plasma (left) shows the locations of the fundamental and 2<sup>nd</sup> harmonic resonances for  $B = 2.4\text{T}$ . The region where the fraction of power absorbed is greater than 70% is shown for a range of densities and magnetic field strengths for 105GHz (middle) and 140GHz (right) at  $T_e = 2.5\text{keV}$ .

Simon Freely

Hitoshi Tanaka

## LATE - Recent result and future plan

The primary objective of LATE (Low Aspect-ratio Torus Experiment) is to study on non-inductive formation of spherical tokamak by using ECH/ECCD. For production of over-dense plasmas, O-mode microwave is injected obliquely to the toroidal field from outboard side to excite EBW.

Recently, by using a newly developed five-pin probe antenna and two-dimensional (2-D) mechanical probe driving system, the 2-D wave pattern of phase and amplitude has been directly measured for an over-dense ECR plasma with 1.5 GHz microwave. In the case of O-mode injection, an EBW-like wave pattern has been detected for the first time, in a localized region near the upper hybrid resonance layer. The pattern has a short wavelength of about 2 mm and is also electrostatic and backward. By adjusting the toroidal magnetic field, it is found that both the position and size of the EBW region have changed, which suggest the localized condition of efficient O-X-B conversion and high collisional damping rate of EBWs.

In May 2021, the LATE device and all the diagnostics were disassembled and moved to Uji campus (~10 km away from Yoshida campus) because of repair work of Plasma Wave Experiment Building. The construction period is from August 2021 to February 2022. New 66 ports in total will be added to the original vacuum vessel. Assembling and installation will be started from April after movement of all the materials to the renovated experiment building.

Nicola Bertelli:

## **Update of 3-D full wave Petra-M simulation modelling of NSTX-U HHFW**

In this work we present recent updates of 3-D full wave Petra-M finite-element-method (FEM) simulations for NSTX-Upgrade plasma. Petra-M code [1] is a state-of-the-art generic electromagnetic simulation tool for modelling RF wave propagation based on MFEM [<http://mfem.org>], open-source scalable C++ finite element method library.

This paper shows the full 3D NSTX-U device geometry including realistic antenna geometry and 3D scrape-off-layer (SOL) plasma. The antenna geometry and the 3D NSTX-U geometry are from the NSTX-U CAD models.

These 3-D simulations show a strong interaction between FWs and the SOL plasma. Cavity modes in the SOL plasma appear in all simulations. A scan can of magnetic field ( $B = 0.6$  T,  $0.75$  T, and  $1$  T) shows was performed and the cavity modes in the SOL plasma tend to decrease for higher magnetic field. A scan in the SOL electron density ( $n_e = 1 \times 10^{18}/m^3$ ,  $2 \times 10^{18}/m^3$ , and  $5 \times 10^{18}/m^3$ ) was also performed. In this scan, the cavity modes increase with higher density. In general, these results are consistent with the 2D full wave simulations performed by AORSA [2] and FW2D [3]. Further studies in Petra-M are necessary to try to quantify the HHFW losses in the SOL plasma. An evaluation of the scattering matrix (S-matrix) in vacuum and three plasma cases (corresponding to the density mentioned above) were shown. In the vacuum, S-matrix is symmetric as expected unlike the plasma case due to the plasma absorption. The S-matrix evaluation is the first step to be able to quantify the HHFW antenna performance and compared it with the measurements.

- [1] S. Shiraiwa et al., EPJ Web of Conferences **157**, 03048 (2017).
- [2] N. Bertelli et al., Nucl. Fusion **54**, 083004 (2014).
- [3] E.-H. Kim et al., Phys. Plasmas **26**, 062501 (2019).

Akira Ejiri:

## **Plasma current start-up by using the lower hybrid wave and its modeling on TST-2**

In the TST-2 spherical tokamak, non-inductive start-up by lower-hybrid waves (200 MHz) has been studied and a plasma current of 27 kA was achieved. A model for lower hybrid wave induced transport to reproduce the hard x-ray (HX) behaviors has been constructed. The model consists of (1) orbit tracing (in Rin- Rout- Vpara space) under RF heating and collisional slowing down, self-inductive field, and (2) X-ray emission models. The experimental HX spectral shape are well reproduced by the model. Responses of RF power turn off (rapid HX decrease,  $I_p$  decay,  $n_e$  increase) are qualitatively reproduced, but the remaining HX after the turn off cannot be reproduced. The effect of self-inductive field is found to be nonnegligible. Responses of additional gas puff were investigated, and the plasma current response seems to be affected by both decreases in the fast electron loss and fast electron population. Movable target was inserted into the SOL and HX from the target was measured, and the existence of fast electrons at the outboard side SOL is indicated. Opposite directed electrons are also suggested.

Yongtae Ko:

## **Development of a capacitively coupled combline antenna for off-midplane launch of lower-hybrid waves in TST-2**

**Summary:** In the TST-2 spherical tokamak device, non-inductive plasma start-up and optimization of the current drive have been studied using lower hybrid wave with frequency of 200 MHz. LHCD has been achieved by using two antennas, one on the outer-midplane and the other on the top side. However, with the increase in plasma density, the accessibility of waves launched from the outer-midplane is restricted to the outer region, and the electron distribution cannot be controlled. The wavenumber spectrum of the top launch is ideal, but most of the electrons are lost as fast electrons in the region where the wave absorption is  $r/a > 0.7$ . In the outer-midplane launch, the wave propagates to the magnetic axis, but the phase velocity is large and the heating of thermal electrons is not achieved. The optimal launching scenario is investigated using the ray-tracking code GENRAY and the orbit-averaged Fokker-Planck code CQL3D. Calculations showed that the wave propagates through the center of the plasma and the phase velocity resonates with that of the thermal electrons when the wave of  $n_{\text{parallel}} \sim 13$  is launched from the off-midplane. In terms of the dependence of the electron density, equilibrium current and temperature, there was no significant change in the driving current and wave absorption. Thus off-midplane launch is attractive. The synergy of conventional outer-midplane launch and off-midplane launch is expected to further optimize the current drive and extend the operation regime. To prove above off-midplane antenna is designed and will be installed by May 2022.

Masayuki Ono:

## **Accessibility enhanced ECH and ECCD for plasma current start-up and ramp-up**

An efficient solenoid-free start-up and ramp-up scenario utilizing the low-field-side launch (LFSL) I-X-mode is proposed [1]. The I-X wave accessibility density limit improves significantly at higher  $B_{T0}$  as accessible density goes up as  $f^2$  (or as  $B^2 T_0$ ) that enables the current start-up and ramp-up to 10 MA with 10 MW in a reasonable plasma density of  $\sim 0.5 - 1.0 \times 10^{19}/m^3$  with a very high ECH/ECCD efficiency at 170 GHz for  $B_{T0} \sim 5 - 6$  T in Sustained High Power Density (SHPD) facility. The high ECCD efficiency is due to the strong wave-particle interactions at the Doppler broadened  $\omega = \Omega_e$  resonance, due to the strong cyclotron interaction of X-mode polarization, together with absorption on uni-directional passing electrons which results from the wave accessibility constraint. The quasi-linear analysis using CQL3D shows further enhancements of ECCD efficiency over the linear calculations due to the generation of less collisional higher energy tail electrons. The current drive efficiency remains high for a broad range of  $n/\#$  (or injection angle) suggesting that a relatively simple waveguide launcher could be used. In ST-40, using the 105 GHz gyrotron at  $B_{T0} = 2$  T, it appears to be possible to drive  $\sim 1$  MA of plasma current with 1 MW at the plasma density of  $8 \times 10^{18}/m^3$ . Once the ramp-up to the full plasma current is achieved, the same ECH system can be switched to more conventional ECH and ECCD such as the O-mode which would permit the access to high density  $\sim 2-3 \times 10^{20}/m^3$  or more advanced EBW-based scenarios for even higher density steady-state operations.

[1] M. Ono, N. Bertelli, et al., *AIP Conference Proceedings* **2254**, 090001 (2020).

Hiroshi Idei:

## Recent Topics on 28-GHz ECHCD in QUEST

Recent two topics on 28-GHz ECHCD in QUEST are reported. One is related to a new 28-GHz CW gyrotron. The gyrotron has been assembled by last year, and it is tested in this year at Univ. of Tsukuba. The designed output of 1.2 MW is achieved with cathode voltage and current of  $V_k = 80$  kV and  $I_k = 50$  A. To apply it to QUEST experiment, the performance at  $V_k = 70$  kV and  $I_k = 25$  A is checked, and reasonable output of 0.6 MW is attained with the efficiency of 38 %. It will be operated at a power level of 400 kW with CPD configuration in CW. The 480-kW output is also attained with a high efficiency of 42 % with the CPD at  $I_k = 15$  A. It enables us to operate one more gyrotron used currently with  $I_k = 10$  A also in the CPD configuration. The EC plasma ramp-up experiment with two different parallel indexes to the magnetic field will be conducted to obtain high plasma current and bulk electron temperature by using two 28-GHz systems. The other topics is related to doubling of the toroidal magnetic field in QUEST. New 100 kA power supply system, composed of lithium capacitor modules and DC-DC converters, is developing to excite 0.5 T in QUEST. The fundamental ( 1<sup>st</sup> ) and second ( 2<sup>nd</sup> ) harmonic X-mode heating scenario is considered for the 0.5 T ECHCD experiment, based on the ray tracing analysis. The incident ray from the low field side (LHS) starts to be damped as third harmonic absorption of the energetic electron and is damped as 2<sup>nd</sup> harmonic absorption of energetic and bulk electrons. In addition, it is damped as 1<sup>st</sup> absorption when it come closer to the Doppler shifted resonance and reflected back outside due to the cutoff. The total single pass absorption reaches to 80-90 %. In high density case, it reflected back outside before coming to the 1<sup>st</sup> absorption area. The ray is strongly damped as 2<sup>nd</sup> harmonic resonance in the absorption area of the bulk electrons. The resonance area for the energetic electrons strongly shifts to the high field side (HFS) due to the relativistic effect and expands to both of the HFS and LHS sides due to the Doppler shift effect. The energetic electrons in various energy range are in the up-shifted resonance in wide velocity space there. The ray does not access to the down-shifted resonance area of the energetic electrons. Three type configurations with the up-shifted resonance, not the down-shifted resonance have proposed to conduct the high efficiency ECCD experiment in QUEST.

Shin Kubo:

## Study of excited EBW detection by sub-Tera-Hz scattering in the QUEST

The QUEST is a spherical tokamak device which has been working on the topic of steady-state operation. One of the main issues is the non-inductive current drive, including the steady state current drive. Among several non-inductive current drive methods, electron Bernstein wave (EBW) heating/current drive is the most attractive method. Since the EBW can be excited through mode conversion process, it is important to clarify and optimize the injection condition by checking the excited EBW near the core region. Expected wavenumber in the perpendicular to the magnetic field ranges  $10^4$ - $10^5$  m<sup>-1</sup>. The direct and detailed measurement of the density fluctuation associated with the EBW gives clear evidence of the excited EBW inside the core, since it is an electro-static wave. Such density fluctuation can be measured by the sub-Tera-Hz wave scattering. Original idea was to apply 400 GHz gyrotrons developed for the collective

Thomson scattering (CTS) experiments. Loan term expires soon and HCN laser system in turn will be prepared as a scattering source. Scattering optics will be designed using a quasi-optical method developed.

Makoto Hasegawa

### **Long-time operation with high temperature wall (<400 C) on QUEST**

In order to investigate the controllability of particle balance during long-term discharge in a high-temperature environment, long-term discharge was performed with the high-temperature wall (hot wall) of QUEST kept at the set temperature of 400 °C. The QUEST hot wall has a sheath heater embedded in it and is in contact with the cooling water pipe, so it can be actively heated and cooled. Although the temperature was lower than 400 °C in some places due to a heater failure, it was confirmed that the experiment could be carried out safely by raising the temperature of the hot wall to the set temperature of 400 °C. And, it was confirmed that when the cooling water was started to flow during the long-term discharge at 400 °C, the Ha emission decreased and the particle supply was restarted accordingly. Thus, the temperature control of the high temperature wall is effective even in this temperature range (400 °C) and has a great influence on the particle balance. In the future, temperature control will be performed more appropriately, and data will be acquired statistically for analysis.

Qilin Yue

### **Preliminary results of Hydrogen Recycling with Fast Ejecting System of Targeted sAmple (FESTA) on QUEST**

In order to realize fusion power generation, the recycling of fuel particles, hydrogen and its isotopes, is important in the plasma facing wall (PFW) to maintain steady operation, which has a significant effect on particle balance. The hydrogen recycling on Q-shu University experiment with Steady-state Spherical Tokamak (QUEST) has been only measured globally and is limited after plasma discharge from PFWs. Therefore, a device named Fast Ejecting System of Targeted Sample (FESTA) was developed to investigate hydrogen recycling locally from a specimen by exposing it to high-temperature and density plasma in QUEST [1].

In this research, a stainless-steel type 316L specimen was exposed to QUEST plasma for three times continuously under the same plasma discharge conditions. Using background model [1], the released hydrogen flux from the plasma-exposed specimen increased over plasma exposures, indicating that hydrogen recycling became more dominant during plasma discharges. Furthermore, it has been observed that the outgassing characteristics changed over plasma discharges, which is unknown for now and should be further investigated.

[1] Q. Yue, et al Plasma Fusion Res. 15 (2020) 240201

Kengo Kuroda:

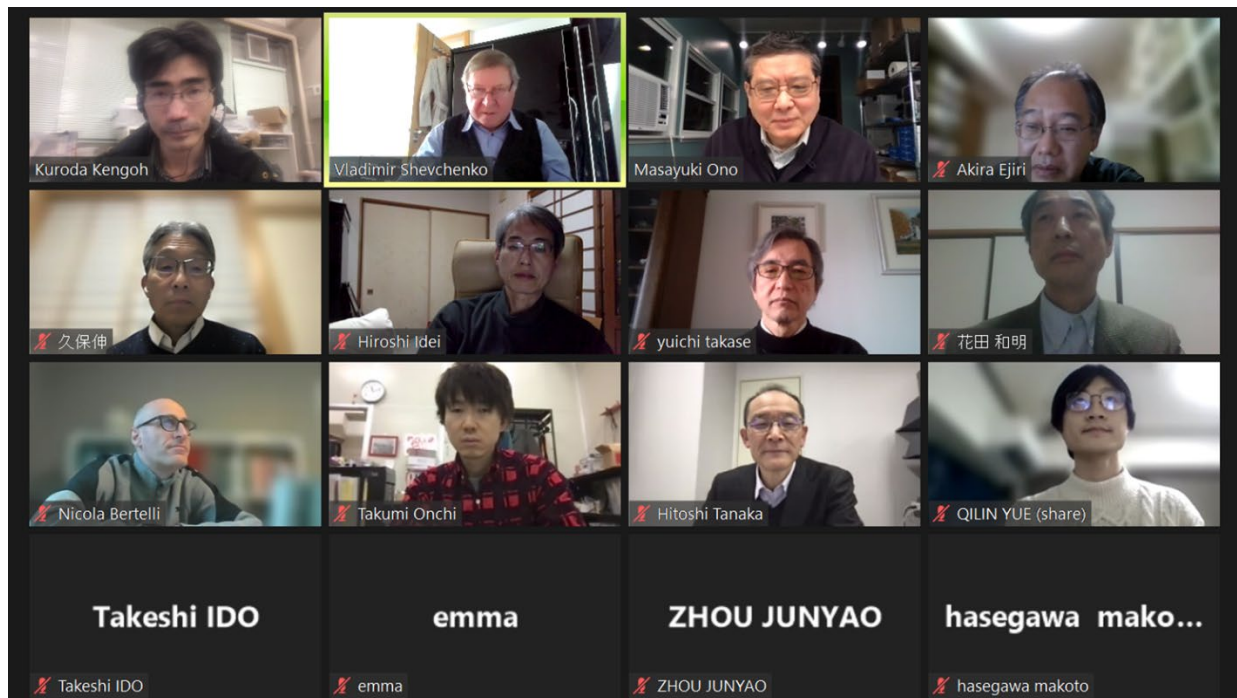
### **Improved results of CHI discharge on remodeled system in QUEST**

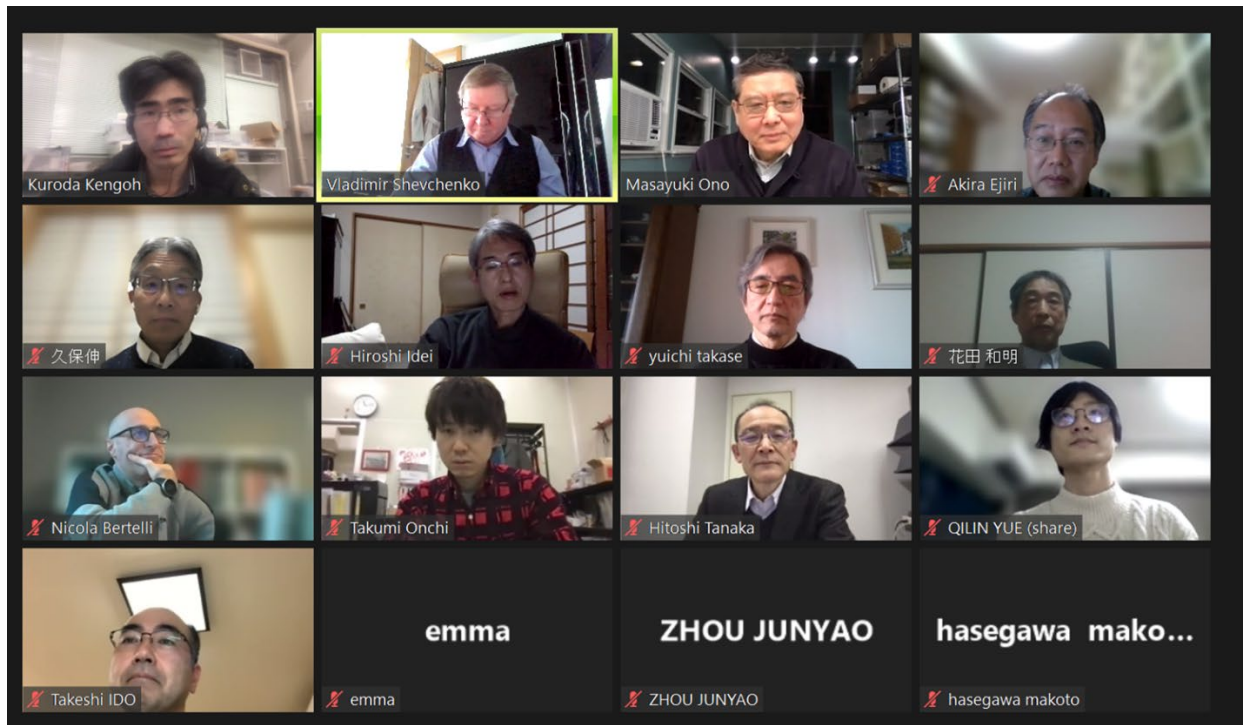
T-CHI current start-up by using newly designed simple electrode has been examined in QUEST:

- Improved result of HFS CHI discharge was obtained in 2021 Feb experiment
- T-CHI system was remodeled on a large-scale in 2021 for higher performance of the current drive.

We obtained progressive results (1~4) on the initial experiment on the remodeled system:

1. 100% of occurrence of breakdown is achieved with lower breakdown conditions
2. Absorber arc is prevented on higher level injector flux configuration
3. Achievement of more than 100kA of current drive
4. Flux evolved largely, but relatively high vertical field was required.





## 国際化推進共同研究概要

No. 5

21NU-4

タイトル：Joint study of calorimetric measurement of heat load and power balance estimation and measurement and simulation of energetic electrons loss in steady state operation (SSO) plasmas on QUEST and EAST

研究代表者：LIU Haqing

所内世話人：花田 和明

研究概要：コロナの影響で来日はかなわなかったが、遠隔で双方の研究の内容の議論を行い、以下の結果を得た。

- 長時間運転で必ず問題になる局所的熱負荷による「ホット・スポット」について議論を行った。特に今年度は EAST 装置でのホット・スポットの原因が、炭素ダイバータの除熱性能とプラズマ加熱用波動の周辺部での衝突減衰によるものであることを見出した。
- EAST 装置では炭素ダイバータをタンクステン化して除熱性能を向上させて 1000 秒を超えるプラズマ維持に成功した。
- 関連する成果に関する論文を執筆中であり、そのほか以下の 3 編が掲載決定済みである。

[1] K. Hanada, ....., H.Q.Liu, et al., "Overview of recent progress on steady state operation of all-metal plasma facing wall device QUEST", Nuclear Materials and Energy **27**(2021) 101013.

[2] Y. Q.Chu, H.Q.Liu, ....., K. Hanada, et al., "Study of the mechanism of ITB formation and sustainment with optimized q profiles in ELM My H mode discharges on the EAST", Plasma Phys. Control. Fusion **63**(2021) 105003.

[3] Y. Q.Chu, H.Q.Liu, ....., K. Hanada, et al., "MHD effect of internal transport barrier on EAST tokamak", Plasma Science and Technology (2022) to be published.

## **Introduction**

Steady state operation (SSO) of magnetic fusion devices is one of the goals for fusion research. The longest steady-state H-mode plasma (#73999 discharge in EAST) with the USN divertor configuration during the 2017 campaign was lasted 101.3 s at a plasma current of 0.4 MA. The hot spot appeared from about 55 s to the end of the shot on the lower graphite divertor maybe one of the important reasons for the degradation of plasma quality and early termination. Hot spots as an interaction between plasma and plasma facing components (PFCs) frequently prevent from maintaining high performance plasmas through unwanted impurity emission. Moreover, the hot spots have a potential to make a meltdown of PFCs which cause serious damages to the machine. After the appearance of the hot spot, the heat load distribution on the first wall was significantly changed. The heat load decrement on the upper divertor is 22.6 MJ from 55 s to 105 s, and this part of power was delivered from the upper divertor to the lower divertor and to the guard limiters of the LHW injection systems. In order to achieve higher parameters and longer duration plasma, it is necessary to find the reason for the appearance of the hot spot. The power handling capability of tungsten divertor is about  $10 \text{ MW m}^{-2}$ , it is a safer divertor material than graphite for the excessive local heat load. So, a new lower tungsten divertor has been developed and installed in the EAST in early 2021, and the cooling system of the lower divertor has also been upgraded.

In this year, the collaboration research focused on analyzing and finding the cause of hot spot formation, and comparing the heat load capacity of tungsten and graphite divertors through calorimetry.

## **Recent results in 2021**

A relativistic guiding center orbit code (RGCO) has been finished and applied to investigate the prompt loss of electrons accelerated by injected RF electric field. ECW (Electron cyclotron Wave) is the main source of energetic electrons on QUEST. LHW (Lower Hybrid Wave) is an efficient way to heating and drive the plasma current, and is the main source of energetic electrons on EAST. The RGCO can be easily applied to both EAST and QUEST tokamaks, because the equilibrium magnetic fields for the simulation are provided by the EFIT code. The orbit simulation can take into account the realistic wall geometry outside the last closed flux surface (LCFS). The toroidal geometry (toroidal position of two LHW antennas) is included in the code. So, it can be used to study the LHW power loss in the scrape-off layer (SOL) and deposited in hot spots on the divertor. The result shows that the electron with pitch angle from  $130^\circ$  to  $180^\circ$  in the dRmid zone in front of the LHW antenna can move along magnetic field lines then attack the lower divertor to form the hot spot, implying that the LHW power couples across the entire width of the dRmid zone rather than mostly at the antenna face. The dRmid is the distance between the LCFS and secondary last flux surface as shown in figure 1. And the simulation result is shown in figure 2. For shot 73999, it is the change of the plasma configuration (the magnitude of dRmid gradually increases with time, confirmed by the EFIT equilibrium reconstruction) that leads to the formation of hot spots on the lower divertor, thus causing the change of the heat load distribution

on the PFCs. The energetic electrons tracing code combined with the EFIT equilibrium code is a good simulation framework for the research both on QUEST and EAST. Electron orbit mapping provided by the code combination can be used to explain the experiment observations.

In early 2021, the material of lower divertor has been developed from graphite to tungsten, aiming at achieving higher power handling capability and achieving longer H-mode operations. Combined with the experience of long-pulse operation accumulated in previous rounds of experiments, EAST achieved a long-pulse high-parameter plasma operation with 1056.66 s, the plasma configuration is well controlled throughout this discharge. Discharge parameters are stable during the whole current flat plateau. And the time evolution of heat load exhausted by the cooling water can be seen in figure 3. It can be seen in figure 3 that the heat load exhausted by the lower divertor is larger than that of the upper divertor, which is in line with the previous experimental conclusion of EAST. From 393 s to 585 s, the exhausted heat load drops due to the drop in temperature of the cooling water, this is due to the cooling water flow through the entire cooling circuit and get cooled.

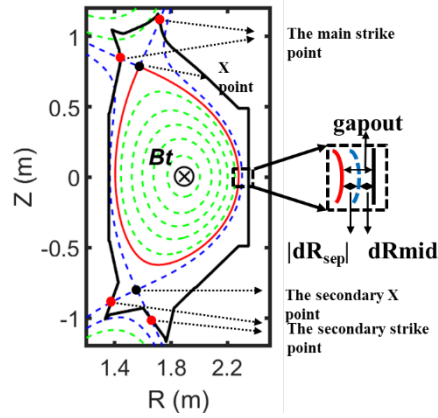


Figure 1. The schematic diagram of the plasma configuration.

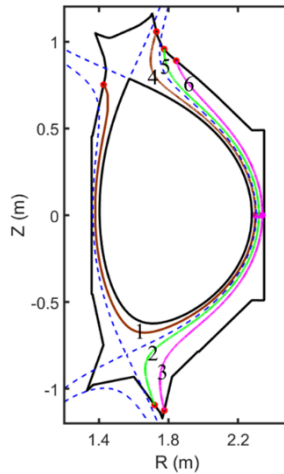


Figure 2. The electron orbit simulation, the start point in the SOL along the R coordinate.

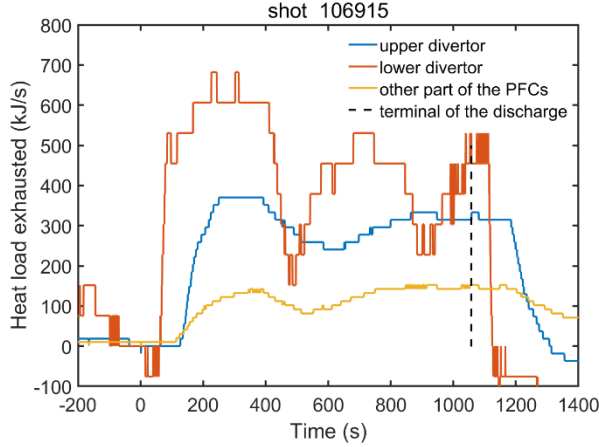


Figure 3. The time evolution of heat load exhausted by the cooling water.

## Discussions

This year, the collaboration research focused on the mechanism of the hot spot formation, comparing the heat load capacity of tungsten and graphite divertors through calorimetry. In 2021, the material of lower divertor has been developed from graphite to tungsten, aiming at achieving higher power handling capability and achieving longer H-mode operations. Combined with the experience of long-pulse operation accumulated in previous rounds of experiments, EAST achieved a long-pulse high-parameter operation with 1056.66 s, the plasma configuration is well controlled. Recent progress on SSO of all-metal plasma facing wall device QUEST was also well studied in this year's research. The results in EAST and QUEST will provide crucial support for ITER and CFETR. Energetic electrons are the main source of heat load which are generated by injected RF electric field. ECW (Electron cyclotron Wave) is the main source of energetic electrons on QUEST. LHW (Lower Hybrid Wave) is an efficient way to heating and drive the plasma current, and is the main source of energetic electrons on EAST. A significant fraction of LHW power applied to EAST can be lost to the scrape-off layer (SOL) and deposited in hot spots on the divertor rather than in the core plasma. This topic has been researched on many devices such as JET and Tore-Supra. The result show that the LHW power flows to these hot spots along magnetic field lines passing through the SOL in front of the antenna, implying that the LHW power couples across the entire width of the SOL rather than mostly at the antenna face. The energetic electrons tracing code combined with the EFIT equilibrium code is a good simulation framework for the research both on QUEST and EAST. Electron orbit mapping provided by the code combination can be used to explain the experiment observations. This is a very interesting issue for the coming year's joint research.

In this year's joint research, I have many fruitful discussions with Prof.Hanada's doctor student, Mr. Yunfei Wang, on his doctoral research issues. Three Co-Publications are achieved in 2021-2022.

## Acknowledgement and comments:

Work supported by the international joint research at the Joint Usage of Research Centers for Applied Mechanics for 2021. I would like to thank our host, Professor K. Hanada, who helps a lot during our remotely research and very appreciate the fruitful discussions and comments. Also RIAM and QUEST staffs are thanked for her kindly helps for this year's joint research. We hope that the international joint research at the Joint Usage of Research Centers for Applied Mechanics could continue to enhance China-Japan cooperation on fusion plasma research in the future.

**Co-Publications in 2021-2022:**

- [1] K. Hanada, ...., H.Q.Liu, et al., "Overview of recent progress on steady state operation of all-metal plasma facing wall device QUEST", Nuclear Materials and Energy **27**(2021) 101013.
- [2] Y. Q.Chu, H.Q.Liu, ...., K. Hanada, et al., "Study of the mechanism of ITB formation and sustainment with optimized q profiles in ELMMy H mode discharges on the EAST", Plasma Phys. Control. Fusion **63**(2021) 105003.
- [3] Y. Q.Chu, H.Q.Liu, ...., K. Hanada, et al., "MHD effect of internal transport barrier on EAST tokamak", Plasma Science and Technology (2022) to be published.

(Signature) Haiqing Liu  
(Name in print) Haiqing Liu

## 国際化推進共同研究概要

No. 6

21NU-5

タイトル：Soft x-ray spectra in inboard poloidal field null (IPN) configuration and relevant physical research on QUEST

研究代表者：JIE Yinxian

所内世話人：花田 和明

研究概要：コロナの影響で来日はかなわなかったが、遠隔で双方の研究の内容の議論を行い、以下の結果を得た。

- IPN 配位での粒子の損失機構として粒子軌道計算に基づいた検討を行った。本研究によって EAST、QUEST 双方の磁場配位で計算可能な相対論的効果を含んだ粒子軌道計算を完成させた。
- 関連する成果に関する論文を執筆中であり、そのほか以下の 2 編が掲載決定済みである。

[1] Y. Q.Chu, ..., Y.X. Jie, ..., K. Hanada, et al., Plasma Phys. Control. Fusion **63**(2021) 105003.

[2] Y. Q.Chu, ..., Y.X. Jie, ..., K. Hanada, et al., Plasma Science and Technology (2022) to be published.

Research subject: Soft x-ray spectra in inboard poloidal field null (IPN) configuration and relevant physical research on QUEST

Due to COVID-19 pandemic, this year we worked remotely. Soft x-ray spectra system is a very important diagnostic on tokamaks. It is one of the most widely used in measuring the plasma electron temperature and MHD phenomena. The whole system needs modification to get more detail date to get the position of IPN and relevant physical research on QUEST.

First, I discussed the mission with Mr. Canbin HUANG. The mission of QUEST is to develop the scientific basis for achieving a steady state condition at sufficiently high beta ( $\sim 20\%$ ), with high confinement and low collisionality. Operating Tokamak at a high poloidal beta value is usually attractive and this makes the spherical tokamak an interesting choice for future reactors. The maximum achievable  $\beta p$ , however, is limited by a so called equilibrium limit, where an inboard poloidal magnetic field null (IPN) appears at the high field side of the vacuum vessel. Inboard poloidal field null (IPN) configuration in a high  $B_p$  discharging was reported first time on TFTR in 1991. In those discharge the evolution of the poloidal field measured at the midplane on the inboard side of the TFTR vacuum vessel was studied. As  $I_p$  was ramped down, and  $B_p$  increased, the midplane poloidal field decreased and eventually became negative, indicating that the separatrix had crossed the coil position and moved into the vacuum vessel. The separatrix-limited discharge was sustained until the end of the beam heating phase. In QUEST, such an IPN configuration is easily achieved under a high magnetic mirror ratio and high  $B_z/B_t$  values ( $\approx 10\%$ ) via electron cyclotron (EC) heating and current drive. A soft x-ray spectra system was set up on QUEST and got some primary date. The whole system needs modification to get more detail date to get the position of IPN on QUEST.

Investigation of loss mechanism of the energetic electron in QUEST provides finally a good assistance of confinement of alpha particle in the international thermo-nuclear fusion reactor (ITER) and designing fusion devices such as Japan DEMO and CFETR (China Fusion Engineering Test Reactor) in China.

**Co-Publications in 2021-2022:**

- [1] Y. Q.Chu, ..., Y.X. Jie,..., K. Hanada, et al., Plasma Phys. Control. Fusion **63**(2021) 105003.
- [3] Y. Q.Chu, ..., Y.X. Jie,..., K. Hanada, et al., Plasma Science and Technology (2022) to be published.

(Signature) Y. Jie

(Name in print) Yinxian Jie

## 国際化推進共同研究概要

No. 7

21NU-6

タイトル : Joint study of long pulse high beta discharges and related edge turbulence transport in steady state operation (SSO) plasmas on QUEST and EAST

研究代表者 : GAO Xiang

所内世話人 : 花田 和明

研究概要 : コロナの影響で来日はかなわなかったが、遠隔で双方の研究の内容の議論を行い、以下の結果を得た。

- EAST でのプラズマ加熱の高効率化に向けてプラズマと波動の結合について議論をしてきた。
- EAST では波動加熱の高効率化に向けて低域混成波用のアンテナを FAM から PAM に変更した。しかしプラズマ蓄積エネルギーの増加は観測されなかつたため、この問題の検討を開始した。現在検討を進めている最中である。
- 関連した研究で、以下の 1 編が掲載決定済みである。

[1] K. Hanada, ....., X. Gao, et al., "Overview of recent progress on steady state operation of all-metal plasma facing wall device QUEST", Nuclear Materials and Energy 27(2021) 101013.

## **Introduction**

This year, given the situation of COVID-19, the joint research was done remotely.

Steady state operation (SSO) of tokamak plasma is one of the basic requirements for future fusion reactors. Long pulse high beta operation is one of important missions for ITER. Joint study long pulse high beta discharges in SSO plasma research field on QUEST and EAST is strongly supporting ITER experiment from both experience and theory. In this year, the collaboration research focused on the power balance in SSO high performance discharge and coupling of injected energy and plasma during discharge, which is benefit for the SSO high beta discharges of EAST and QUEST.

## **New results in 2021**

The Experimental Advanced Superconducting Tokamak (EAST) research program concentrates on demonstrating steady-state high-performance H-mode operations with ITER-like tungsten divertor. Calorimetry was applied to actively water-cool the plasma facing components (PFCs) by increasing the water temperature for power balance investigation. A new lower tungsten divertor has been developed and installed in the EAST superconducting tokamak in early 2021 to replace the previous graphite divertor with power handling capability increasing from  $<2 \text{ MW m}^{-2}$  to  $\sim 10 \text{ MW m}^{-2}$ , aiming at achieving long-pulse H-mode operations in a full metal wall environment with the steady-state divertor heat flux of  $\sim 10 \text{ MW m}^{-2}$ . In 2021 EAST winter campaign, the record longest steady-state long-paused high-parameters plasma #106915 was sustained for up to 1056.66 s with net injected energy exceeding  $\sim 1.42 \text{ GJ}$  in the DSN configuration. It can be seen in figure 1 that the discharge parameters are stable. The loop voltage is well controlled to be nearly 0 V, which means that almost all of the plasma current is noninductive. The strike point is almost unchanged, which means that the plasma configuration is well controlled. H/H+D rises slowly because of the live application of lithium to the PFCs. The first wall maintains a strong pumping capacity, and the particle recirculation is controllable. Figure 1 (b) shows that except for ICRF-N limiter, the temperature of other PFCs are relatively stable.

Heat load analysis of this discharge using calorimetric measurement in figure 2 indicates that the water temperature increment of the upper divertor became almost constant for the first time at about 250 s, for the second time at about 864 s. During this time, the temperature of cooling water decreases because after about 400 s, the cooling water goes through a complete cycle and is effectively cooled by the external cooling tower.

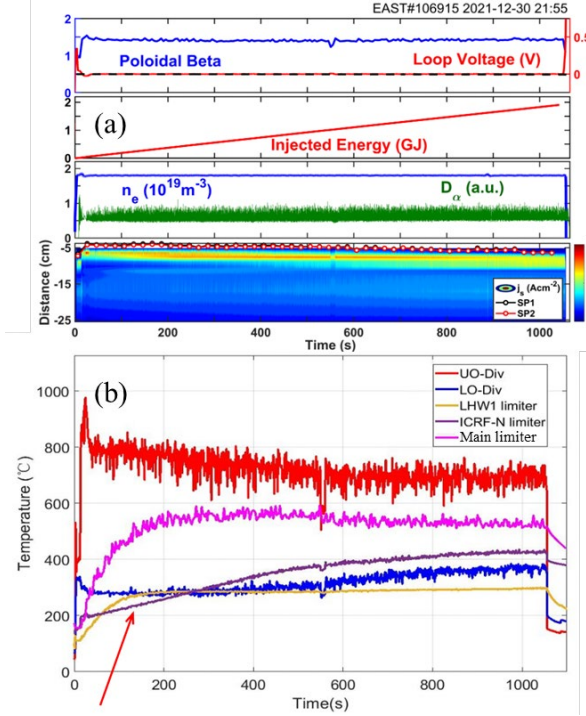


Figure 1. Parameters of shot 106915. (a): Time evolution of Poloidal Beta, Loop Voltage, injected energy, line-averaged electron density,  $D_\alpha$  and  $j_s$ , (b): time evolution of temperature about main PFCs.

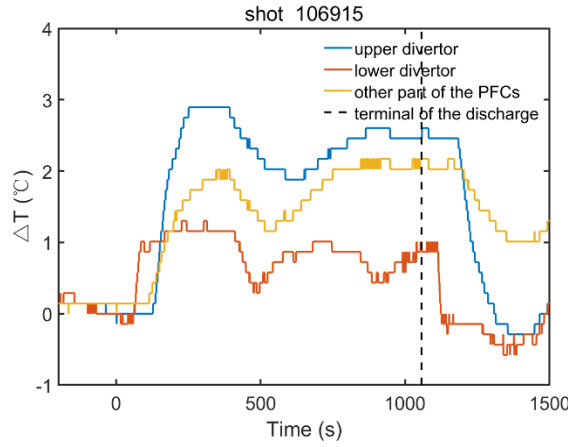


Figure 2. The time evolution of cooling water temperature increment in the upper divertor, lower divertor and other part of the PFCs.

In a LHW modulation experiment (EAST USN shot 74864) during 2017 EAST Campaign, the hot spot appeared in the lower graphite divertor. Some important parameters of shot 74864 can be seen in figure 3. The auxiliary heating power are consisted of  $\sim 0.65$  MW LHW1,  $\sim 0.65$  MW LHW2. The duty ratio of LHW1 and LHW2 are 50% and each heating period is about 1 s. The line-averaged electron density is well controlled as a constant. The stored energy at 5 s is  $\sim 0.54 \times 10^5$  J, it can be clearly observed that the injection of LHW has a significant effect on increasing plasma stored energy. Figure 4 (a) is the

photo taken by IR camera in port G, the LHW 2 antenna and two graphite limiters are on the left side of the figure. Figure 4 (b) is the average temperature evolution over time of the four zones marked in figure 4 (a). The temperature in zone 1 is strongly related to the injection of LHW 1, but is weakly related to the injection of LHW 2. This indicates the heat deposition at zone 1 was caused by LHW 1 injection. The temperature in zone 3 and 4 changed with the injection of LHW 1 and 2 simultaneously, because the heat load of upper divertor in USN configuration is from core plasma ultimately. After the GENRAY/ CQL3D simulation, it can be concluded that the non-resonant collision absorption (one of the mechanisms of LHW power deposit, which mainly occurs in the SOL zone) causes the hot spot appearance during the LHW1 injection. For LHW1, more energy is deposited in the SOL, so less energy is deposited in the plasma core, which is not conducive to the improvement of the main plasma parameters.

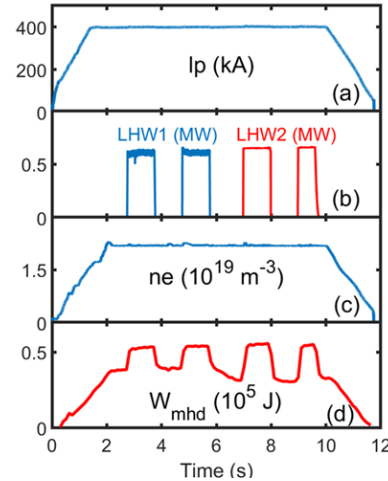


Figure 3. Parameters of shot 74864. (a): plasma current, (b): auxiliary heating power of LHW 1 and LHW 2, (c) line-averaged electron density measured by the 6th chord of the POINT system, (d): stored energy.

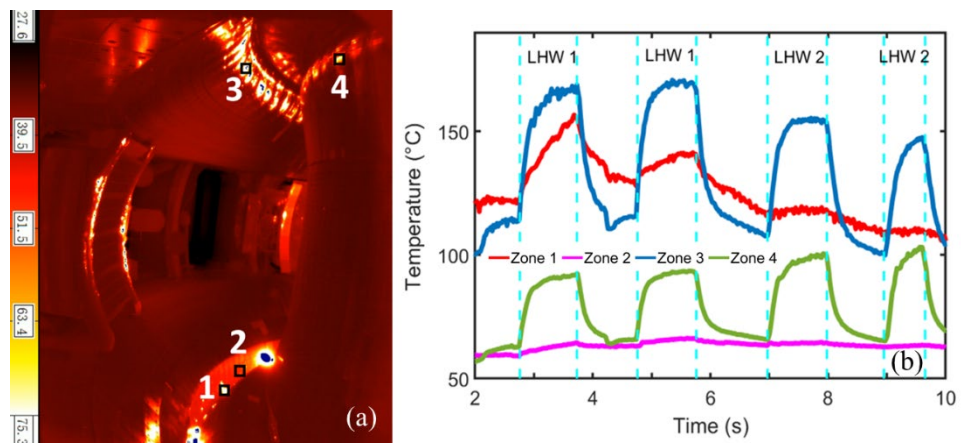


Figure 4. (a): IR camera photo of EAST chamber and location marks from zone 1 to zone 4 in discharge 74864. (b):

*The evolution of average temperature over time for the four zones.*

## **Discussions**

The major motivation of this project is to realize SSO plasma, based on QUEST and EAST device. In 2021 EAST winter campaign, the LHW1 antenna was changed from FAM to PAM, aiming at achieving better coupling between LHW power and plasma. But in some shots, the increase in the LHW1 power did not appear as an increase in plasma stored energy, indicating that this part of energy is not constrained by the main plasma. We will focus on the studying of the wave-plasma physics, such as coupling between LHW power and plasma, for achieving high-parameter SSO of the tokamak. In 2022, this subtheme will continue pursue in long pulse high beta discharges and related pedestal structure and edge turbulence transport in SSO plasma on QUEST and EAST. Comparison and combination study based on the calorimetry and other diagnostics will continue be done on both devices. The combined study will be helpful for understanding the underlying physics and obtaining H mode plasma on QUEST. It is benefit for the long pulse high beta discharges of EAST and QUEST.

## **Acknowledgement and comments:**

Work supported by the international joint research at the Joint Usage of Research Centers for Applied Mechanics for 2021. I would like to thank our host, Professor K. Hanada, who helps a lot during our remotely research and very appreciate the fruitful discussions and comments. Also RIAM and QUEST staffs are thanked for her kindly helps for this year's joint research. We hope that the international joint research at the Joint Usage of Research Centers for Applied Mechanics could continue to enhance China-Japan cooperation on fusion plasma research in the future.

## **Co-Publications in 2021-2022:**

- [1] K. Hanada, ....., X. Gao, et al., "Overview of recent progress on steady state operation of all-metal plasma facing wall device QUEST", Nuclear Materials and Energy **27**(2021) 101013.

(Signature) \_\_\_\_\_ Xiang Gao \_\_\_\_\_

(Name in print) \_\_\_\_\_ Xiang Gao \_\_\_\_\_

## 国際化推進共同研究概要

No. 8

21NU-7

タイトル： Improved EFIT code of the plasma equilibrium reconstruction for physical study on QUEST

研究代表者： QIAN Jinping

所内世話人： 花田 和明

研究概要： コロナの影響で来日はかなわなかったが、遠隔で双方の研究の内容の議論を行い、以下の結果を得た。

- 過渡的な電磁応答で発生する金属容器の渦電流は、プラズマの平衡磁場配位の計算に大きな影響があることが知られている。今年度はフーリエ展開を用いた渦電流の計算コードを開発してプラズマ平衡計算EFITに適用した。検討の結果、5、6次のモード展開が適当であることが判った。
- この渦電流の効果は、プラズマ電流やプラズマ形状にはほとんど影響がなかったが、蓄積エネルギーには大きな影響が見られた。EASTではディアマグで計測した蓄積エネルギーと平衡計算で得た蓄積エネルギーに差があったが、渦電流を考慮した結果、この差が非常に小さくなる結果を得た。
- この渦電流の影響は QUEST ではより顕著になると予測されるため、双方にとって重要な結果を得たこととなる。
- 関連した研究で、以下の 1 編が掲載決定済みである。

[1] K. Hanada, ....., X. Gao, et al., "Overview of recent progress on steady state operation of all-metal plasma facing wall device QUEST", Nuclear Materials and Energy 27(2021) 101013.

## RESEARCH REPORT

Date Feb. 13 2022

Visiting scientist: (name) Jinping Qian

(position) Professor

(university / institute) Institute of Plasma Physics,

Chinese Academy of Sciences

Host scientist: (name) K. Hanada

(position) Professor

(university / institute) Kyushu University

Research period: (from) \_\_\_\_\_ (to) \_\_\_\_\_

## Research subject: Develop and improve EFIT code of the plasma equilibrium reconstruction for SSO operation and advanced physical study on QUEST

Due to COVID-19 pandemic, this year we worked remotely. We improved the equilibrium reconstruction with eddy current calculation. The method of using Fourier expansion model to represent eddy current distribution for the improvement of equilibrium reconstruction is explored. It is shown that vacuum vessel current can be generally determined with the Fourier expansion model through the equilibrium reconstruction. Comparison of the eddy current distributions reconstructed with Fourier expansion model against the presets are presented. The reconstructed results are found to reasonably agree with the presets. The experimental equilibrium reconstruction is improved with the reconstructed eddy current.

To test Fourier expansion model in reconstructing eddy current, benchmarking and test are performed to calculate the eddy current with the simulated magnetic data. The magnetic data are simulated from the equilibrium analysis with an EAST double-null divertor equilibrium. From the equilibrium analysis, the 35 flux loops and 38 magnetic probes are simulated. The equilibrium is computed on a  $65 \times 65$  ( $R, Z$ ) grid using the EFIT code. In order to test Fourier expansion model's capability, the different eddy current distributions are assumed. Then these extra signals are computed through Green function and merged correspondingly to the 35 flux loops and 38 magnetic probes. Finally, the simulated magnetic data is used as the inputs to test the equilibrium reconstruction and eddy current distribution.

Here, the five kinds of eddy current distribution are reconstructed and compared with the presets. And every preset eddy current distribution is reconstructed by EFIT using different order Fourier expansion models. As shown in figure1, the reconstructed eddy current distributions agree well with the preset ones.

One important element in the reconstruction of the preset eddy current distributions is the choice of an appropriate Fourier expansion model. The unknown parameters  $[a_0, a_n, b_n]$  are determined by LSM (least square method), which means that higher order Fourier expansion model would improve fitting accuracy with sufficient external magnetic data in ideal conditions. However, the finite magnetic measurements suggesting the limited unknown parameters can be used in LSM fitting. To check the sensitivity against the number of fitting parameters for the Fourier expansion model, we vary the Fourier expansion order from 1 to 15. Reconstructed eddy current distribution's RMSEs (root mean square error) are shown in figure 2. According to the data analysis, 5-order and 6-order Fourier expansion model are appropriate model with sufficiently high accuracy for different eddy current distributions, as shown in figure 2. Note that smaller RMSE represent a higher-precision reconstruction.

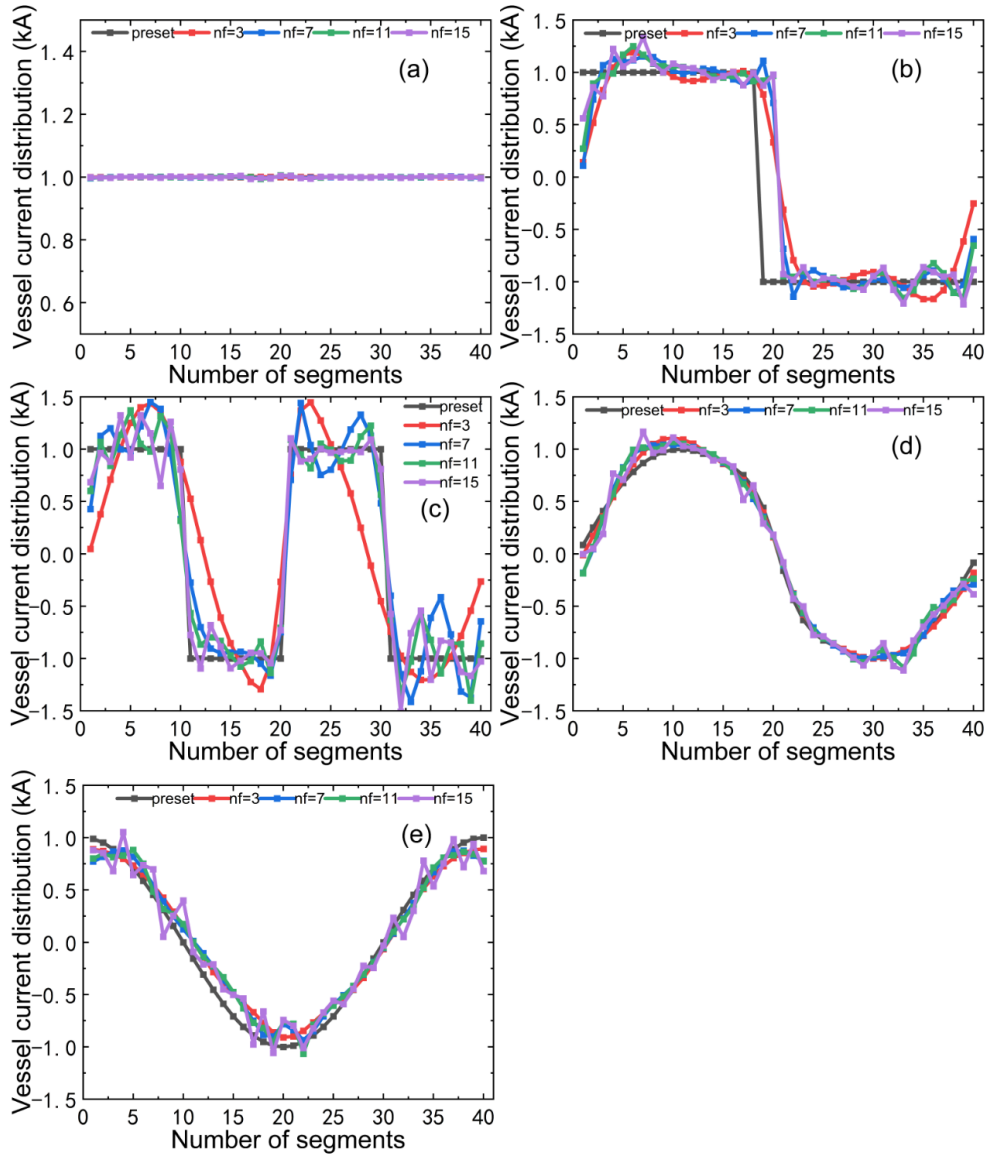


Figure 1 Preset and reconstructed of five kinds of vessel current. Black line is the preset and red line, blue line, green line and purple line represets the reconstructed ones with 3-order, 7-order, 11-order and 15-order Fourier expansion model respectively.

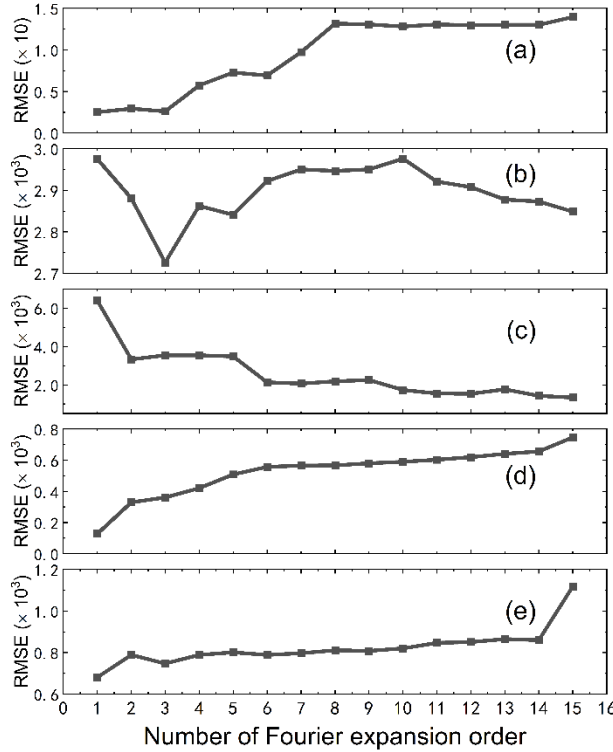
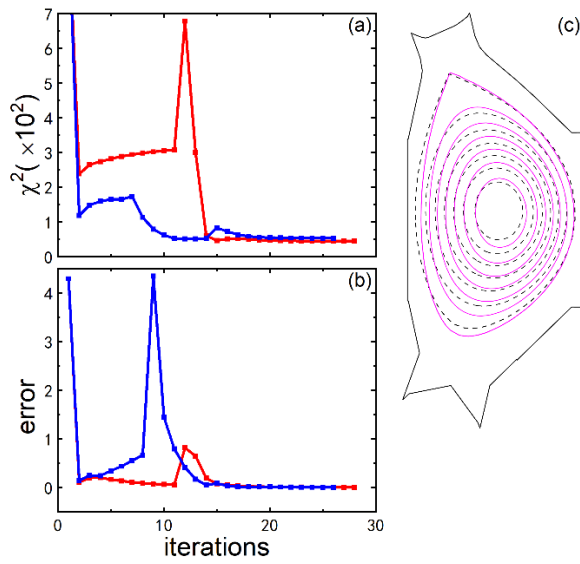


Figure 2 RMSE (root mean square error) of the five kinds of eddy current distribution's reconstruction with different order Fourier expansion model.

Furthermore, we test the eddy current distribution reconstruction algorithms using experimental EAST data. An EAST high loop voltage single-null divertor discharge (discharge 91929) is used. The reconstruction of discharge 91929 at 7500 ms is shown in figure 3. The reconstructed magnetic surfaces, the evolution of  $\chi^2$  and the maximum relative error of  $\psi$  during the iterations reconstructed with consideration of eddy current are compared with those without eddy current in figure 3(a), 3(b) and 3(c) respectively. As shown in figure 3(c), the two reconstructed magnetic surfaces are basically same. Both  $\chi^2$  and the relative  $\psi$  error decrease rapidly as the iterations proceed. The global plasma parameters are compared in table 1. As expected, most global parameters are close while plasma stored energy  $W_p$ (kJ) increases from 60kJ to 80kJ.

The time history of plasma stored energy using the diamagnetic measurement (red curves) compared with the reconstruction with (blue) and without (green) consideration of eddy current are shown in figure 4. It is obvious that the reconstructed plasma stored energy with the consideration of eddy current is consistent with the diamagnetic measurement, while the other shows a trend of decrease during the discharge.



*Figure 3 Comparison of magnetic surfaces, the evolution varying with iterations of  $\chi^2$  and the error reconstructed with consideration of the eddy current (red solid line and blue line for magnetic surface,  $\chi^2$  and error respectively) and those (black dashed line and red line for magnetic surface,  $\chi^2$  and error respectively) leaving out the eddy current for an EAST high loop voltage discharge 91929 at 7500 ms.*

*Table 1 Comparison of several parameters for two EAST reconstructions with and without consideration of vacuum vessel eddy current for discharge 91929 at 7500 ms.*

Case	With eddy current	Without eddy current
$I_p(\text{MA})$	0.46	0.46
$\Omega(\text{m}^3)$	10.60	10.57
$a(\text{m})$	0.45	0.43
$k$	1.6	1.7
$\delta_U$	0.59	0.62
$R_M(\text{m})$	1.87	1.88
$Z_M(\text{m})$	0.05	0.04
$W_p(\text{kJ})$	60	81

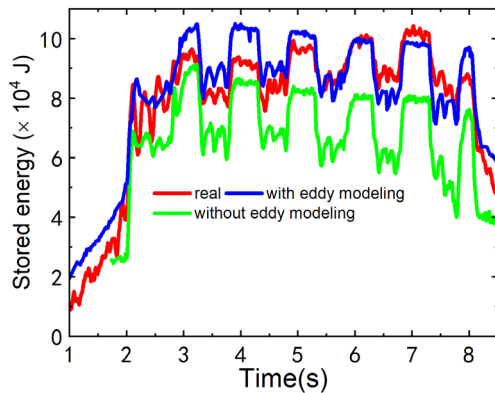


Figure 4 Evolution of plasma stored energy by diamagnetic measurement (red line) with the reconstructed one taking account of eddy current (blue line) and the one (green line) reconstructed with regardless of eddy current.

In addition, the total eddy current is computed and compared with the measured one using Rogowskii coil outside and inside the vessel during the whole discharge in figure 8. As shown in figure 5, they agree well with each other during the whole discharge, and the comparison shows that the reconstructed eddy current is reasonable.

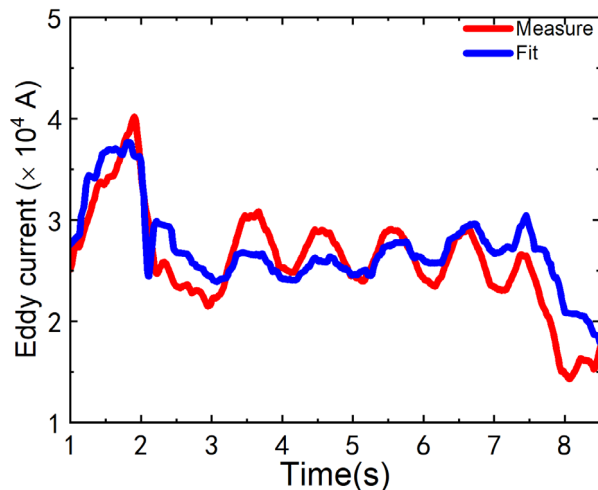


Figure 5 Comparison of measured eddy current (red line) and reconstructed (blue line).

#### Co-Publications in 2021-2022:

- [1] K. Hanada, ...., J. Qian, "Overview of recent progress on steady state operation of all-metal plasma facing wall device QUEST", Nuclear Materials and Energy **27**(2021) 101013.

(Signature) J. Qian

(Name in print) Jinping Qian

## 国際化推進共同研究概要

No. 9

21NU-8

タイトル : Local plasma parameter measurements using a multi-color tomography system

研究代表者 : CAVEDON Marco

所内世話人 : 文 賛鎬

### 研究概要 :

この国際共同研究は RIAM で行われているトモグラフィーを用いた乱流計測をさらに発展させ、プラズマの発光強度ではなく、より基本的な物理量である電子密度・温度の二次元揺動計測手法を確立することを目的とした。複数のヘリウムの輝線を二次元計測することで、それらの強度の比率から電子温度・密度を推定することができる。この手法では原子のモデル計算によって輝線の強度を電子温度・密度の関数として正確に予測することが不可欠である。マックスプランク・プラズマ物理学研究所の ASDEX-Upgrade トカマクの実験データを用いてヘリウムの原子モデルの検証を行なった。また複数の輝線の強度を適切に組み合わせることで信号の電子密度・温度依存性を調整し、電子温度または密度のみの揺動スペクトルを抜き出す解析手法を開発した。この手法により EDA H-mode における電子温度・密度それぞれの揺動スペクトルを 90kHz まで計測することに成功した。

# Local plasma parameter measurements using a multi-color tomography system

Università di Milano-Bicocca Marco Cavedon

## Introduction:

The aim of this research is to establish a method to measure local electron density and temperature on a turbulence time scale by using line ratios. Two-dimensional fluctuating structures have been characterized by inverting the intensities of emission lines at PANTA. Emission line intensities depend on electron density, electron temperature and neutrals, each of which plays a different role in turbulence and resulting transport. Therefore, extracting fluctuations of individual quantities helps further understand the physics of magnetized plasmas. The same technique is also applicable to the tomography system at PLATO currently under development.

Since PANTA allows for the direct comparison between the line-ratio techniques and probe measurements, this research can also provide the basis for the further development of Helium beam emission spectroscopy and gas puff imaging, which have been installed on many large devices including ASDEX-Upgrade, NSTX-U, JET and W7-X. At the moment, PANTA is the only device where the reliable validation of the line-ratio technique for the electron temperature and density measurements against Langmuir probes can be conducted. This is why the joint research between Riam and Max Planck institute for plasma physics (IPP) has been initiated.

## Results:

Unfortunately, a visit to Riam was not possible due to the outbreak of Covid-19. Thus, main efforts were made at IPP by using the thermal helium beam spectroscopy system at ASDEX-Upgrade tokamak (AUG)[1]. Figure 1 shows the comparison between the experimentally observed He I line ratios and the collisional radiative modeling at the electron density of  $9.2e+18 \text{ m}^{-3}$  and the electron temperature of 75.2 eV (calculated by Dr. Ralph Dux at IPP). The experimental result is well reproduced. A similar comparison was also made for the He I emission coefficients provided by Open ADAS[2], which has been often used in preceding works. It was found that Open ADAS often fails to match the relative intensities of all four lines being observed at AUG.

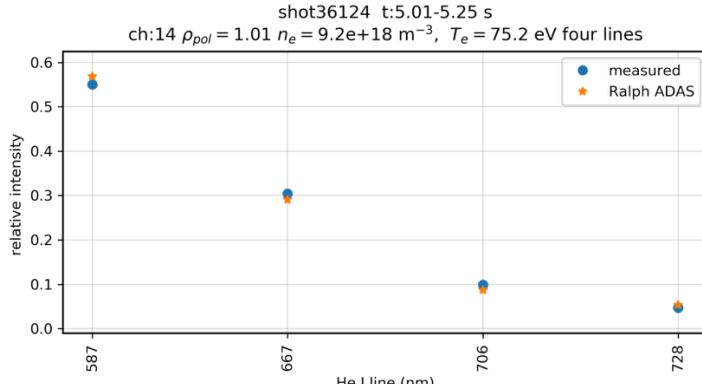


Figure 1. Comparison between the collisional radiative modeling and experimental data of He I lines.

In addition to the atomic models, achieving high time resolution is another major challenge in resolving the two-dimensional turbulence structure. To this end, a new line-ratio analysis technique has been developed[3]. In this technique, a quantity that is only sensitive to either electron density or electron temperature can be constructed by applying arithmetic operations to observed line intensities. Unlike conventional approaches, which utilize only three lines to determine the electron temperature and density, the proposed technique is able to make use of all available line intensities and, thus, improves the signal to noise ratio. The noise contribution

can further be removed by correlating two measurements that probe the same location but are recorded by using independent light-detection systems. By using this technique, the electron density and temperature fluctuation spectra for an EDA H-mode discharge were successfully resolved up to 90 kHz as shown in Fig 2.

The funding of this joint research, which was originally for travel expense, was used for purchasing some parts of the spectroscopy diagnostic system being developed for PANTA and PLATO. This system will be able to provide wide range spectra (200-1050 nm), and further comparison between the atomic models and measurements can be made for Helium and other gases.

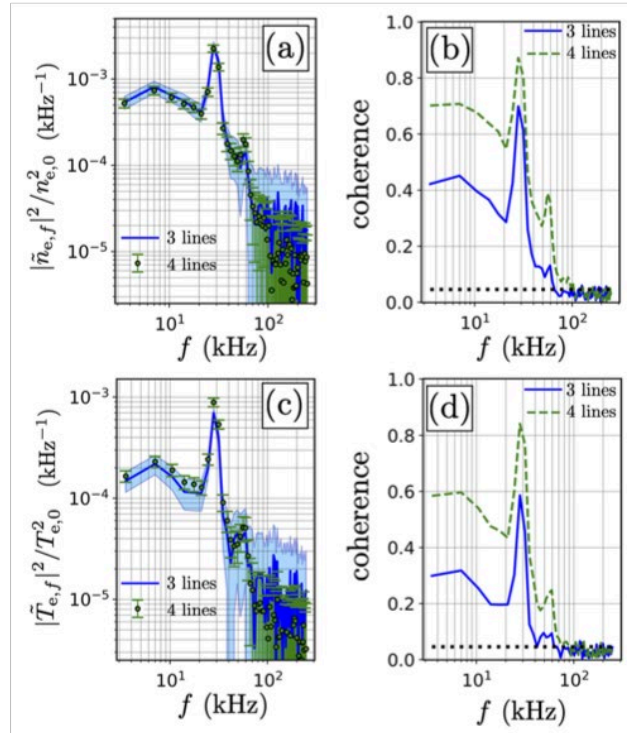


Figure 2 PSDs for the electron density and temperature(a), (c) and their coherence (b), (d).

## Reference

- [1] M. Griener, E. Wolfrum, M. Cavedon, R. Dux, V. Rohde, M. Sochor, J. M. Muñoz Burgos, O. Schmitz, and U. Stroth, Rev. Sci. Instrum. **89**, 10D102 (2018).
- [2] Summers H P 2004 The ADAS User Manual version 2. 6th edn.
- [3] T. Nishizawa, M. Griener, R. Dux, G. Grenfell, D. Wendler, S. Kado, P. Manz, and M. Cavedon, Review of Scientific Instruments **92**, 103501 (2021).

## 国際化推進共同研究概要

No. 10

21NU-9

タイトル: High power mm wave transmission line technology for advanced fusion devices

研究代表者: LECHE Carsten Hanno

所内世話人: 出射 浩

### 研究概要:

国際熱核融合実験炉(ITER)実験では、プラズマパラメータ分布の詳細な細部制御により、燃焼プラズマを閉じ込めることが重要である。電子サイクロトロン加熱・電流駆動では、局所的にプラズマ電流を駆動することで不安定性(磁気島)を抑制することが期待されている。磁気島は kHz~10 kHz 程度の周期でプラズマ断面を回転する。磁気島の回転に併せて局所電子サイクロトロン加熱・電流駆動することで高効率な抑制が可能となる。現在、kHz~10 kHz で入射位置を変えるスイッチ素子が開発中である。九州大学での低電力試験後、量子科学技術研究開発機構(QST)で高電力試験を行ったが、スイッチボックス内でアーキングが発生した。アーキング抑制に向け、スイッチボックス内のミラーを精査し、ミラー面での損傷を確認した。ドイツでのミラー面の再加工に向けた検討・準備、アーキング観測のためのカメラシステムの検討・導入を進めた。

# Report of collaboration between RIAM and IGVP in FY2021: The MQIV FADIS diplexer for ITER with automatic tuning at QST

Mr. Dr. Carsten Lechte

**Introduction:** The MQIV diplexer developed at IGVP is a fast switch, power combiner, and mode filter for 170 GHz using a Fabry-Perot resonator in a compact box design that is vacuum capable and can be directly interfaced with the 63.5 mm ITER ECRH waveguides which are available at QST. Our technical partners at TNO in the Netherlands have designed and built a fast mechanical tuning control unit for the device that is also vacuum-compatible. It uses feedback to fix the output power to either the resonant or the non-resonant output port, compensating for changes in the gyrotron frequency and mechanical expansion of the resonator. The activities of this year have concentrated on improving the high-power compatibility and the calibration of the power monitoring sensors at the input and the two outputs of the diplexer.

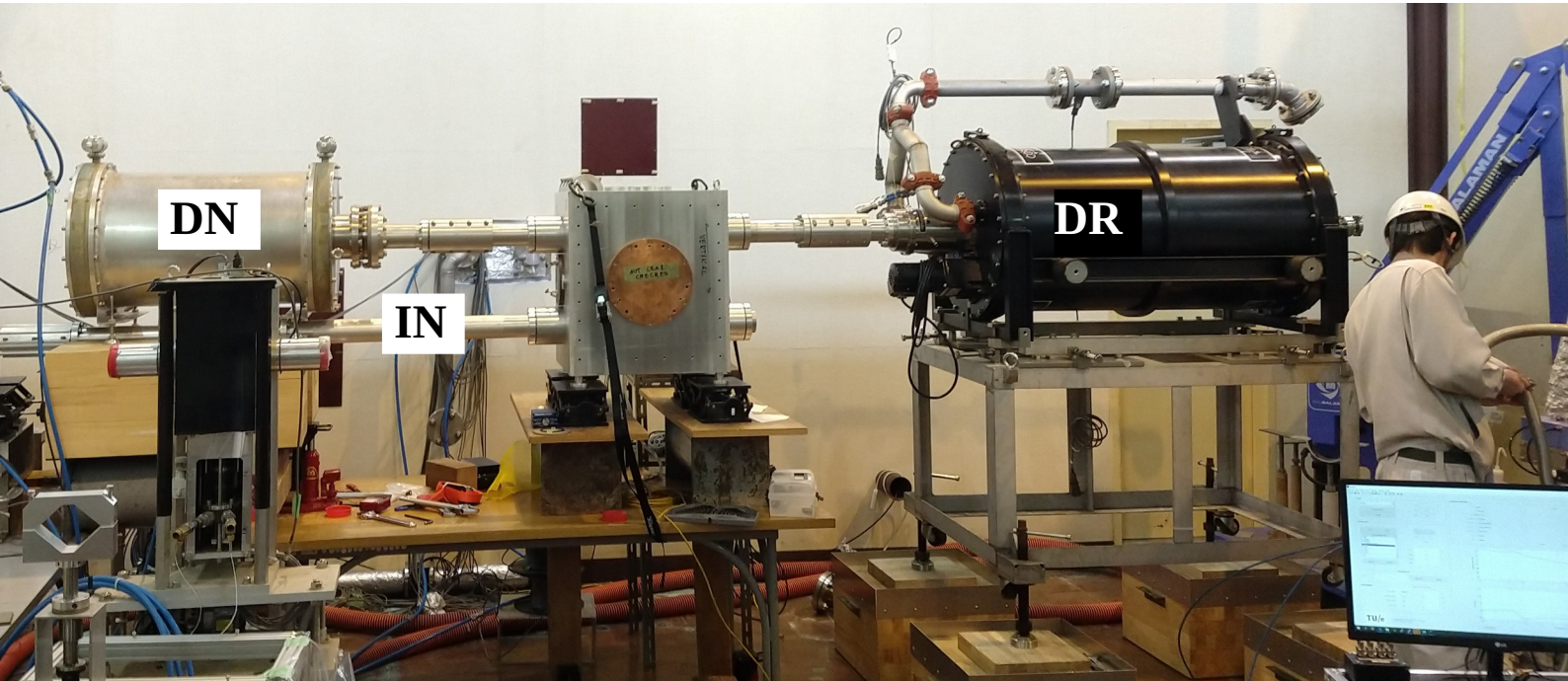


*Fig 1: Diplexer integration into the gyrotron test stand at QST. DN and DR are the dummy loads at the non-resonant and the resonant channel, respectively, and IN is the input waveguide.*

The following problems were identified during testing in 2020: Arcing was happening continuously on the coupling gratings and probably also on the resonator mirrors. In full power operation, such events would necessitate the termination of the pulse, which would make the device unusable. In addition, the stray radiation caused by the arcs was degrading the control test results.

**Since no travel to Japan was possible in 2021,** the work was either of theoretical nature (design and analysis), or parts have to be sent to IGVP for remanufacturing.

**Arc mitigation:** It was found in 2020 after electropolishing of the problematic mirror surfaces, that the material defects in the surfaces were not just irregularities in shape, but there could also be

cavities which outgas material that is then causing the arc. After careful analysis of the video footage from some arcing events, it was decided to return the mirrors to IGPV, where a galvanically deposited “known-good” copper layer will be put down, and the 4 surfaces of the main resonator, which see the greatest incident power, will be remachined. The mirrors are on the way to IGPV.

**Arc detection:** The resonator box has 2 viewports and an additional 4 feedthroughs for cooling lines, which are not currently used for cooling and are fitted with plexiglas windows. All 6 openings can be fitted with cameras to observe a large percentage of the mirror surface area. With stereoscopic vision, we can discriminate between arcs on surfaces and in the volume.

**Improvement of power monitor signal:** The polarisation of the power monitoring horn antennas has been fixed.

**Stray radiation mitigation:** Mounting hardware for holding the absorbing ceramic tiles near the matching mirrors has been devised.

## 国際化推進共同研究概要

No. 11

21RE-1

タイトル： Highly robust and reliable DC breaker based on SiC for the low carbon society

研究代表者： KAMINSKI Nando

所内世話人： 斎藤 渉

研究概要：

SiC Cascode 素子を評価する過電流遮断テストボードの作製を行った。T0-247-3pin パッケージを接続する仕様で、過電圧保護用に最適化された RC スナバ、バリスタを追加することで、被測定素子に余分なストレスが印加されない状況が実現された。オフセット電圧を変化させることで、過電流遮断のトリガレベルを 0~200A の範囲で調整可能などを確認した。

# Highly robust and reliable DC breaker based on SiC for the low carbon society

Nando Kaminski,

The University of Bremen

In 2021, RIAM was provided with an Over Current Breaker (OCB) test board, containing the OCB-FET itself, the JFET in cascode configuration to increase the voltage rating and the overvoltage protection consisting of a varistor and an RC-snubber. RIAM was also provided with the control box generating the required off-set voltages to turn the normally-off MOSFETs into normally-on devices, to control the turn-off threshold and to reset the OCB after it triggered. Both parts together fulfil the task of a controllable overcurrent breaker.

During 2021 this OCB test board has been improved. The latest version is shown in figure 1. The board is equipped with a socket to accommodate a single TO-247-3pin SiC-JFET, which is connected in cascode configuration to increase the voltage rating (centre top). The overvoltage protection consists of an optimised RC-snubber in parallel to a varistor (bottom right). On the left, the LV-OCB with some gate protection is shown. The operation of this board is comparable to previous generations, but achieves less stress on the devices.

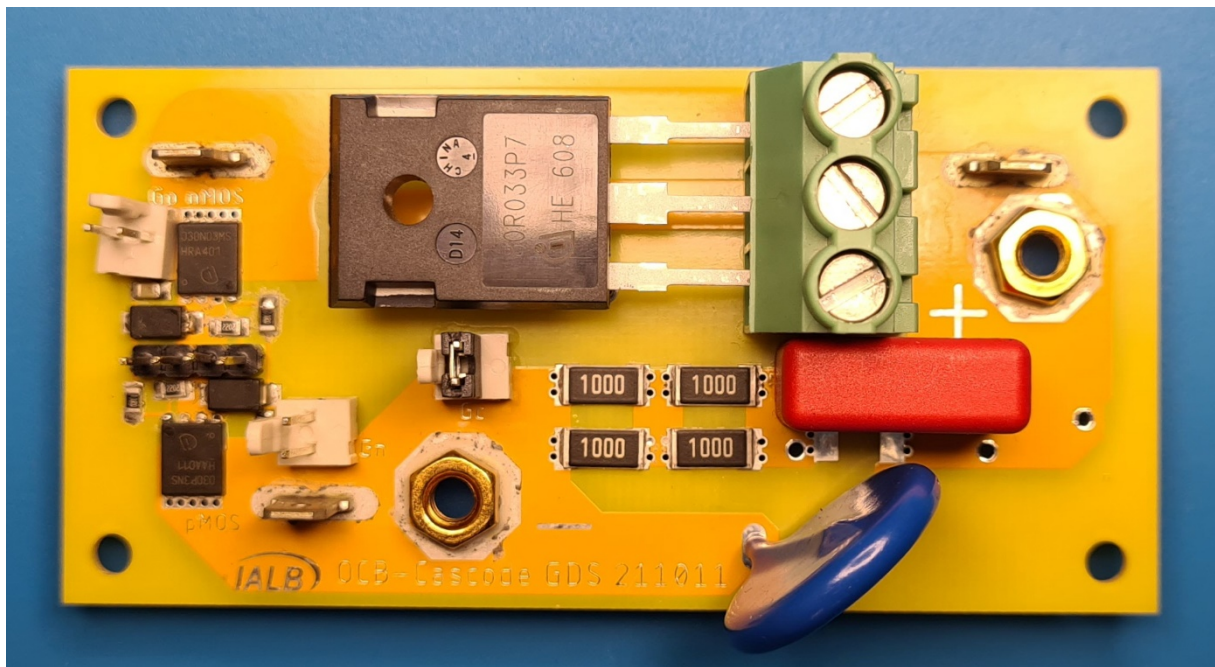


Figure 1: Latest version of the OCB board for accommodating TO247-3pin as the cascoded SiC switch increasing the voltage rating.

Another variant has been designed to accommodate TO-247-4pin SiC-MOSFETs (up to 3 pcs.). The design is shown in figure 2. This version can be used for the 1700V SiC MOSFETs developed within the national project SiC DCBreaker by Infineon Technologies AG. The switching waveforms do not differ significantly, because the transients are determined mostly by the interaction between the overvoltage protection and the outside circuitry, not significantly by the OCB or the cascaded switch.

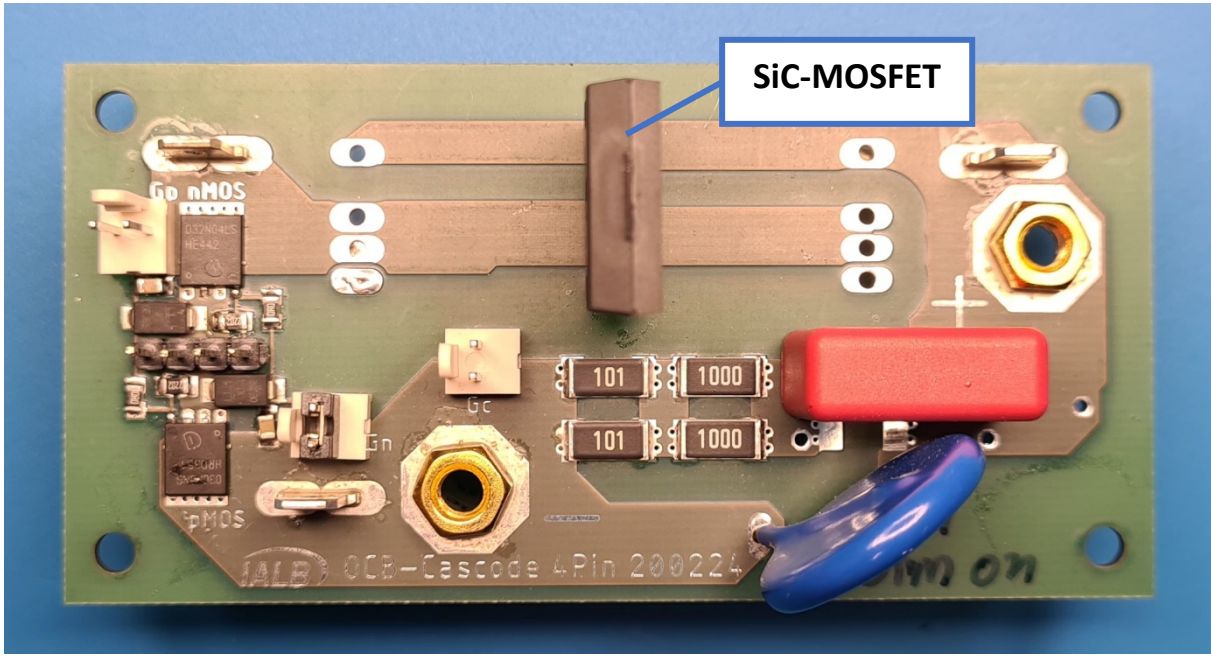


Figure 2: Latest version of the OCB board for accommodating TO247-4pin as the cascoded SiC switch, here a signal experimental 1700V SiC-MOSFET.

The trigger level of the OCB-switch was determined by an automated test bench. Figure 3 shows the trigger level depending on the off-set voltages. In contrast to initial results, the trigger level forms a smooth contour. In other words, the trigger level can be easily controlled by means of the off-set voltages.

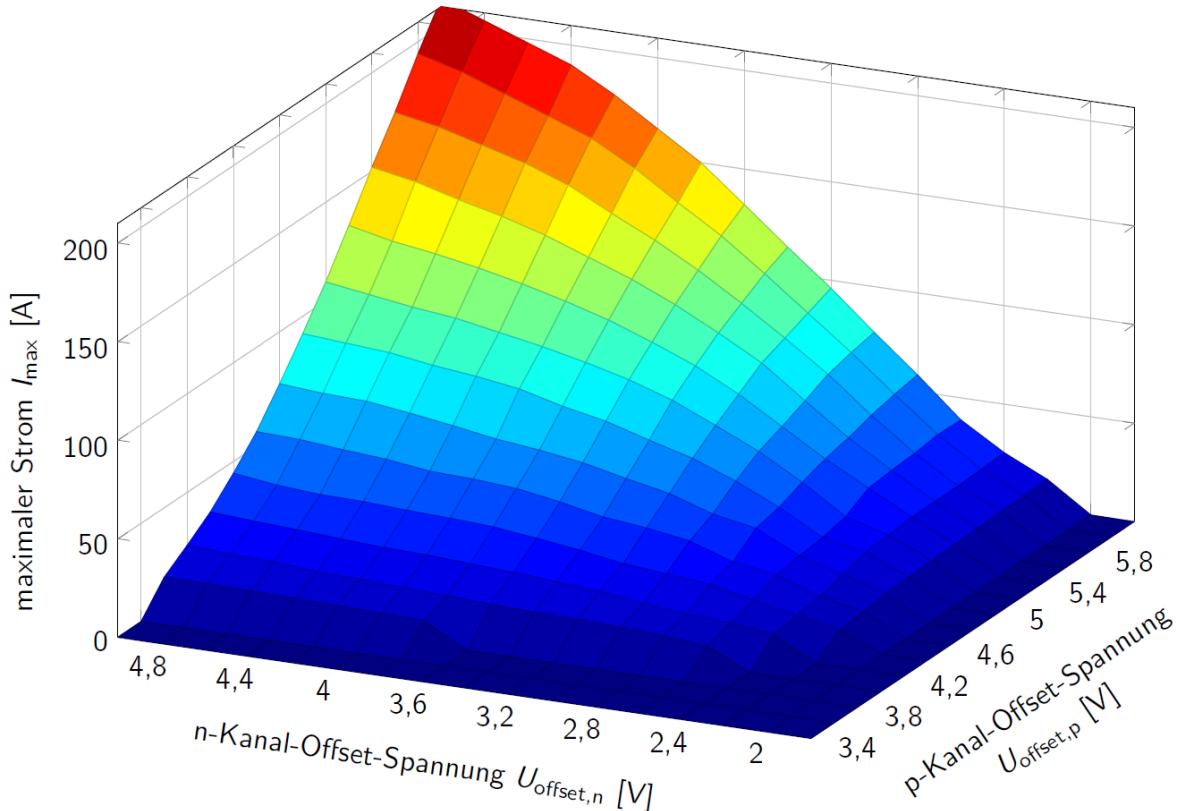


Figure 3: Trigger level of a fully populated OCB test board under various gate-voltage off-sets. The trigger level can be easily controlled.

## 国際化推進共同研究概要

No. 12

21RE-2

タイトル：Flexible energy harvesting system

研究代表者：JEON Insu

所内世話人：東藤 貢

研究概要：

本研究では、天然高分子であるセルロース等の高分子材料と合成高分子を用いて新規ゲル材料の開発を試みた。開発したゲル材料の物理的特性を調べたところ、500MPa に達する弾性率、55MPa の高強度、および 2200s/m の電気伝導性を示した。さらに、-50 °C から 35 °C の温度環境下で 14 日間も優れた物理的特性を維持できることが分かった。開発したゲル材料は次世代のエネルギー用材料としての使用が期待される。

## Flexible energy harvesting system

Chonam National University, Prof. Insu Jeon

### Summary

Next-generation applications, such as flexible electronic devices, sensors, actuators, and soft robotics, require anisotropic functional soft materials with controlled, directional electrical and heat conductivities, mechanical properties, and responsiveness, as well as shape-morphing capability, complex designability, and wide operational temperature ranges. However, a combination of these functions in any single class of materials has been very rarely seen to date. In this study, a novel class of multi-anisotropic gels is developed to realize all these functions through a new fabrication route. The gels are synthesized by integrating cellulose with poly(3,4-ethylenedioxythiophene):poly(styrenesulfonate) (PEDOT:PSS) in tripropylene glycol. The prepared gels exhibit high electrical and thermal conductivities of  $\approx 200 \text{ S m}^{-1}$  and  $\approx 1.49 \text{ W m}^{-1} \text{ K}^{-1}$ , respectively, with exceptional Young's modulus ( $\approx 500 \text{ MPa}$ ) and tensile strength ( $\approx 55 \text{ MPa}$ ), which are much better than the previously reported mechanical properties of PEDOT-based gels (modulus/strength  $\leq 10 \text{ MPa}$ ). Moreover, the gels exhibit self-welding ability and maintain their properties for 14 d over a wide temperature range (from  $-50$  to  $35^\circ\text{C}$ ), covering almost the entire atmospheric temperature range on Earth surface. It is believed that the developed gels are promising candidates for application in many next-generation flexible devices, some of which are experimentally demonstrated in this study.

### Method

First, isotropic water-equilibrated (cellulose/PEDOT:PSS)(x/y) hydrogels were prepared (the detailed procedure is described in the Supporting Information). The hydrogels were subsequently immersed in TriPG for  $\approx 2$  d for solvent exchange, during which TriPG was replaced multiple times to ensure complete exchange of solvent molecules in the gel network. Finally, the gels were stabilized in air at  $\approx 25^\circ\text{C}$  for 1 d to obtain the desired isotropic (cellulose/PEDOT:PSS) TriPG gels, which were then characterized. To prepare the anisotropic (cellulose/PEDOT:PSS) (x/y)@a/b TriPG gels, the corresponding isotropic hydrogels were dried at a process temperature (a) of  $\approx 25$  or  $90^\circ\text{C}$  under clamping at a prestretching strain (b) of 0% or 40% along the length of the gel (x-axis) for 2 d. Thereafter, the gels that dried while clamped were sequentially immersed in water for 1 d and TriPG for  $\approx 2$  d. Finally, the gels were allowed to stabilize by maintaining them under ambient conditions (humidity = 30–70%, temperature  $\approx 25^\circ\text{C}$ ) for 1 d, unclamped, and characterized in detail after placing them in an air atmosphere for  $\approx 2$  h. The data for each type of gel were collected from three measurements and presented as mean values, with the error bars representing the mean absolute deviation ( $n = 3$ ). To compare the properties of the anisotropic gels, the DA was calculated from the absolute ratio of their mean properties between the parallel and perpendicular directions.

### Results

The gels in this study were fabricated via a facile drying and reswelling process, as shown in **Figure 1**. Owing to the synergistic effect of the components, the gels exhibit multi-anisotropic functions, including anisotropic mechanical, electrical, and thermal properties, along with applicability in a wide temperature range (from  $-50$  to  $35$  °C), as well as easy weldability and efficient fabrication of complex and flexible structures.

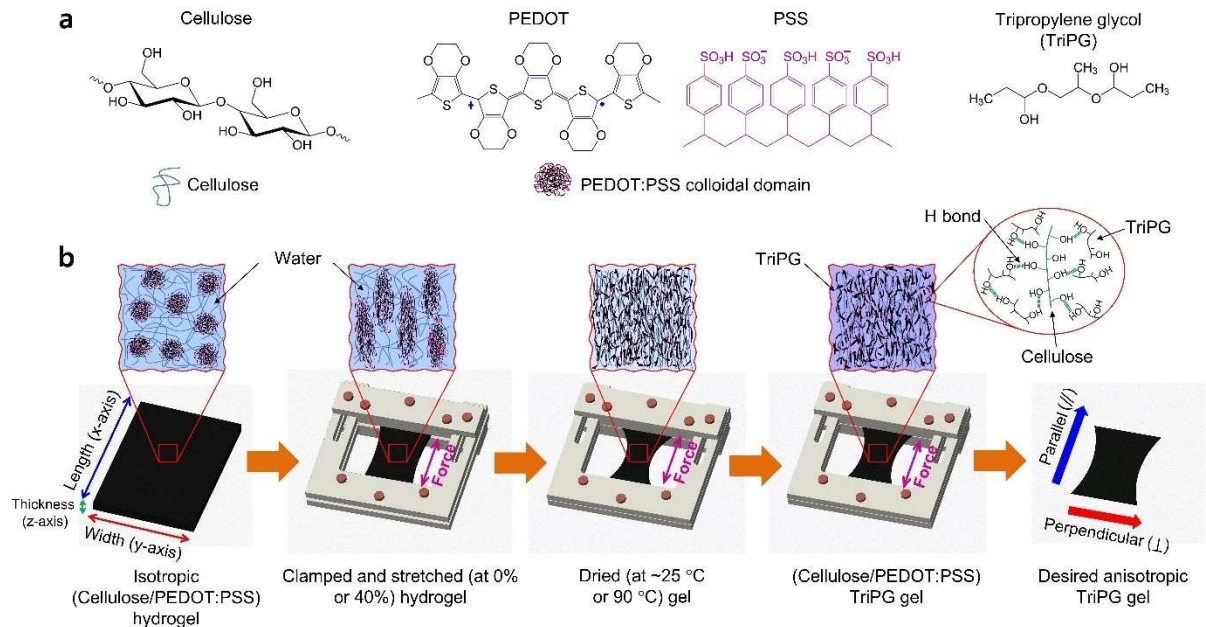


**Figure 1.** (a) Chemical structures of cellulose, PEDOT:PSS, and TriPG. (b) Schematic diagram of the synthesis of the anisotropic (Cellulose/PEDOT:PSS) TriPG gels. The as-prepared (Cellulose/PEDOT:PSS) hydrogel was clamped under a predetermined pre-stretching strain of 0% or 40% along the length direction (x-axis) and was allowed to dry under this confined condition at a temperature of  $\sim 25$  °C or 90 °C. The dried gel was reswelled sequentially in water and TriPG, stabilized in air, and finally unclamped to obtain the desired anisotropic (Cellulose/PEDOT:PSS) TriPG gel, wherein the solvent molecules (TriPG) within gel network were stabilized mostly by intra- and intermolecular hydrogen bonding (H bond) with cellulose polymers.

To determine the optimal composition for the TriPG gels, we prepared a series of (Cellulose/PEDOT:PSS)(x/y) hydrogels and (Cellulose/PEDOT:PSS)(x/y) TriPG gels using the steps illustrated in Figure S1 and analyzed their properties using tensile tests and electrical and thermal conductivity measurements. As the PEDOT:PSS concentration increased from 0 to 1 wt% at a set cellulose concentration of 1.5 wt%, the Young's modulus, tensile strength, and work of extension of the TriPG gels increased gradually, whereas those of the corresponding hydrogels decreased. However, as the cellulose concentration increased from 0.5 to 1.5 wt% at a set PEDOT:PSS concentration of 1 wt%, the mechanical properties of both the TriPG gels and corresponding hydrogels increased gradually. These changes in the mechanical properties of the gels were in agreement with the changes in their final solvent contents. Our compositional study indicated that TriPG can serve as a good solvent for integrating both cellulose and PEDOT:PSS into gel materials despite their highly contrasting chemical structures. While the mechanical properties of the TriPG gels increased proportionally to the concentrations of cellulose and PEDOT:PSS, the mechanical

properties of the hydrogels did not exhibit the same trend. The swelling ratio of the TriPG gels (~80 wt% TriPG content) was lower than that of the corresponding hydrogels (~90 wt% water content); thus, the mechanical properties of the former were superior to those of the latter. Moreover, the highest recorded electrical conductivity of the TriPG gels was higher than that of the hydrogels. Furthermore, cellulose is electrically non-conductive, whereas PEDOT:PSS is highly conductive; consequently, the electrical conductivity of the TriPG gels and corresponding hydrogels strongly depends on the final PEDOT:PSS concentration and PEDOT:PSS-to-cellulose concentration ratio. The final density of PEDOT:PSS in the TriPG gels should be higher than that in the hydrogels because the solvent content of the gels decreased during solvent exchange, which increased the electrical conductivity of the TriPG gels. Increasing the PEDOT:PSS concentration at a set cellulose concentration or decreasing the cellulose concentration at a set PEDOT:PSS concentration led to an increase in the gel electrical conductivity because the PEDOT:PSS-to-cellulose ratio increased. Among the TriPG gels, the (Cellulose/PEDOT:PSS)(1.5/1) TriPG gel presented the best mechanical properties (Young's modulus of  $47.62 \pm 5.52$  MPa, tensile strength of  $7.13 \pm 0.59$  MPa, and work of extension of  $5.55 \pm 1.17$  MJ m<sup>-3</sup>), and the (Cellulose/PEDOT:PSS)(0.5/1) TriPG gel presented the best electrical conductivity ( $10.111 \pm 1.182$  S m<sup>-1</sup>). The (Cellulose/PEDOT:PSS)(1/1) TriPG gel that had excellent mechanical properties (Young's modulus of  $33.28 \pm 6.36$  MPa, tensile strength of  $4.57 \pm 0.36$  MPa, and work of extension of  $3.47 \pm 0.52$  MJ m<sup>-3</sup>) and a reasonably high electrical conductivity ( $5.708 \pm 0.887$  S m<sup>-1</sup>) was selected for further studies.

When cellulose hydrogels are anisotropically dried under confined conditions, well-aligned hierarchical fibrous cellulose structures form along the constraint direction, which afford hydrogels with anisotropic properties after reswelling.<sup>[20]</sup> Moreover, drying induces the crystallization of the PEDOT:PSS colloidal domains. This leads to an increase in the length of the PEDOT:PSS chains, which serve as electrical pathways, and thus significantly increases the electrical conductivity of PEDOT:PSS-based gels.<sup>[45,48]</sup> The gels developed in this study comprised both cellulose and PEDOT:PSS. Therefore, we analyzed the effect of the drying treatment on the gel properties. First, we prepared isotropic pre-dried (Cellulose/PEDOT:PSS)(1/1) TriPG gels by drying the corresponding hydrogels at ~25 °C in the absence of constraints and under biaxial clamping (lengthwise and widthwise) at a strain of 0%, followed by sequential reswelling in water and TriPG and stabilization in air at ~25 °C. The gel without constraints shrank in all directions (length, width, and thickness), whereas only the thickness of the biaxially clamped gel decreased significantly. We determined that the final solvent contents of both pre-dried TriPG gels decreased significantly, and the gels presented isotropic mechanical properties along their lengths and widths. Moreover, the properties of the pre-dried TriPG gels were superior to those of the isotropic TriPG gel prepared without drying the corresponding hydrogel. In particular, the solvent content of the pre-dried TriPG gel after biaxial clamping was ~56 wt%, and the Young's modulus, tensile strength, work of extension, and electrical conductivity were ~4, ~4, ~2, and ~10 times higher, respectively, than those of the corresponding isotropic gel obtained without drying. These results implied that drying the gels induced cellulose aggregation and PEDOT:PSS crystallization, which led to a dramatic decrease in solvent content and a notable improvement to the gel mechanical and electrical properties.

Based on these results, we expected that applying unidirectional constraints to the hydrogels during drying would

induce directional orientation and aggregation of the polymers, which could yield corresponding TriPG gels with multi-anisotropic properties. We prepared unidirectional pre-dried TriPG gels by drying the corresponding hydrogels at  $\sim 25$  °C and clamping them at pre-stretching strains of 0% and 40% along the length direction (Figures 1); these are termed anisotropic (Cellulose/PEDOT:PSS)(1/1)@25/b TriPG gels (where 25 is the process temperature (°C) and *b* is the pre-stretching strain). As the hydrogels were constrained at two ends, their width and thickness decreased significantly during drying, whereas their lengths did not change. This caused aggregation and alignment of the linear rigid polymers (cellulose and PEDOT:PSS) along the length direction in accordance with the principle of “drying in confined condition method,” reported previously.<sup>[20]</sup> The solvent content of the final anisotropic TriPG gels was  $\sim 60$  wt%. The gel properties were analyzed along the directions parallel and perpendicular to the clamping direction, which showed that the gels presented excellent properties, with high degrees of mechanical and electrical anisotropy (**Figures 2a and c**). Increasing the clamping pre-stretching strain from 0% to 40% during drying led to remarkable increases in the stiffness/strength and electrical conductivity and a decrease in the work of extension in the direction parallel to the clamping direction, whereas opposite trends were observed in the direction perpendicular to the clamping direction (Figures 2a, 2c). Moreover, increasing the pre-stretching strain significantly increased the anisotropy. The average Young’s modulus, tensile strength, and electrical conductivity in the direction parallel to clamping for the (Cellulose/PEDOT:PSS)(1/1)@25/0 gel were 2.45, 1.85, and 2.49 times higher, respectively, than those in the direction perpendicular to clamping, whereas those of the (Cellulose/PEDOT:PSS)(1/1)@25/40 gel were up to 6.09, 3.59, and 4.84 times higher, respectively.

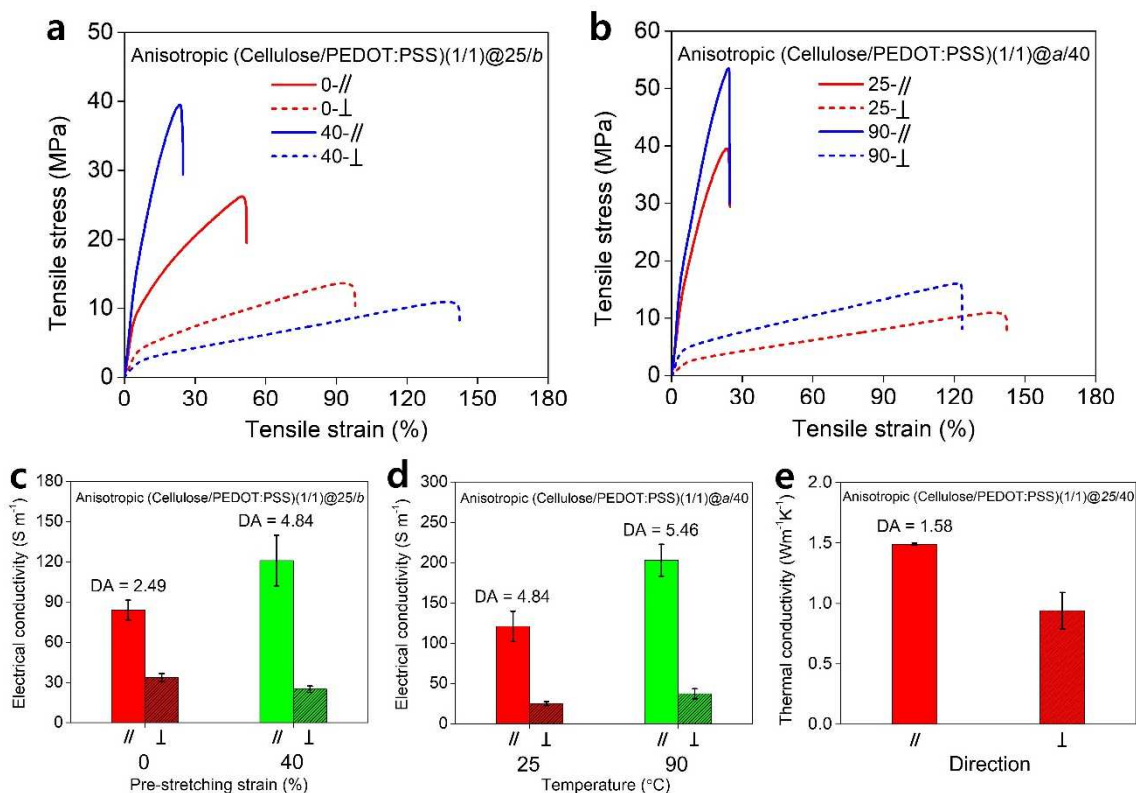


**Figure 2.** Representative tensile stress–strain curves in the directions parallel and perpendicular to clamping of the (a) anisotropic (Cellulose/PEDOT:PSS)(1/1)@25/b TriPG gels prepared by drying the corresponding hydrogels at

$\sim 25$  °C under clamping at pre-stretching strains (*b*) of 0% and 40% and (b) anisotropic (Cellulose/PEDOT:PSS)(1/1)@*a*/40 TriPG gels obtained by drying the corresponding hydrogels at temperatures (*a*) of  $\sim 25$  and 90 °C under clamping at a pre-stretching strain of 40%. (c) and (d) Electrical conductivity in the directions parallel and perpendicular to clamping of the gels in (a) and (b), respectively. (e) In-plane thermal conductivity of the anisotropic (Cellulose/PEDOT:PSS)(1/1)@25/40 gel parallel and perpendicular to the clamping direction. DA values are shown above the plots in (c), (d), and (e).

## Conclusion

We successfully developed a novel class of anisotropic gels by integrating cellulose and PEDOT:PSS, which are bio-friendly, high-value polymers, in TriPG, a green organic solvent. Despite the significant differences in the structures and properties of the two polymers, the novel fabrication method proposed in this study enabled the creation of a hybrid gel with excellent mechanical, thermal, and electrical properties, multiple types of strong anisotropy, self-welding capability, and extremely high stability over a wide temperature range. Furthermore, we demonstrated the suitability of the prepared gels for fabricating complex flexible electrical circuits, flexible connectors, and solvent sensors. Through the extensive study of changing the composition of cellulose, PEDOT:PSS, and TriPG, as well as other parameters like pre-stretching strain and process temperature, (Cellulose/PEDOT:PSS)(1/1)@90/40 TriPG gel was determined to be the optimal anisotropic gel. Considering these remarkable properties and facile synthesis, the developed gels are expected to have a high potential for numerous applications in next-generation flexible devices.

## 国際化推進共同研究概要

No. 13

21RE-3

タイトル： Numerical Wave Tank for Floating Offshore Wind Turbine Structures

研究代表者： WAN Decheng

所内世話人： 胡 長洪

研究概要：

本国際化推進共同研究について、共同研究・研究集会とも予定通り実施した。共同研究について、浮体式洋上風車の波浪中性能や、風車間干渉などの問題に対して数値シミュレーションに関する検討が行われ、関連の研究成果は 8 編の国際学会論文に纏められ採択された。R4 年 1 月 21 日にオンライン国際研究集会「The 3rd International Symposium on Novel Computational and Experimental Methods for Complicated Fluid-Structure Interactions」が開催され、外国から 30 名、日本から 26 名の参加者があり、流体・構造連成解析問題に関する数値解析方法及び水槽実験方法の高精度化・高効率化に関して有意義な国際研究集会となった。

*Report for 2021 RIAM International Joint Research Project*

[21RE-3]

## Numerical Wave Tank for Floating Offshore Wind Turbine Structures

Decheng Wan

School of Naval Architecture, Ocean and Civil Engineering, Shanghai Jiao Tong University, China

### 1. Purpose

Offshore Wind Turbine (OWT) is considered as one of the most promising renewable energy sources from ocean. The OWT is exposed to severe ocean environment such as typhoon (hurricane) and extreme waves, and has to be designed to withstand those ocean environments. During the design, the evaluation of the environmental loading on the OWT has been relying on the empirical simulation tools and the physical wave tank model test. Recently, there has been breakthrough in the physics-based simulation of offshore platforms, which is called as the Numerical Wave Tank (NWT). The NWT is considered to replace partly the physical tank model test in the near future for OWT design. This joint research project focuses on some important research topics in NWT development, and provides an opportunity for researchers, especially younger researchers, including but not limited to SJTU and RIAM, to exchange their knowhow on their researches.

### 2. Research Plan

The major research topics of this joint research project is new CFD solver development, large scale parallel simulation technique, fluid-structure interaction simulation, fully-nonlinear wave model for ocean waves, and advanced wind modeling, etc. CFD codes which are developed in SJTU and RIAM will be compared to the experiments. In the end of 2021, as the main event of this international joint research project, the 3rd International RIAM Symposium on Novel Computational and Experimental Methods for Complicated Fluid-Structure Interactions will be carried out. Researchers involved in this joint research project will present and discuss their research progresses.

The members involved in this collaborative research are shown in the following table.

Researcher's Name	Name of University or Institute	Present Status or Grade (graduate students)	Researcher role
Decheng Wan	SJTU	Professor	Representative person (CFD )
Jianhua Wang	SJTU	Assistant Professor	Co-researcher (CFD)
Cheng Liu	SJTU	Associate Professor	Co-researcher (CFD)
Weiwen Zhao	SJTU	Assistant Professor	Co-researcher (CFD)
Liushuai Cao	SJTU	Assistant Professor	Co-researcher (CFD)
Xiaosong Zhang	SJTU	PhD student	Co-researcher (CFD)
Zhiqiang Liu	SJTU	PhD student	Co-researcher (CFD)
Chongyi Huang	SJTU	PhD student	Co-researcher (CFD)
Seiya Watanabe	RIAM	Assistant professor	Co-researcher (CFD)

Mohamed M. Kamra	RIAM	Research Fellow	Co-researcher (CFD)
Hongzhong Zhu	RIAM	Research Fellow	Co-researcher (Experiment)
Changhong Hu	RIAM	Professor	RIAM Attendant

### 3. Summary of Collaboration Research

In 2021, due to the international travel restriction, research discussions have been made online. Main topics that have been studied include (1) numerical simulation of asymmetrical wake flows of a yawed wind turbine; (2) numerical analysis of aero-hydrodynamic responses of floating offshore wind turbine considering blade deformation; (3) numerical investigations of wake flows of counter-rotating wind turbines in shear inflows; and (4) forces prediction of a hydrofoil by combined machine learning and CFD approach. The research results have been presented at the 2021 ISOPE conference and the 3rd International Symposium on Novel Computational and Experimental Methods for Complicated Fluid-Structure Interactions.

International conference papers related to this joint research project in 2021 are listed as follows.

- 1) Dezhi Wei; Decheng Wan; Changhong Hu: Numerical Simulations of Asymmetrical Wake Flows of a Yawed Wind Turbine, Proc. the 31st International Ocean and Polar Engineering Conference, Rhodes, Greece, June 2021. Paper Number: ISOPE-I-21-1193
- 2) Chunhui Ma; Decheng Wan; Changhong Hu: Numerical Study of Passive Control of Flow-Induced Oscillation of Cylinder with Symmetric Strips, Proc. the 31st International Ocean and Polar Engineering Conference, Rhodes, Greece, June 2021. Paper Number: ISOPE-I-21-3226
- 3) Yang Huang; Decheng Wan; Changhong Hu: Numerical Analysis of Aero-Hydrodynamic Responses of Floating Offshore Wind Turbine Considering Blade Deformation, Proc. the 31st International Ocean and Polar Engineering Conference, Rhodes, Greece, June 2021. Paper Number: ISOPE-I-21-1197
- 4) Heming Bai; Yang Huang; Decheng Wan; Changhong Hu: Numerical Investigations of Wake Flows of Counter-Rotating Wind Turbines in Shear Inflows, Proc. the 31st International Ocean and Polar Engineering Conference, Rhodes, Greece, June 2021. Paper Number: ISOPE-I-21-1198
- 5) Minsheng Zhao; Decheng Wan; Changhong Hu: Numerical Simulation of Propeller Cavitation Flows in Non-Uniform Flow Fields, Proc. the 31st International Ocean and Polar Engineering Conference, Rhodes, Greece, June 2021. Paper Number: ISOPE-I-21-4147
- 6) Hao Hu; Di Deng; Decheng Wan; Changhong Hu: Numerical Analysis of Vortex-Induced Vibrations of a Slender Flexible Riser under Platform Motions, Proc. the 31st International Ocean and Polar Engineering Conference, Rhodes, Greece, June 2021. Paper Number: ISOPE-I-21-3220
- 7) Songtao Chen; Weiwen Zhao; Decheng Wan; Changhong Hu: Numerical Investigation of Vortex-Induced Motions of a Circular Cylinder with Free Surface, Proc. the 31st International Ocean and Polar Engineering Conference, Rhodes, Greece, June 2021. Paper Number: ISOPE-I-21-3219
- 8) Hongjie Cao; Decheng Wan; Changhong Hu: Forces Prediction of a Hydrofoil by Combined Machine Learning and CFD Approach, Proc. the 31st International Ocean and Polar Engineering Conference, Rhodes, Greece, June 2021. Paper Number: ISOPE-I-21-3176

As a main event of this international joint research project, ‘The 3rd International Symposium on Novel Computational and Experimental Methods for Complicated Fluid-Structure Interactions’ has been held on January 21, 2022. Due to the global pandemic situation of COVID-19, the symposium was held online. On the symposium, overseas and domestic scholars were invited to present their recent researches on their recent research results on development of computational and experimental methods for complicated fluid-structure interactions. The program of the symposium is as follows.

## The 3rd International Symposium on Novel Computational and Experimental Methods for Complicated Fluid-Structure Interactions

Date: January 21, 2022

Place: Zoom Meeting Room (From 9:00 Japan time)

Organized by Research Institute for Applied Mechanics, Kyushu University

### TIME TABLE

9:50 -10:00	Opening Address by Changhong Hu
<b>Session 1      High Performance Numerical Method</b>	
10:00 - 10:30	<b>Yingyi Liu</b> (RIAM, Kyushu University) Computational Accuracy and efficiency for Diffraction Transfer Matrix using Hybrid Source-dipole Formulations
10:30 - 11:00	<b>Zhiteng Gao</b> , Ye Li (Shanghai Jiao Tong University, China) Validation and Improvement of Actuator Line Model in the Large-Eddy Simulation of Wind-Turbine Wakes
11:00 - 11:30	<b>Lei Tan</b> (RIAM, Kyushu University) Motion and Load Characteristics of a Barge-Type Vertical-Axis Floating Wind Turbine with Moonpools
11:30 - 12:00	<b>Tomoaki Hirakawa</b> (Akita University) Improved BEM Simulation for Wave-Body Interactions by Elastic Mesh Techniques
12:00 - 13:00	Lunch break

**Session 2      Tidal Current and Wave Energy**

13:00 - 13:40	<b>Daisaku Sakaguchi</b> , Reiko Yamada, Yusaku Kyozuka (Nagasaki University) <u>Invited Lecture</u> Design Optimization of Tidal Current Turbines by Meta-model Assisted Genetic Algorithms
13:40 - 14:10	<b>Mohamed Kamra</b> , Rui Yamamoto, Changhong Hu (RIAM, Kyushu University) Application of Machine Learning to Wake Prediction of Tidal Current Turbine
14:10 - 14:40	<b>Patxi Garcia Novo</b> (Nagasaki University) Tidal Stream Energy as a Potential Continuous Power Producer: A Case Study for West Japan
14:40 - 15:10	<b>Peiwen Cong</b> (Dalian University of Technology, China) Numerical Evaluation of the Hydrodynamic Performance of Multi-Degree-of-Freedom Floating Oscillating Water Column (OWC) Devices

15:10 - 15:20	Break
---------------	-------

**Session 3      Offshore Wind Energy**

15:30 - 16:00	<b>Dezhi Wei</b> , Decheng Wan (Shanghai Jiao Tong University, China) Analytical Modeling of Multiple Yawed Turbine Wakes: Considering the Effects of Transverse Wake Velocity
16:00 - 16:30	<b>Xiaobo Zheng</b> , Ye Li (Shanghai Jiao Tong University, China) Aerodynamic Response of a Pitching Foil to Vortex Shedding - Some Inspiration for the Vertical-Axis Wind Turbine
16:30-17:00	<b>Ali Alkhabbaz</b> , Ho-Seong Yang, Watchara Tongphong, Young-Ho Lee (Korea Maritime & Ocean University, Korea) Aerodynamic Performance Analysis of Floating Wind Turbine Experiencing Platform Surge Motion
17:00 - 17:30	<b>Nitin Thulkar</b> (Chartered Engineer IET, UK) A Unified Seakeeping and Maneuvering Analysis of Multiple Linked Towing System with Triangular Bodies
17:30 - 18:10	<b>Zhiqiang Hu</b> (Newcastle University, UK) <u>Invited Lecture</u> Application of SADA Method on Dynamic Performances Analysis of FOWT : Case of Study with Full-Scale Hywind Data

18:10 - 18:20	Closing Address by Decheng Wan
---------------	--------------------------------

## 国際化推進共同研究概要

No. 14

21RE-4

タイトル： Software-in-the-Loop combined Artificial Intelligence method for Dynamic Response Analysis of FOWTs

研究代表者： HU Zhiqiang

所内世話人： 胡 長洪

研究概要：

浮体式洋上風力発電システム用のセミサブ型浮体の運動特性解析に Software-in-the-Loop 法と AI 技術を応用する国際化推進共同研究について今年度は予定通り実施した。特に、SADA 手法に対して検討を行い、有望な成果が得られた。R3 年 1 月に応研で開催されたオンライン国際研究集会「The 3rd International Symposium on Novel Computational and Experimental Methods for Complicated Fluid-Structure Interactions」に参加し、「Application of SADA Method on Dynamic Performances Analysis of FOWT : Case of Study with Full-Scale Hywind Data」のタイトルで共同利用成果の発表を行い、参加者との研究交流を行った。

*Report for 2021 RIAM International Joint Research Project*

[21RE-4]

**Software-in-the-Loop combined Artificial Intelligence method for Dynamic Response Analysis of FOWTs**

Zhiqiang Hu

Marine, Offshore and Subsea Technology, School of Engineering, Newcastle University, UK

During year of 2021, although we couldn't attend the RIAM symposium at Kyushu University in person due to pandemic, but international collaborations were conducted steadily. Zhiqiang Hu attended the RIAM symposium online in Jan 2021, and gave a presentation on the topic of SADA, a new innovative AI-based methodology for dynamic performance analysis of floating offshore wind turbines. After the symposium, Zhiqiang Hu led his research team and continued investigation on AI+FOWTs, especially the engineering application of SADA on FOWTs. During the year of 2021, the collaborative research outcomes are listed as below.

- 1) The 3rd International Symposium on Novel Computational and Experimental Methods for Complicated Fluid-Structure Interactions is planned to be held online at RIAM Kyushu University in Jan 2022. Zhiqiang Hu has agreed to attend and will give a presentation on the topic of 'Application of SADA method on Dynamic Performances Analysis of FOWT: Case of Study with Full-Scale Hywind Data'.
- 2) During year 2021, the collaborative research is carried out to conduct engineering applications of the Artificial Intelligence knowledge-based method, SADA, on the full-scale measurement data of FOWT. This investigation also received the kind support from ORE Catapult UK, as they provided the valuable full-scale measurement data from Hywind FOWT in Scotland. The SADA method was applied to perform numerical optimization and dynamic responses prediction of the FOWTs, based on the full-scale data from one FOWT in Hywind Farm. The numerical model imbedded in SADA was trained to be intelligent for the objective Hywind FOWT under different sea states, and then it can be used to do more prediction and analysis.
- 3) Based on the research in year 2021, a collaborative conference paper entitled 'Dynamic Performance Prediction of Hywind Floating Wind Turbine based on SADA Method and Full-Scale Measurement Data' has been accepted to be published on MARTECH Conference 2022. Prof Changhong Hu is the co-author of this paper. At this moment, the paper is under the revision status. If it can be accepted, it will be presented in May 2022.

**1. RIAM international symposium**

The 3rd International Symposium on Novel Computational and Experimental Methods for Complicated Fluid-Structure Interactions was held online on 21st Jan 2022. Zhiqiang Hu attended this symposium and gave a presentation on the topic of 'Application of SADA method on Dynamic Performances Analysis of FOWT: Case of Study with Full-Scale Hywind Data'.

This presentation introduced the latest collaborative research outcomes of Zhiqiang Hu and Changhong Hu's research teams on FOWTs during year 2021. This presentation introduced the structure of SADA methodology and its first successful engineering application on one FOWT at Hywind Scotland Farm. After the presentation, Zhiqiang Hu made fruitful discussions with others who were interested in this new method. After the symposium, professor Changhong Hu and Zhiqiang also made a detailed discussion and confirmed to continue the collaborative research in the field of AI+FOWTs in the year 2022.

## **2. Collaborative research on AI technology for FOWTs**

In the year of 2021, a collaborative research on the engineering application of AI-based technology for dynamic responses analysis of FOWTs was conducted well. This study started with introducing a case study for the dynamic performance analysis of Hywind FOWT by using full-scale data through the application of SADA. The full-scale data used was collected by one of Hywind FOWTs in Scotland. The analysis of dynamic performance of FOWT can be optimized by using the trained SADA model in terms of platform motions, tower top, and blade tip deformation. The analysis results show that SADA can predict the Hywind supporting floater motions with high accuracy, although some design parameters are not accessible. Based on the comparison and validation of platform motion predictions, it can be proved that SADA is a reliable and cost-effective method for dynamic performance analysis of FOWTs. In summary, the SADA method can bring an innovative vision for FOWTs' full-scale measurement technology in engineering applications.

In addition, thanks for the support and collaboration in 2021, a collaborative conference paper submitted to MARTECH Conference 2022. The paper is titled 'Dynamic Performance Prediction of Hywind Floating Wind Turbine based on SADA Method and Full-Scale Measurement Data'. This paper has been accepted for publication and the first author will give a presentation on MARTECH2022 conference.

In year 2022, the collaborative research between Newcastle University and Kyushu University will be conducted to a further step. The research will be extended to FOWT design field, and it is expected that a new design method, named Interactive Integrated Design method will be proposed, based on AI+FOWTs SADA method. In UK, there are quite a lot opportunities for the development of FOWTs designs in the coming years, but design methods are not mature enough to support design of large offshore wind turbine. Therefore, the collaborative research on FOWT design has a promising future. The AI technology application in offshore renewable energy is also the strong side of Professor Changhong Hu's research team. It is expected there will be fruitful research outcomes in year 2022.

## 国際化推進共同研究概要

No. 15

21RE-5

タイトル : Joint study on the next generation of high frequency with controllability and reliability in power semiconductor device technologies

研究代表者 : EKKANATH MADATHIL Sankara Narayanan

所内世話人 : 斎藤 渉

研究概要 :

1. 2kV 系のトレンチ IGBT とトレンチクラスターIGBT の比較を三次元 TCAD シミュレーションを用いて行った。オン電圧—ターンオフ特性の比較に加えて、ターンオン損失比較を行った。トレンチクラスターIGBT では、高い電流増幅率によるターンオン損失低減に加えて、PMOS 動作による負性容量の抑制が得られる。これらの効果から損失トレードオフも改善される。加えて、三次元スケーリング設計によるターンオン動作の解析も行った。シミュレーション結果からターンオン損失の劇的な減少を確認し、150°C 動作において、 $k=3$  のスケーリングにより電力損失を 40% 低減できるという結果が得られた。

# Joint study on the next generation of high frequency with controllability and reliability in power semiconductor device technologies

Sankara Narayanan Ekkannath Madathil

The University of Sheffield, United Kingdom

## Abstract

In this paper, performances of 1.2-kV Trench IGBT (TIGBT) and Trench Clustered IGBT (TCIGBT) are compared through 3-D TCAD simulations. Comparative on-state and turn-off performances have been reported previously. Herein we show much lower turn-on loss ( $E_{on}$ ) of TCIGBT due to its higher current gain and the negative gate capacitance effect is effectively suppressed by the self-clamping feature and PMOS actions in comparison to the TIGBT. In addition, the impact of 3-D scaling rules on turn-on performance is analyzed in detail. Simulation results show significant reduction of  $E_{on}$  in both TIGBT and TCIGBT. The k3-TCIGBT shows a 40% reduction of power loss compared to the k3-TIGBT at 150°C.

## 1. Introduction

The trends in the development of silicon MOS-Bipolar devices are devoted to increase in power density as well as power efficiency. Remarkable efforts have been made to improve the turn-off energy loss ( $E_{off}$ ) versus on-state voltage drop ( $V_{ce(sat)}$ ) trade-off. For example, the 3-D scaling concepts on TIGBT [1, 2] and Trench Clustered IGBT (TCIGBT) [3], as shown in Fig. 1, have resulted in significant improvement of  $E_{off}$ - $V_{ce(sat)}$  trade-off. Due to the enhanced thyristor effect, the scaled TCIGBT shows even lower  $V_{ce(sat)}$  than the scaled TIGBT, as shown in Fig. 2. Moreover, Fig. 3 shows that the PMOS actions enable the TCIGBTs to show lower  $E_{off}$  than the TIGBTs. Recently, the TCIGBTs have been experimentally evaluated to show Dynamic Avalanche (DA) free behavior and low power loss at high current density operations [4-6]. In addition to the on-state and turn-off behavior, the turn-on performance is also important for TIGBTs and TCIGBTs to achieve high switching frequency with low power loss. In this paper, the turn-on behavior of TIGBT and TCIGBT are studied via 3-D TCAD simulations [7]. Furthermore, the impacts of 3-D scaling rules on the turn-on performance of TIGBT and TCIGBT are analyzed in detail.

## 2. Comparison of Turn-on Performance

The cross-sections of the TIGBT and TCIGBT are shown as the  $k1$  structures in Fig. 1. The threshold voltages are kept identical to compare the turn-on performance. A double pulse inductive test circuit as shown in Fig. 4 is used to simulate the switching behavior. Fig. 5 compares the turn-on waveforms at rated current and identical gate resistance ( $R_g$ ). It can be seen that TCIGBT shows much higher turn-on  $dI/dt$  and  $dV/dt$  than the TIGBT. This is because the thyristor structure

within TCIGBT exhibits a higher current gain than the BJT structure within TIGBT, as expressed in Equations (3) and (4). Therefore, TCIGBT shows much lower turn-on energy loss ( $E_{on}$ ) than the TIGBT. In addition, in the TIGBT, the P-float potential ( $V_{PF}$ ) rises up during turn-on. The voltage difference across the gate oxide ( $V_{PF} - V_{ge}$ ) can induce a reverse displacement current to charge the gate capacitance to a negative value, which has a significant impact on the  $dV/dt$  and  $dI/dt$  controllability [8]. Fig. 6 shows the  $V_{PF}$  and  $V_{ge}$  of TIGBT and TCIGBT during turn-on while Fig. 7 compares the potential distribution and hole current flowlines when  $I_c = 100$  A and  $V_{ce} = 600$  V. It is shown that there is a significant potential difference between  $V_{PF}$  and  $V_{ge}$  in the TIGBT, which is caused by the current flow within the P-float region. However, in the TCIGBT, the P-base potential is clamped under a low value due to the self-clamping feature and the hole current is evacuated through the PMOS directly. Hence, the potential difference across the gate oxide is marginal and the negative gate capacitance effect is therefore successfully suppressed.

## 3. Impact of Scaling Rules on Turn-on Performance

Fig. 8 compares the switching waveforms and gate charge ( $Q_g$ ). As shown, the  $Q_g$  is scaled in k3-TIGBT due to the scaled trench gate while the  $dV/dt$  and the  $dI/dt$  of k3-TIGBT are increased compared to that of k1-TIGBT due to reduced input capacitance, as shown in Fig. 9 and Fig. 10. Hence, the scaling rules result in significant reduction of  $E_{on}$  in both TIGBT and TCIGBT, as shown in Fig. 11. Due to suppression of negative gate capacitance, better turn-on  $dI/dt$  controllability with respect to the  $E_{on}$  of TCIGBT compared with TIGBT is shown in Fig. 12. At  $dI/dt = 5$  kA/ $\mu$ s, k3-TCIGBT shows a 70% reduction of  $E_{on}$  compared to that of k3-TIGBT. Fig. 13 compares the total power loss of TIGBTs and TCIGBTs. As shown, scaling rules result in a 10% reduction of total power loss in both TIGBTs and TCIGBTs. k3-TCIGBT shows a 40% reduction of  $E_{on}$  compared to k3-TIGBT at  $T_j = 425$  K.

## 4. Conclusions

The behavior of TIGBT and TCIGBT with scaling design are studied. The negative gate capacitance is suppressed in the TCIGBT due to the self-clamping feature. The scaling rules on TIGBT and TCIGBT reduce  $E_{on}$  significantly. The k3-TCIGBT shows high power efficiency due to enhanced thyristor effect and good switching controllability.

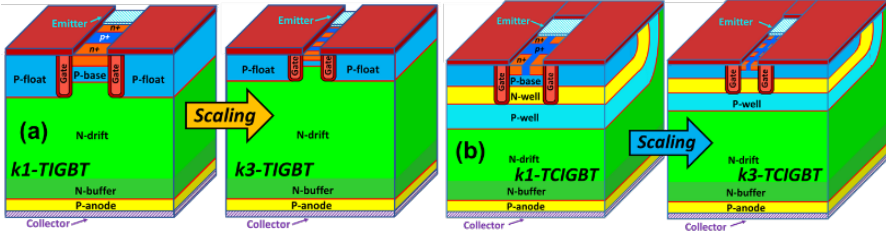


Fig. 1. Scaling concepts on (a) TIGBT [1] and (b) TCIGBT [3].

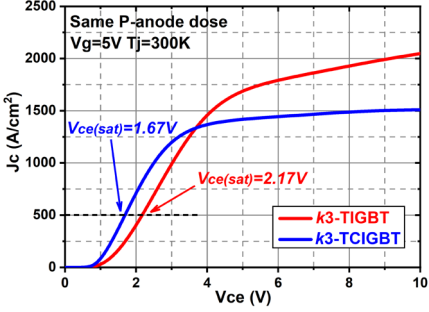


Fig. 2. Comparison of I-V performance.

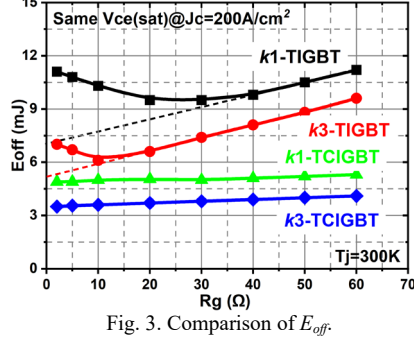


Fig. 3. Comparison of  $E_{off}$ .

$$\text{TIGBT} \quad \frac{dV_{CE}}{dt} = \frac{V_g - (V_{th} + \frac{1-\alpha_{PNP}}{g_m} I_c)}{R_g \times C_{gc}} \quad (1)$$

$$\frac{dI_c}{dt} = \frac{g_m(V_{g,in} - V_g)}{(1-\alpha_{PNP})(R_g \times C_{ge})} \quad (2)$$

$$\text{TCIGBT} \quad \frac{dV_{CE}}{dt} = \frac{V_g - [V_{th} + \frac{(1-\alpha_{PNP})(1-\alpha_{NPN})}{g_m} I_c]}{R_g \times C_{gc}} \quad (3)$$

$$\frac{dI_c}{dt} = \frac{g_m(V_{g,in} - V_g)}{(1-\alpha_{PNP})(1-\alpha_{NPN})(R_g \times C_{ge})} \quad (4)$$

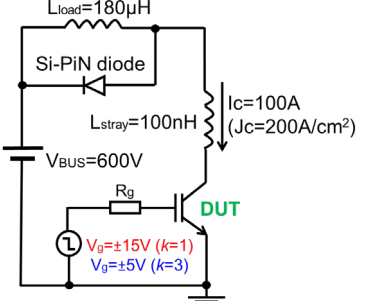


Fig. 4. Test circuit configuration.

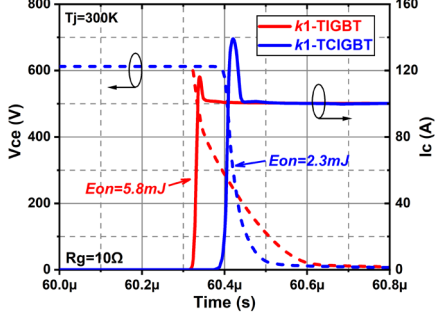


Fig. 5. Comparison of turn-on performance.

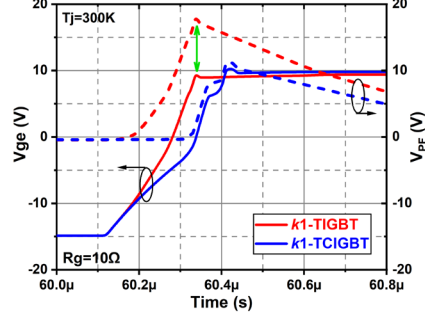


Fig. 6. Comparison of  $V_{PF}$  and  $V_{ge}$  during turn-on.

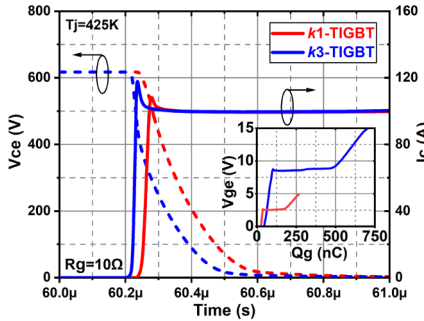


Fig. 8. Comparison of turn-on waveforms.

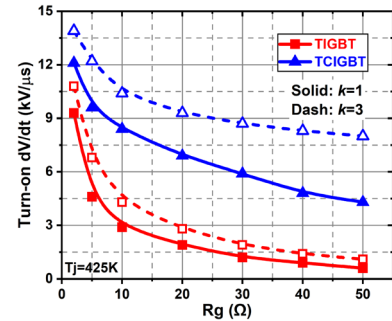


Fig. 9. Comparison of turn-on  $dV/dt$ .

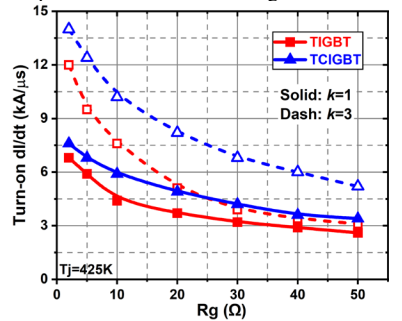


Fig. 10. Comparison of turn-on  $dI/dt$ .

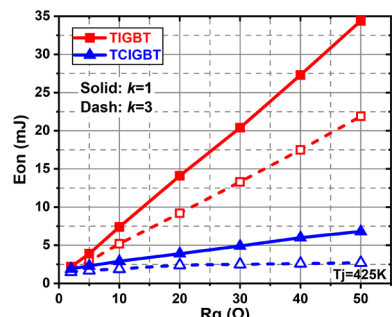


Fig. 11. Comparison of turn-on energy loss.

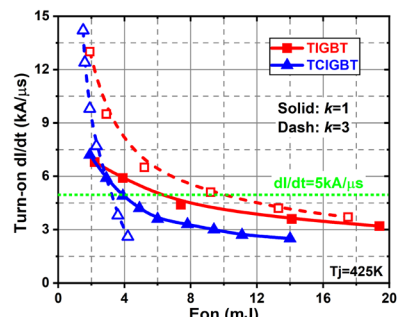


Fig. 12. Comparison of  $dI/dt-E_{on}$  trade-off.

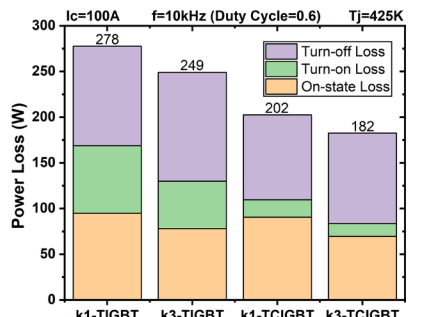


Fig. 13. Comparison of total power loss.

- References:** [1] K. Kakushima, et al., IEDM 2016, pp. 10.6.1-10.6.4. [2] T. Saraya, et al., IEDM 2018, pp. 8.4.1-8.4.4. [3] P. Luo, et al., *IEEE Trans. Electron Devices*, vol. 65, pp. 1440-1446, 2018. [4] P. Luo, et al., IEDM 2019, pp. 12.3.1-12.3.4. [5] P. Luo, et al., *IEEE Trans. on Electron Devices*, vol. 67, pp. 3691-3697, 2020. [6] P. Luo, et al., *IEEE Trans. on Power Electronics*, vol. 36, pp. 3304-3311, 2021. [7] I. Synopsys, Sentaurus Device User Guide: Version R-2020.09. [8] Y. Onozawa, et al., *IEEE Trans. on Industry Applications*, vol. 43, pp. 513-519, 2007.

## 国際化推進共同研究概要

No. 16

21RE-6

タイトル : Predictions of the wave power absorption by a large Floating Oscillating Water Column (OWC) wave energy converter based on a Higher-order Boundary Element (HOBEM) method

研究代表者 : CONG Peiwen

所内世話人 : 劉 盈溢

研究概要 : この研究では、複雑な形状の振動水柱（OWC）発電装置の流体力学的解析のため、数値方法が開発された。物理的には、デバイスが自由に移動したり波に係留されたりする状況では、チャンバー内の気流の動きが、内部の流体表面の変化およびデバイスの流体力学的応答と密接に関連していた。これらの結合効果を考慮に入れることにより、適切な境界積分方程式が補足的な理論的関係で定式化された。次に、境界値問題は、高次境界要素法（HOBEM）を使用して解決された。波と動的空力を取得した後、連成運動と流体力学的効率を積分によって評価した。特に、固定 OWC に限定された従来の方法とは異なり、提案された方法は、結合された剛体運動で浮いているものに適用可能であることが証明されていた。したがって、波力吸收を最大化するために、最適なタービンパラメータが数学的に導き出された。線形量に加えて、非線形の波漂流力は、遠場の寄与と内部流体表面上の振動空気圧を説明する、新しく導出された定式化によって評価された。上記の方法論と結果として得られたツールに基づいて、さまざまな浮動型デバイスの数値研究が実行された。

- [1] Cong, P., Teng, B., Bai, W., Ning, D., Liu, Y. (2021). Wave power absorption by an oscillating water column (OWC) device of annular cross-section in a combined wind-wave energy system. *Applied Ocean Research*, 107, 102499.
- [2] Liu, Y., Liang, H., Kashiwagi, M., Cong, P. (2021). Alternative approaches of evaluating Diffraction Transfer Matrix and Radiation Characteristics using the hybrid source-dipole formulation. *Applied Ocean Research*, 114, 102769.

# 國際化推進共同研究報告書

No.

**21RE-6**

タイトル: Predictions of the wave power absorption by a large Floating Oscillating Water Column (OWC) wave energy converter based on a Higher-order Boundary Element (HOBEM) method

研究代表者: CONG, PEIWEN

所内世話人: 劉 盈溢

## Introduction

The ocean is vast and powerful, enabling marine renewable energy to be potentially a significant energy supply. Due to the high power density and longtime availability, considerable efforts and advances have been made in exploiting the power of ocean waves worldwide, and a variety of wave energy converters have been invented to harvest the wave energy. Among different classes of designs, the oscillating water column (OWC) device has been widely regarded as one of the most promising options<sup>[1]</sup>.

In addition to wave energy, wind energy is also a great source of renewable energy. Wind energy converters have been used for the harvesting and exploitation of the available enormous wind energy resources. Offshore wind turbine technology has been being developed rapidly in recent years, and it can be considered as the leading technology in the offshore renewable energy sector<sup>[2]</sup>. For both the offshore wind turbine and the wave energy converter, there is a need for a reduction in the cost and the further development. Due to the natural correlation, wave energy may also be of considerable amount where the offshore wind energy resource is rich. Significant opportunities and benefits have been identified through an integration of the energy systems of different technologies into one single platform. Due to the various possible advantages as a result of the combination of the wind and wave energy converters, several concepts of the combined system have been proposed. Examples include the integration of a point-absorber-type wave energy converter with a semi-submersible type or a spar type wind turbine; integration of an OWC with a floating or bottom-mounted offshore wind turbine, and semisubmersible flap concept.

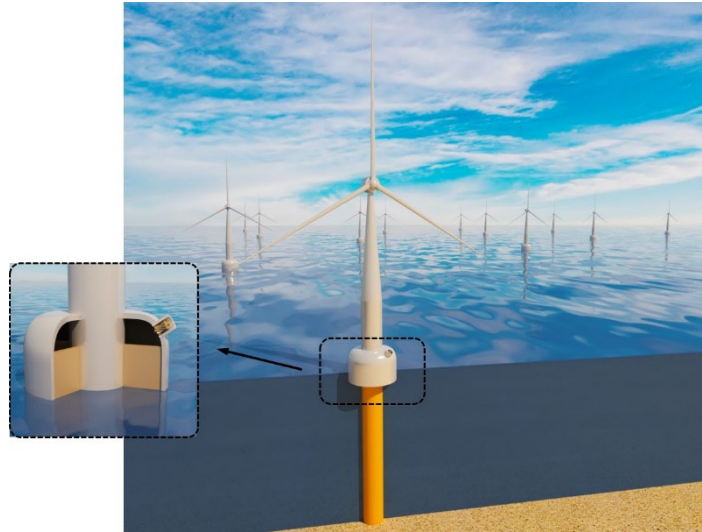


**Fig. 1 Overview of a combined concept consisting of a monopile wind turbine and an attached OWC device**

In this study, a novel combined concept consisting of an oscillating water column (OWC) device and an offshore wind turbine is proposed. As shown Fig. 1, the wind turbine is supported by a monopile foundation, and the OWC is coaxial with the foundation. The OWC is partly submerged with its bottom open to the sea. An air duct, which houses an air turbine, is installed on the roof of the chamber. Within the chamber, the exterior shell of the OWC and the monopile foundation are connected by four vertical stiffening plates. Correspondingly, the whole chamber is divided into four fan-shaped sub-chambers. The performance of the proposed system is then investigated.

## Methodology

### Governing equations

It is assumed that the fluid is inviscid and incompressible with a constant density  $\rho$ , the fluid motion is irrotational, and the wave steepness is small. The linear potential flow theory can then be used, and there exists a velocity potential  $\Phi(\mathbf{x}; t)$  satisfying the Laplace's equation in the fluid domain. That is

$$\nabla^2 \Phi(\mathbf{x}; t) = 0. \quad (1)$$

The combined system is exposed to the action of a plane incident wave of amplitude  $A$ , and frequency  $\omega$ . The wave heading is  $\beta$  with respect to the positive  $x$ -direction. A frequency-domain analysis is conducted, and all time-dependent variables are assumed to be harmonic. The time factor can then be separated, and the velocity potential will have the following form

$$\Phi(\mathbf{x}; t) = \text{Re} \left[ \phi^{(1)}(\mathbf{x}) e^{-i\omega t} \right], \quad (2)$$

in which ‘Re’ is the real part of a complex variable;  $i = \sqrt{-1}$ .

Besides Laplace's equation, the velocity potential must satisfy appropriate boundary conditions. On the

exterior free surface  $S_e$  ( $r \geq R_e$ ), there is only the atmospheric pressure  $P_0$ . However, the inner free surface  $S_i$  ( $a \leq r \leq R_i$ ) is subjected to an air pressure distribution of  $P_0 + P_c(t)$ , in which  $P_c(t)$  is the oscillating air pressure. Due to the high sound speed in air and the low frequency of ocean waves, the oscillating air pressure can be considered spatially uniform throughout the whole chamber<sup>[3]</sup>. Referring to Sarmento and Falcão (1985)<sup>[4]</sup>, after assuming isentropy and using a linear wave theory, the mass flux of the air through a linear turbine is related to the oscillating air pressure by

$$\frac{dM_a}{dt} = \rho_a Q_c - \frac{V_0}{c^2} \frac{dP_c}{dt} = \frac{KD}{N} P_c, \quad (3)$$

in which  $M_a$  is the mass of the air in the chamber;  $Q_c$  is the change rate of the total volume of air inside the chamber;  $V_0$  is the air volume in the chamber in calm water;  $\rho_a$  is the air density;  $D$  is the diameter of the turbine rotor;  $N$  is the speed of the turbine rotation;  $c$  is the speed of the sound in air;  $K$  is an empirical coefficient depending on the design of the turbines. For simple harmonic motions with

$$Q_c(t) = \text{Re}[q_c e^{-i\omega t}]; \quad (4a)$$

$$P_c(t) = \text{Re}[p_c e^{-i\omega t}], \quad (4b)$$

we can have

$$q_c = \Lambda p_c, \quad (5)$$

in which  $q_c$  and  $p_c$  are the amplitudes of the volume flux and the oscillating air pressure, respectively. The parameter  $\Lambda$  is expressed as

$$\Lambda = \chi - i\omega\mu, \quad (6)$$

with

$$\chi = \frac{KD}{N\rho_a}; \quad (7a)$$

$$\mu = \frac{V_0}{c^2 \rho_a}. \quad (7b)$$

$\chi$  depends on the design of the air turbine, and can be adjusted by some ways, such as varying the rotational speed  $N$ .  $\mu$  represents the effect of compressibility of air in the chamber, and is analogous to a spring constant.

### Boundary equations

In the hydrodynamic analysis, the effect of the oscillating air pressure should be considered properly. Then, on the mean plane of the free surface ( $z = 0$ ), the combined kinematic and dynamic boundary condition is given by

$$\frac{\partial \phi}{\partial z} - \frac{\omega^2}{g} \phi = \frac{i\omega}{\rho g} p_c, \quad \text{on } S_i; \quad (8a)$$

$$\frac{\partial \phi}{\partial z} - \frac{\omega^2}{g} \phi = 0, \quad \text{on } S_e. \quad (8b)$$

On the mean wet surface of the combined system  $S_b$ , the boundary condition is given by

$$\frac{\partial \phi}{\partial n} = 0, \quad \text{on } S_b, \quad (9)$$

in which  $\mathbf{n}$  is the normal unit vector pointing outward from the fluid domain. In the same way, the boundary condition on the impermeable sea bed ( $z = -h$ ) is

$$\frac{\partial \phi}{\partial z} = 0, \quad \text{on } z = -h. \quad (10)$$

To ensure the uniqueness of the solution,  $\phi$  has to satisfy the Sommerfeld radiation condition at a substantial distance from the structure. That is

$$\lim_{r \rightarrow \infty} \sqrt{r} \left[ \frac{\partial}{\partial r} (\phi - \phi_l) - i\kappa_0 (\phi - \phi_l) \right] = 0, \quad (11)$$

in which  $\phi_l(\mathbf{x})$  represents the incident velocity potential, and it is given by

$$\phi_l(\mathbf{x}) = -\frac{iAg}{\omega} \frac{\cosh \kappa_0(z+h)}{\cosh \kappa_0 h} e^{i\kappa_0(x \cos \beta + y \sin \beta)}, \quad (12)$$

in which  $\kappa_0$  is the wavenumber.  $\kappa_0$  and  $\omega$  satisfy the relationship  $\omega^2 = g\kappa_0 \tanh \kappa_0 h$ , with  $g$  being the gravitational acceleration.

### **Power take-off model**

The captured power  $W_c$  is the time-averaged rate of work done by the oscillating air pressure pushing the air through the air turbine<sup>[5]</sup>.  $W_c$  can be evaluated according to

$$W_c = \lim_{\hat{T} \rightarrow \infty} \left\{ \frac{1}{\hat{T}} \int_t^{t+\hat{T}} P_c(t) Q_c(t) dt \right\}. \quad (13)$$

For regular incident wave,  $W_c$  can be further expressed as

$$W_c = \frac{1}{2} \operatorname{Re} [p_c q_c^*] = \frac{1}{2} \operatorname{Re} [\Lambda] \|p_c\|^2. \quad (14)$$

Following Cruz (2008)<sup>[6]</sup>, the wave energy extraction efficiency  $E_c$  (also known as the relative capture width) for the present combined system is defined as

$$E_c = \frac{W_c}{W_{in}} = \frac{W_c}{2(R_i - a) P_{in}}, \quad (15)$$

in which  $W_{in}$  is the wave power of the free incident wave passing through the width of  $2(R_i - a)$  over a wave period;  $P_{in}$ , representing the power flux density of the incident wave, is determined according to

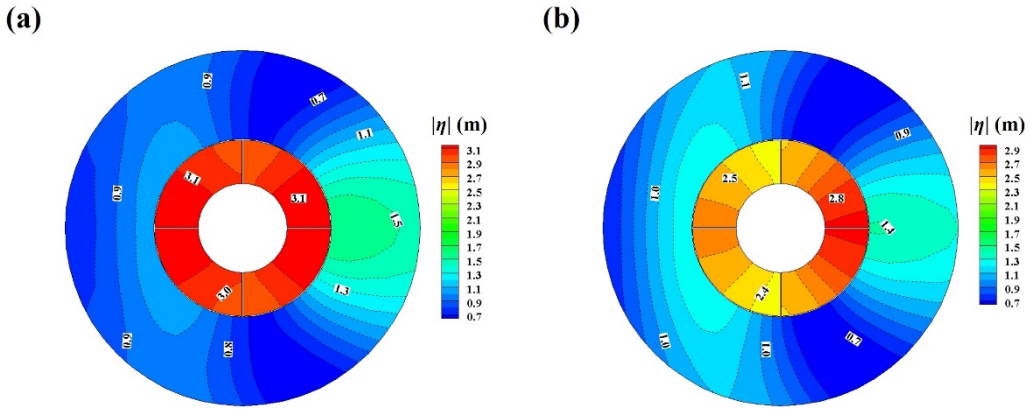
$$P_{in} = \frac{1}{2} \rho g A^2 C_g. \quad (16)$$

In Eq. (16),  $C_g$  is the group velocity of the incident wave.

## Results

The distribution of the wave elevation in the vicinity of the combined system at  $\omega = 1.38$  rad/s is calculated and shown in Fig. 2 with different turbine parameters.  $\chi = +\infty$  corresponds to a condition that the inner free surface open to the air, and the air turbine is removed ( $N = 0$ ). Around  $\omega = 1.38$  rad/s, the total volume flux maximises, and the captured wave power attains a local maximum. In addition, at this frequency, the radiation susceptance vanishes, and the radiation conductance maximises. It suggests that this frequency corresponds to the piston (or pumping) natural frequency of the water column in a moonpool. As a result, when the inner free surface is open to the air, significantly amplified wave elevation is observed at this wave frequency (see Fig. 2(a)). In Fig. 2(a), the distribution of the wave elevation within the whole chamber is almost uniform, and the fluid within the chamber moves like a rigid body. With a decrease of the turbine parameter, more damping effect is applied on the inner free surface, and the wave elevation gradually loses its uniform distribution. Its magnitude varies more and more apparently along the circumferential direction, causing a breakdown of the piston-like motion.

We then examine the effect of the wave heading on the wave elevation in the vicinity of the system. The distribution of the wave elevation amplitude at  $\omega = 1.38$  rad/s is shown in Fig. 3 with  $\beta$  varying from 0 to  $\pi/4$ . Under different wave headings, the wave elevation within each sub-chamber distributes almost uniformly. As  $\beta$  increases, the wave elevation in the upstream and downstream sub-chambers gets enhanced, while in the remaining two sub-chambers, the wave elevation gets gradually less obvious. When  $\beta$  increases to  $\pi/4$ , the distribution of the wave elevation is symmetry with respect to  $\theta = \pi/4$ , and significantly amplified wave elevation can be observed in the downstream sub-chamber.



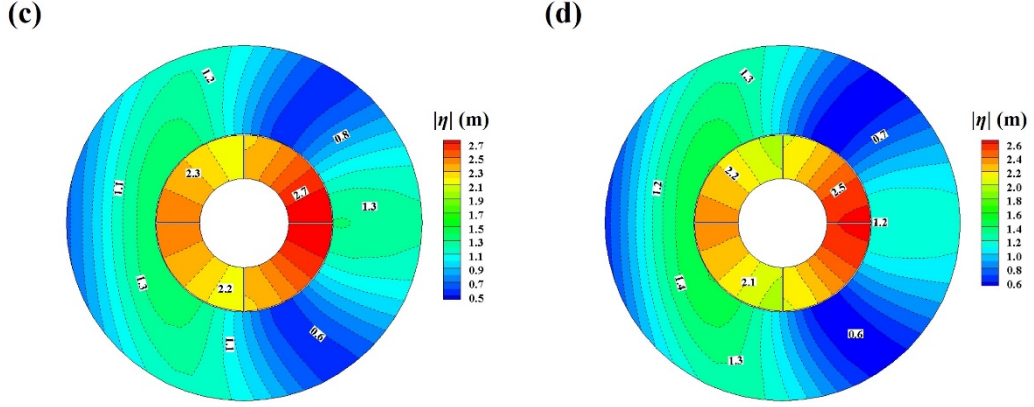


Fig. 2 Distribution of the surface elevation amplitude in the vicinity of the combined system at  $\omega = 1.38$  rad/s with  $R_e = 6$  m,  $d = 3$  m,  $e = 0.06$  m,  $h = 20$  m,  $A = 1$  m, and  $\beta = 0$  for (a)  $\chi = +\infty$ , (b)  $\chi = 2\chi_{opt}$ , (c)  $\chi = \chi_{opt}$ , and (d)  $\chi = 0.5\chi_{opt}$

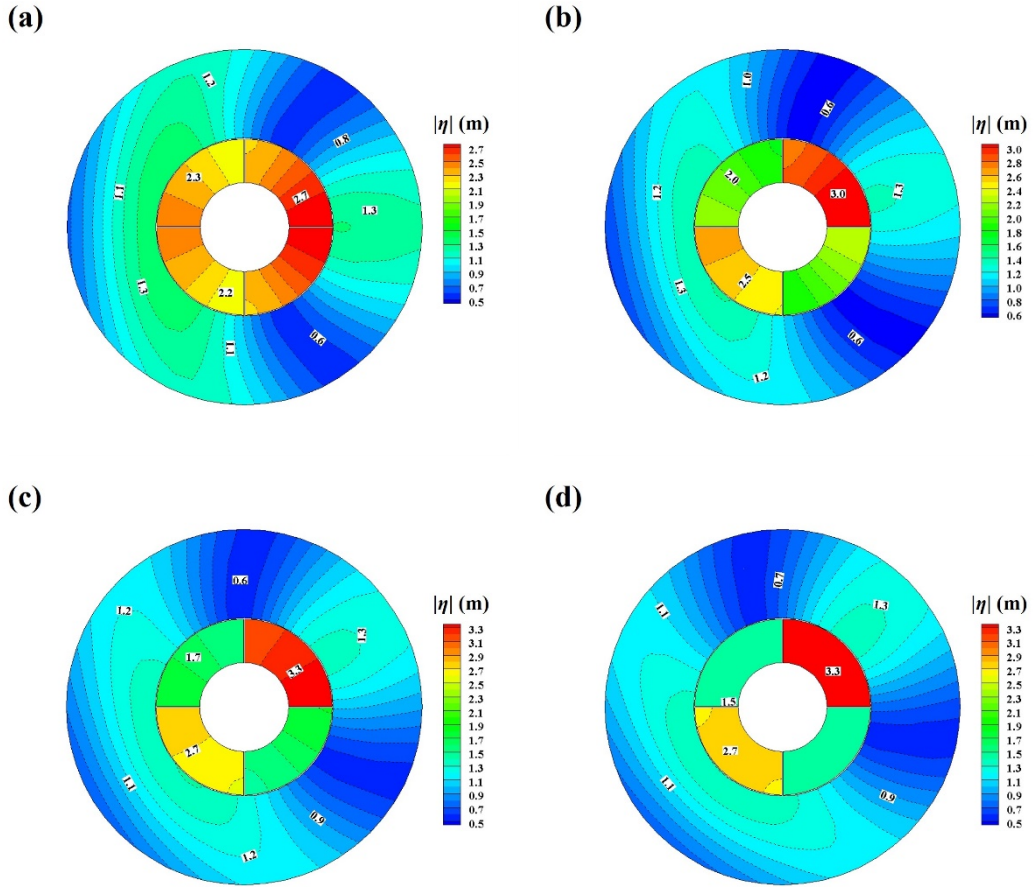


Fig. 3 Distribution of the surface elevation amplitude in the vicinity of the combined system at  $\omega = 1.38$  rad/s with  $R_e = 6$  m,  $d = 3$  m,  $e = 0.06$  m,  $h = 20$  m,  $A = 1$  m, and  $\chi = \chi_{opt}$  for (a)  $\beta = 0$ , (b)  $\beta = \pi/12$ , (c)  $\beta = \pi/6$ , and (d)  $\beta = \pi/4$ .

## References

- [1] Falcão A F de O. Wave energy utilization: A review of the technologies. *Renewable and Sustainable Energy Reviews*, 2010, 14(3): 899-918.
- [2] Heath T V. A review of oscillating water columns. *Philosophical Transactions of the Royal Society London, Series A: Mathematical, Physical and Engineering Sciences*, 2012, 370(1959): 235-245.
- [3] Sarmento A J N A, Falcão A F O. Wave generation by an oscillating surface-pressure and its application in wave-energy extraction. *Journal of Fluid Mechanics*, 1985, 150: 467-485.
- [4] Sheng W A, Alcorn R, Lewis A. On thermodynamics in the primary power conversion of oscillating water column wave energy converters. *Journal of Renewable and Sustainable Energy*, 2013, 5(2): 023105.
- [5] Evans D V, Porter R. Efficient calculation of hydrodynamic properties of OWC-Type devices. *Journal of Offshore Mechanics and Arctic Engineering*, 1997, 119(4): 210-218.
- [6] Cruz J. *Ocean Wave Energy*. 2008, Springer, Berlin, Heidelberg, Germany.

## 国際化推進共同研究概要

No. 17

21RE-7

タイトル : Downwind Turbine Technologies, Model Development and Verification

研究代表者 : HÖNING Leo

所内世話人 : 吉田 茂雄

研究概要 :

ダウンウインドロータは将来の超大型風車および浮体式洋上風車の発電コスト(LCOE)削減に有望な技術である。本研究では、洋上/陸上の風車を含めて、ダウンウインド風車が有効な設計条件を調査する。対象とする研究テーマには、動的応答、荷重、制御、およびLCOEへの影響などを含む。

ダウンウインド風車の空力弹性解析の精度を向上させるために、4つのタワーシャドウモデル、1つのナセルブロックージモデルが開発された。さらに、2MWのベースラインモデルを開発し、各サブタスクに提供された。さらに、フリーヨーアイドリングの評価方法が提案され、実機により検証された。超大型風車に対するダウンウインド風車の利点は、システムエンジニアリングのアプローチを通じて示された。さらに、ダウンウインド風車の革新的な概念が研究され、超大型風車に対するダウンウインド風車の利点が示された。

## **21RE-7 Downwind Turbine Technologies, Model Development and Verification**

Applicant: Leo, Hoening, Fraunhofer Institute for Wind Energy Systems  
RIAM Attendant: Shigeo Yoshida

### **1. OUTLINES**

#### **1.1 Member**

(IWES) Leo Hoening, Bernhard Stoevesandt  
(X1 Wind) Alex Raventos, Rocio Torres  
(NREL) Nick Johnson  
(BWC) Sandy Butterfield  
(UVA) Eric Loth  
(AIST) Tetsuya Kogaki, Shigemitsu Aoki  
(Hitachi) Soichiro Kiyoki, Shigehisa Funabashi, Nobuo Namura  
(WEIT) Masataka Owada, Yoshitaka Totsuka  
(UTokyo) Atsushi Yamaguchi  
(RCCM) Noriki Iwanaga  
(KU RIAM) Shigeo Yoshida

#### **1.2 Outlines of the Task**

WP1) Model Development& Verification

- WP1-1) 2MW Baseline Turbine Model
- WP1-2) Tower Shadow
- WP1-3) Nacelle-Rotor Interaction
- WP1-4) Stability & Control
- WP1-5) Complex Terrain

WP2) Design and LCOE Assessment

- WP2-1) Blade Optimization for DTs
- WP2-2) Scalability Benefits for DTs

WP3) Recommended Practice

- WP3-1) Standards Evaluation for DTs
- WP3-2) RP for DTs

### **2. REPORTS**

#### **WP1-1) Baseline Model, UTokyo**

Aeroelastic models of a 2MW baseline downwind turbine model were defined. The tower was designed to avoid resonance in the operation conditions as shown in Fig 1. The Bladed and FAST models were delivered to the members to proceed the verification study in each research subject.

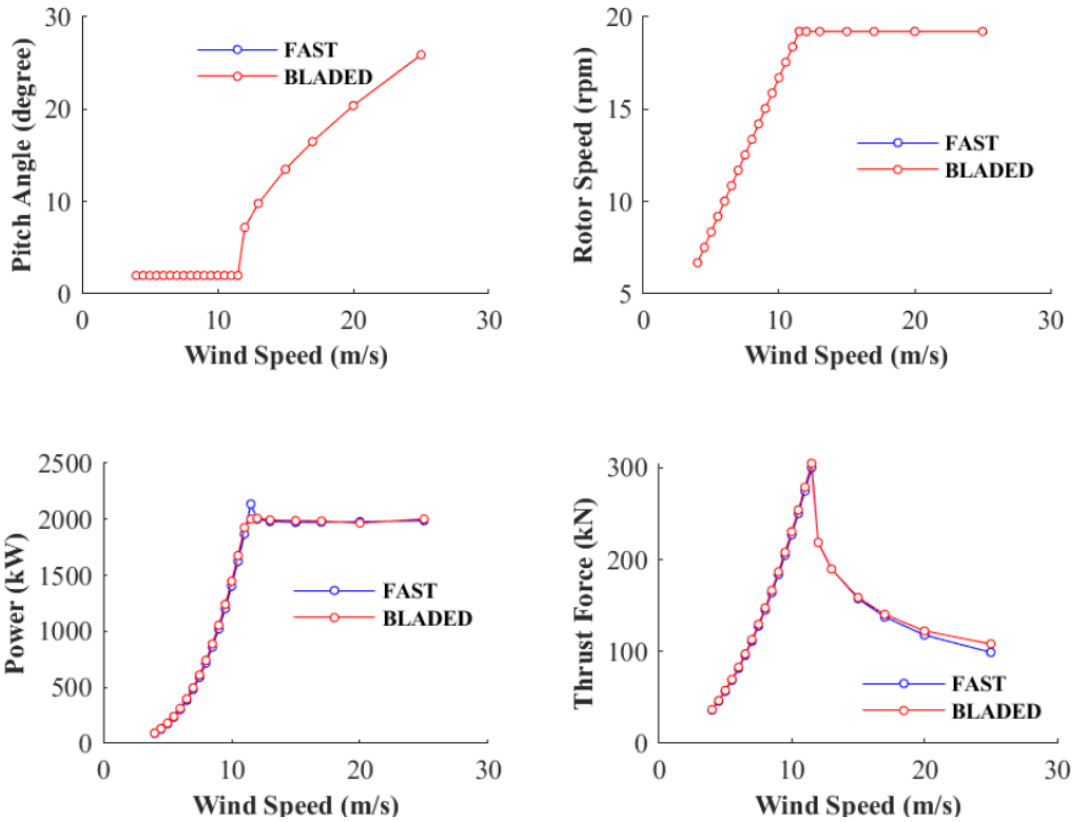


Fig 1 Steady characteristics of aeroelastic models

### WP1-2) CFD Result, IWES

- Model: Hitachi 2MW-80m downwind
- Wind speed: 8.6 m/s (steady)
- Pitch angle: 1.6 deg
- CFD solver: OpenFOAM
- 1/3 domain (steady), full WT (unsteady)
- Number of cells: 16million per blade

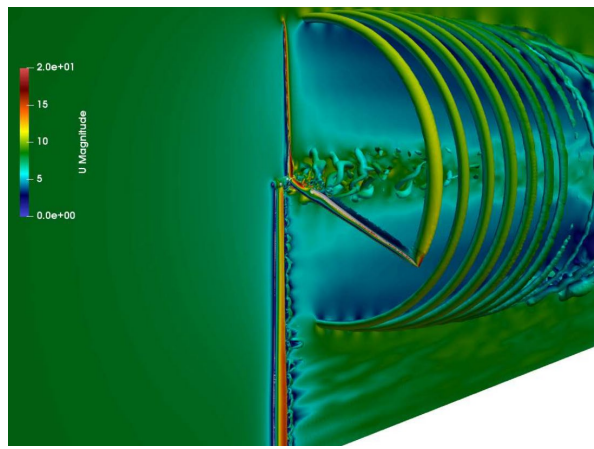


Fig 2 CFD model outline

### WP1-2) Tower Shadow, KU

Some research results on tower shadow modeling of downwind turbines in Blade-Element and Momentum (BEM) method, which was not considered in the former methods were reported.

- (1) Load Equivalent Model [1]

The load equivalent model tower shadow model was introduced. The wind speed profile of the tower wake is defined based on the load fluctuation calculated by the CFD. It showed good agreement with the measurement.

### (2) Tower Variable Load [2]

The variable load model of downwind turbine tower, which was not considered in the previous model, is formulated as below, using lifting-line theory.

$$\Delta C_{dT} = \frac{\pi D_T}{2U_0^2} \left( -U_0 \frac{du}{dx_T} + r\Omega \frac{dv}{dx_T} - w \frac{dw}{dx_T} \right)$$

It was verified by the CFD of rotor-tower-nacelle configurations at rated and cut-out operating conditions. It shows fairly nice agreement with the CFD in particular out-board section and at low thrust conditions as shown in Fig 6. However, there still be some more room for improvement in inboard sections.

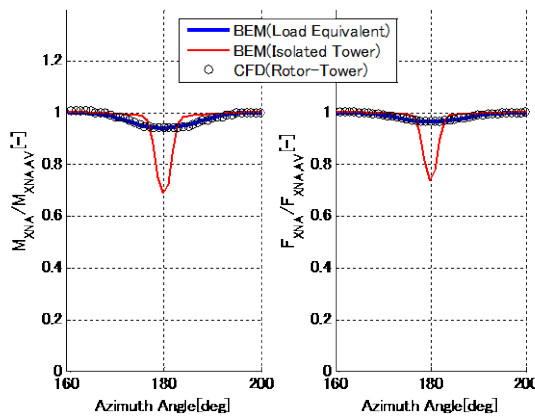


Fig 3 Rotor thrust and torque of a downwind turbine stiff model around the tower shadow at 13 m/s [1]

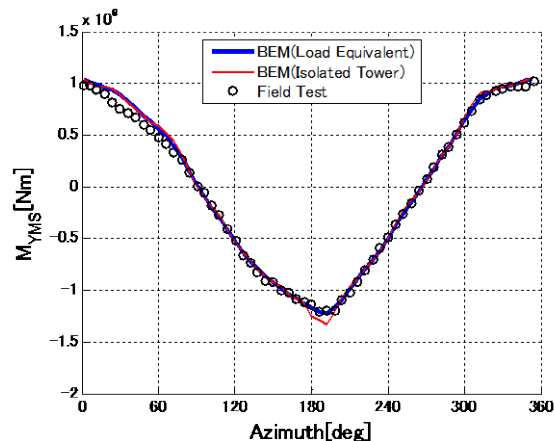


Fig 4 Mainshaft bending a 2 MW prototype downwind turbine at 13 m/s [1]

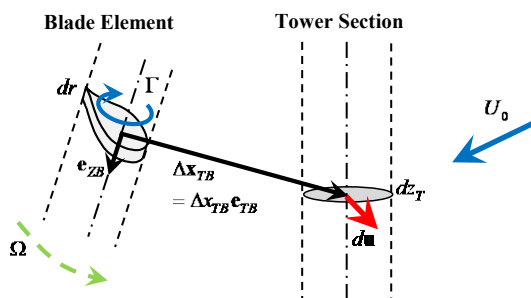


Fig 5 Outlines of the model [2]

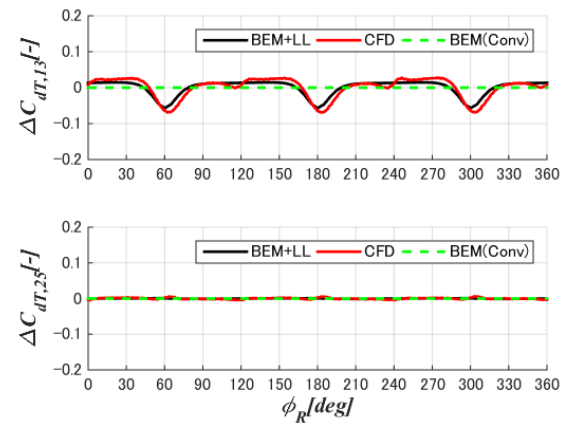


Fig 6 Variable loads of the downwind turbine tower at 100% rotor radius: (T) 13 m/s, (B) 25 m/s [2]

### (3) Tower Average Load [3]

The average tower load model was also introduced based on the momentum theory, which consists with velocity and pressure gradient terms.

$$\begin{aligned} \Delta C_{dTV} &= \Delta C_{dTV} + \Delta C_{dTP} \\ &= -C_{dT0} \left( 1 - \mu_T^2 \right) + \frac{\pi}{2} \mu_T \frac{d\mu_T}{d\xi_T} \end{aligned}$$

The model was validated by the wind tunnel test. It shows good agreement with the wind tunnel test data as shown in Fig 7.

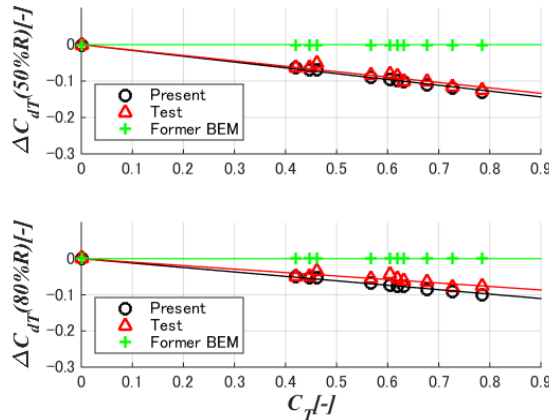


Fig 7 Rotor thrust to tower drag: (T) 13m/s, (B) 25 m/s  
[3]

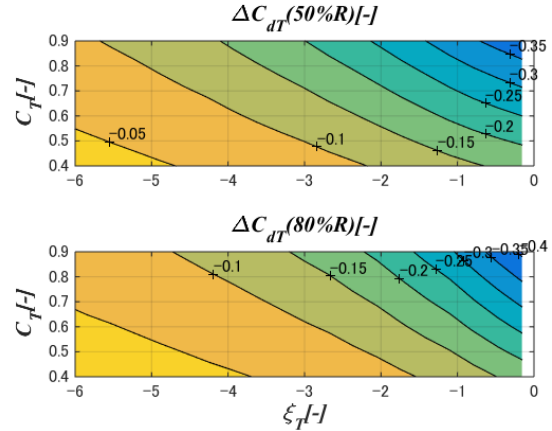


Fig 8 Tower section drag to the rotor thrust and the clearance between the rotor and the tower: (T) 50 %R, (B) 80 %R [3]

#### (4) Dynamic Blade Load [4]

The dynamic blade load model was reported. This model was developed based on the former study of Munduate [5]. Two points were modified from the reference; 1) application of Moriarty's tower wake model [6] and 2) wake entrance condition. Fig 9 shows the analysis and experiment results on a 1.0 m diameter model. Where, UG indicates University Glasgow's former model and KU does present model. The present model was successfully shown the increase in load before the wake entrance was modeled better than the previous work.

The scale effects of the model were investigated. Fig 10 is the simulation results for the similar models. The top, middle and bottom subplots are analysis results with x1 model (1 m rotor diameter), x3 (3 m), and x10 (10m), respectively. Here the tip speeds are set to be identical. As shown in these figures, the variation of the lift coefficients are decreasing as the scale getting larger.

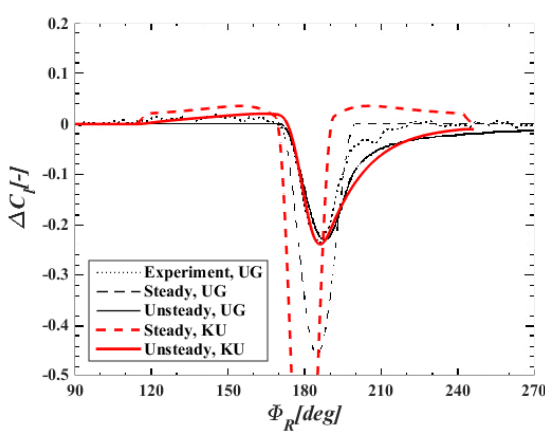


Fig 9 Blade section (75% rotor radius) lift coefficient to rotor azimuth, UG model [4]

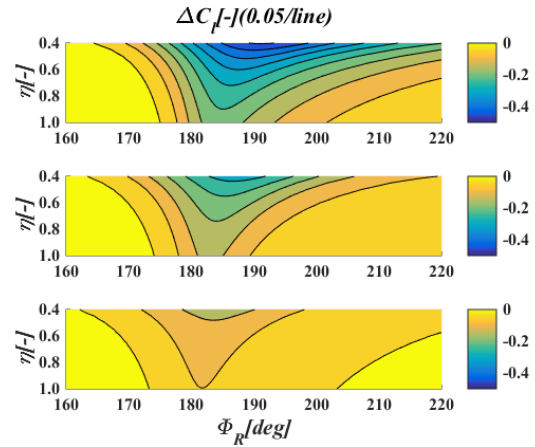


Fig 10 Blade section lift coefficient to rotor azimuth: scale (T) x1, (M) x3, (B) x10, KU model [4]

#### WP1-3) Nacelle Blockage Effect, NREL [7]

##### 1. Outlines

With respect to the three-dimensional effects in the blade-element and momentum (BEM) method, the tip/root effect is one of the most essential considerations because of the edges at the blade tip and root. Although only “loss” has been focused on the root effect, downwind rotors are expected to have stronger blockage effect, that is an

aerodynamic interaction with the nacelle. The nacelle blockage effects on the rotor performance and loads were modeled and verified numerically.

To evaluate the present method, CFD was conducted for typical nacelle shapes shown in Fig 11. Here, “EM” indicates engineering model defined in this section.

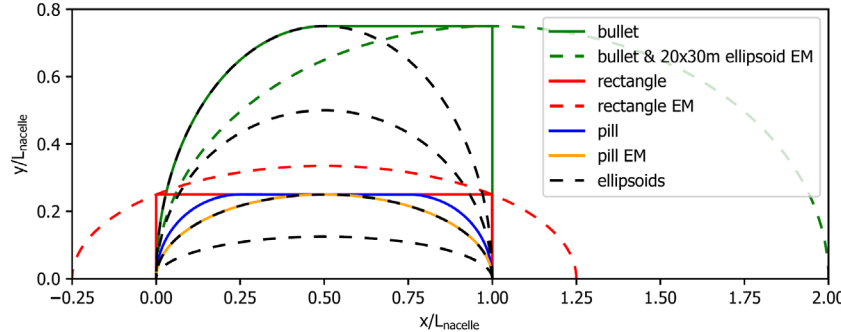


Fig 11 CFD Cases [7]

## 2. CFD Results

The wind speed distributions of typical configurations, 20 m x 30 m bullet and ellipsoid, calculated by CFD are shown in Fig 12. The latter is the EM configuration of the former one. They show similar distributions in the upwind and middle of the bodies.

CFD results for the three nacelle shapes with the three rotor planes are shown in Fig 13. The lines from left to right, are upwind, middle, and downwind respectively. Note: the rectangle EM is wider in the middle.

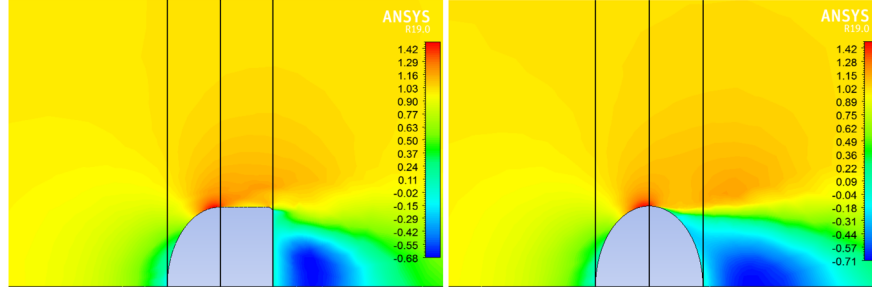


Fig 12 Normalized velocity by CFD around the 20 m x 30 m bullet (left) and ellipsoid (right) nacelles [7]

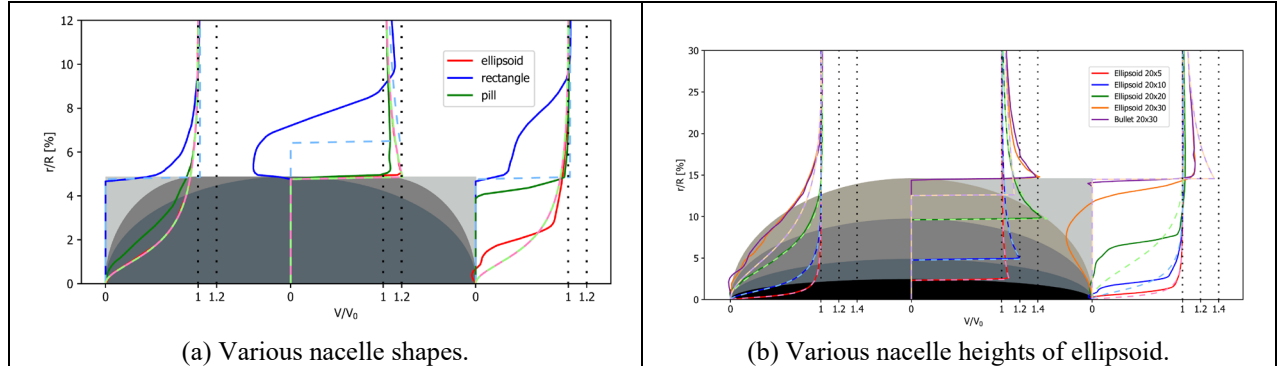


Fig 13 Normalized velocity profiles along rotor planes. Solid, darker lines: CFD results. Dashed, lighter lines: EM results [7]

The relationship between boundary layer height  $BLH$  from CFD, and Reynolds numbers  $Re_L$ ,  $Re_H$ , and aspect ratio of all the nacelles are shown in Fig 14. No correlation is found between  $BLH$  and  $Re$ , though an inverse relationship is found between  $BLH$  and aspect ratio. No correlation is found between maximum speed up and  $Re$ , though an inverse relationship is found between maximum speed up and aspect ratio as shown in Fig 15. No correlation is found between  $C_p$  and  $Re$ , though an inverse relationship is found between  $C_p$  and aspect ratio as

shown in Fig 16.

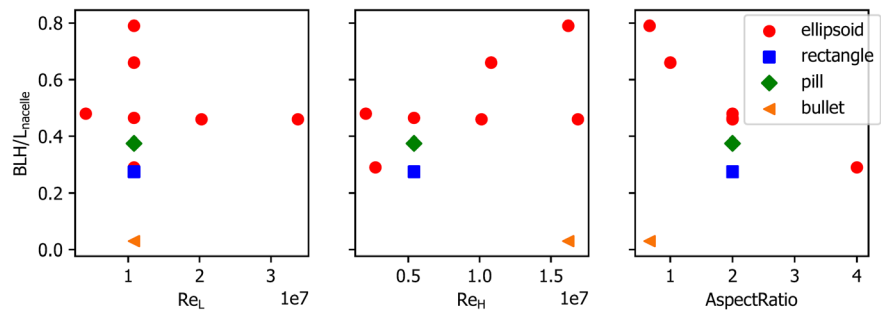


Fig 14  $BLH$  from CFD vs.  $Re_L$ ,  $Re_H$ , and aspect ratio for all nacelles [7]

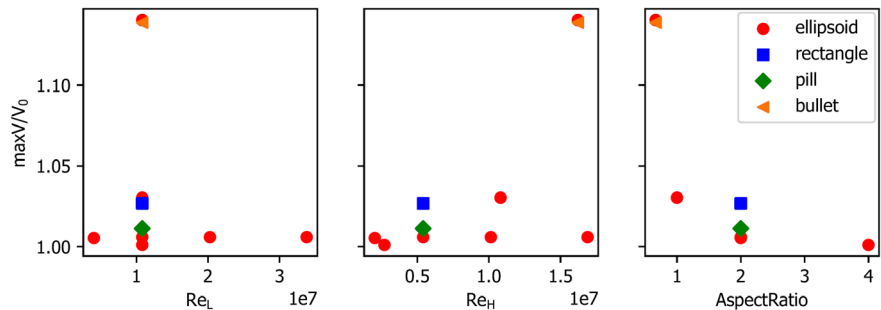


Fig 15 Maximum speed-up from CFD vs.  $Re_L$ ,  $Re_H$ , and aspect ratio for all nacelles [7]

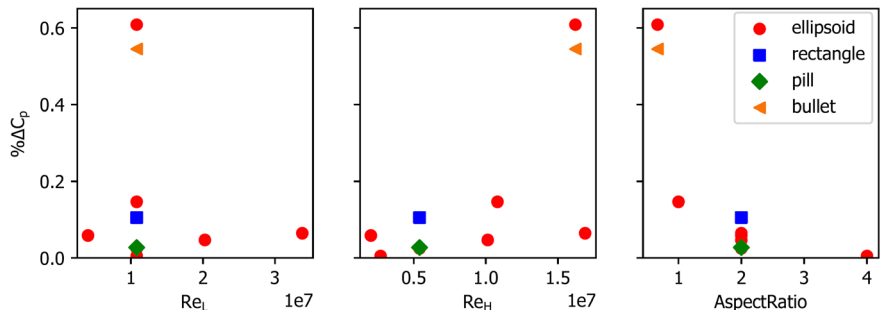


Fig 16 Rotor  $C_p$  in CFD flow field vs.  $Re_L$ ,  $Re_H$ , and aspect ratio for all nacelles [7]

### 3. Conclusions

Nacelle blockage effects on rotor loads and performance were found to be insignificant (<0.5%) for all except low-aspect-ratio nacelles. For all cases studied, nacelle blockage was seen to increase rotor loads and performance. The potential-flow engineering model developed here has negligible (sub-millisecond) computational cost.

The engineering model was validated against CFD, yielding like BEM results, with both models yielding  $C_p$  within 0.7% for all runs. For cases with the most significant blockage effects (20 x 30-m ellipsoid and bullet), the relative error in  $C_p$  between the two models was within 1% and 11%, respectively.

Consider the wind speed distribution induced by the nacelle by CFD or experiment. In cases of the BEM with the wind speed distribution at the rotor plane is determined by simulations or experiments. In cases of the elliptic nacelle, the following model introduced by the potential model is applicable.

#### WP1-4) Stability, Hitachi [8][9]

The extreme loads of a 5.2 MW DT in parked condition in Typhoon #21 in 2017 were simulated. Yaw angles by the measurement and the analysis are shown in Fig 17. Blade root flapwise bending moment are shown in Fig 18. The results are consistent with the measurement.

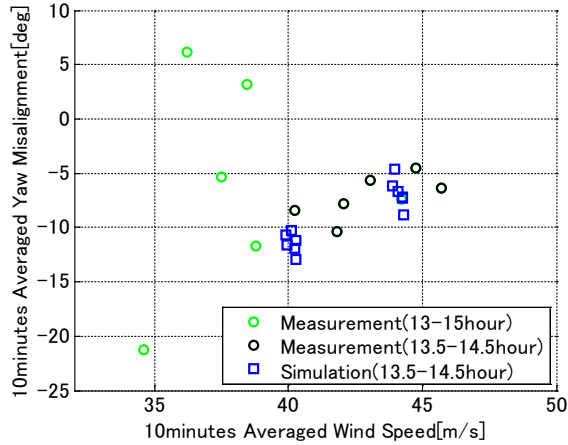


Fig 17 Yaw misalignment to wind speed [8][9]

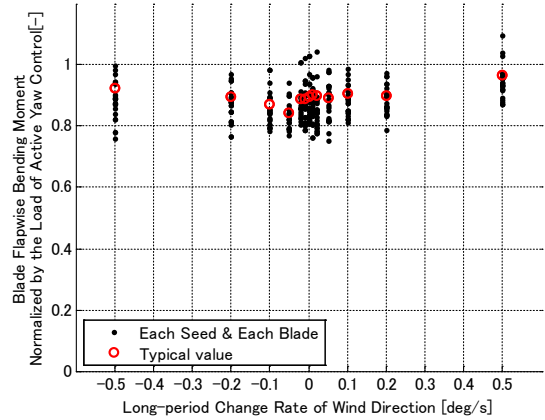


Fig 18 Blade root flapwise bending to wind direction change rate [8][9]

## WP2-2) Scalability Benefits, Hitachi [10]

### 1. Outlines

Fatigue calculation and tower shadow model were introduced in this research. Natural frequencies in flap-wise and edgewise are the output of the optimization. Design variables are not optimized for pre-bent blades as present cost is not considered. Less than 5m is recommended due to the manufacturing and transportation. The tower shadow model is too pessimistic. Therefore, the advantage of downwind turbines is underestimation.

WISDEM, the system engineering code developed by NREL, was modified to consider the tower shadow effect of downwind turbines.

### 2. Conditions

- Wind class: 1A
- Downwind: prebent 0 m
- Upwind-1: prebend max 6 m
- Upwind-2: prebend max 20 m

### 3. Results

Downwind turbine shows lower LCoE than upwind turbines.

Here, the cost of the production and transportation of the prebent blades are still not considered in the cost model of the prebent blades. Therefore, LCoE of the upwind turbines are estimated a little optimistic.

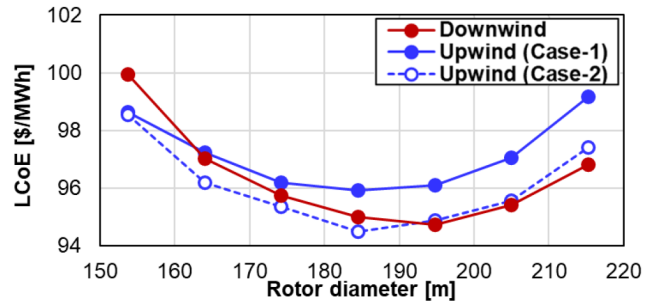


Fig 19 LCoE to rotor diameter [10]

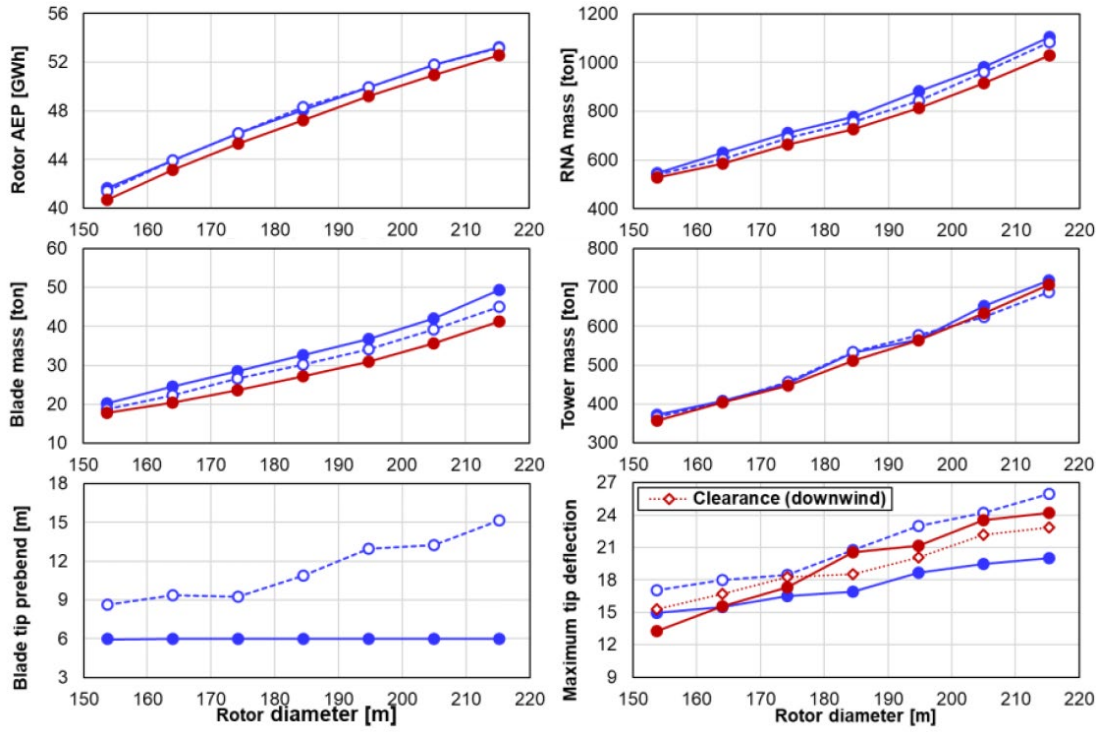


Fig 20 Design parameters to the rotor diameter [10]

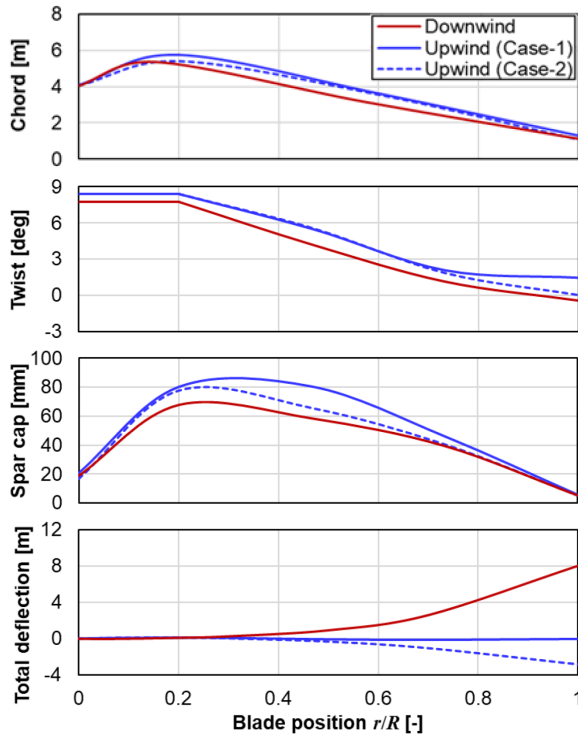


Fig 21 Optimal blade shapes [10]

### WP2-2) Largest Wind Turbine, UVA[11]

Morphing blades, which adapt the alignment of the blade in accordance with the thrust and the centrifugal forces, are promising concept for super large wind turbines.

The studies in SUMR show promising results, such as 27% RNA mass reduction and 24% LCoE reduction, but the fatigue load reduction.

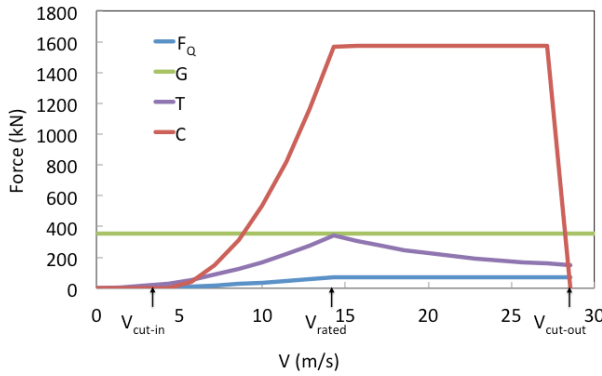


Fig 22 Typical force to wind speed [11]

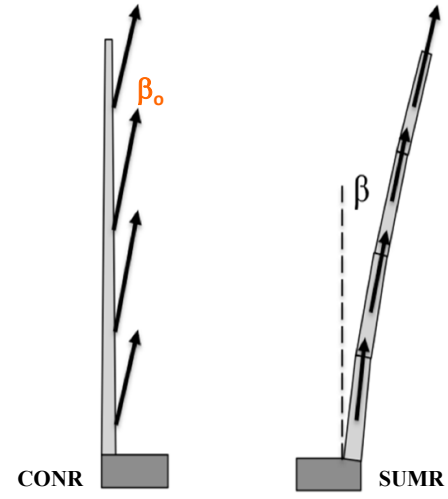


Fig 23 Concept of the SUMR blade [11]

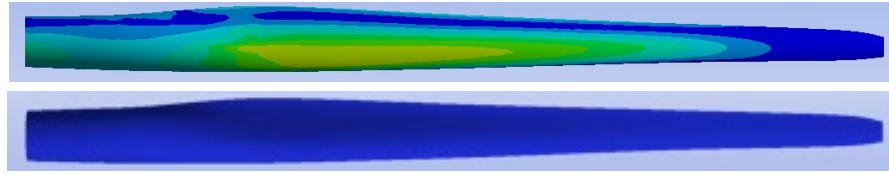


Fig 24 von Mises stress of CONR (top) and SUMR (bottom) [11]

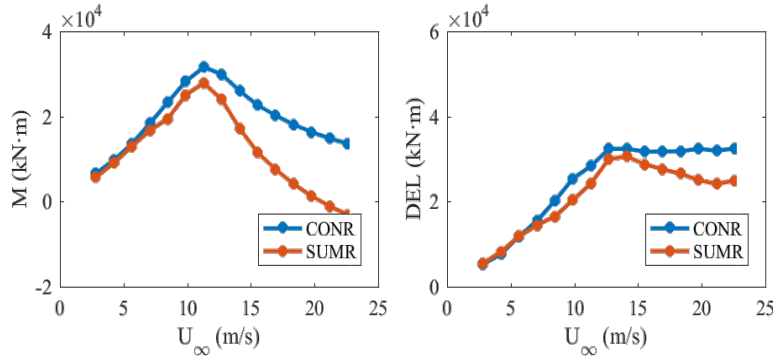


Fig 25 Average moment (left) and its DEL (right) to wind speed [11]

Table 1 Dimensions of the CFD Model [11]

	CONR 3-Blades	SUMR 2-Blades
Rotor Mass	100%	73%
Power Output	100%	98%
LCoE	100%	76%

### 3. REFERENCES

- [1] Yoshida, S., Load Equivalent Tower Shadow Modeling for Downwind Turbines, European Wind Energy Conference, 2007.
- [2] Yoshida, S., Combined Blade-Element Momentum - Lifting Line Model for Variable Loads on Downwind Turbine Towers, energies, 2018.
- [3] Yoshida, S., et al., Effect of Rotor Thrust on the Average Tower Drag of Downwind Turbines, energies, 12, 2, 227-241, 2019.
- [4] Yoshida, S., Dynamic Stall Model for Tower Shadow Effects on Downwind Turbines and Its Scale Effects ,

energies, 1-19, Energies 2020, 13, 5237, 2020.

- [5] Munduate, X., Coton, F.N., Galbraith, R.A.M., An Investigation of the Aerodynamic Responses of a Wind Turbine Blade to Tower Shadow, J. Solar Energy Engineering, 126, 1034-1040, 2004.
- [6] Moriarty, P.J. and Hansen, A.C., AeroDyn Theory Manual, NREL/EL-500-36881, National Renewable Energy Laboratory, 2005.
- [7] Anderson B., Branlard E., Vijayakumar, G., Johnson, N., Investigation of the nacelle blockage effect for a downwind turbine, J. Phys. Conf. Ser. 1618 062062, 2020.
- [8] Kiyoki, S., et al., Evaluation of wind loads by a passive yaw control at the extreme wind speed condition and its verification by measurement, GRE2018, 2018.
- [9] Okuno, A., et al., alidation of Extreme Loads of Wind Turbine by Measurement Data and Simulation, JWEA Wind Energy Utilization Symposium 2018.
- [10] Namura, N., Shinozaki, Y., Design Optimization of 10MW Downwind Turbines with Flexible Blades and Comparison with Upwind Turbines, J.Phys.: Conf. Ser. 1618 042021, 2020.
- [11] Noyes, C., et al., Analytic analysis of load alignment for coning extreme - scale rotors, Wind Energy, 2020:23:357-369, 2020.

## 国際化推進共同研究概要

No. 18

21RE-8

タイトル： Analysis of Multi-Rotor System Wind Turbines

研究代表者： ISMAIEL Amr Mohamed Metwally

所内世話人： 吉田 茂雄

研究概要：

マルチロータシステム（MRS）風車は、コストと品質が比較的成熟した風車が使用できることと、構造上・輸送上のメリットのため、将来の超大型風車のコンセプトとして有望視されている。MRS の荷重計算のための空力弾性ツールを開発している。このツールは、シングルロータ風車に関して、既存の空力弾性ツール FAST で検証した後に、ロータ数 2~4 個の MRS について検討した。検討の結果、固有振動数が非常に重要であることを確認した。また、3 ロータと 4 ロータの MRS のタワー動的応答を比較することにより、4 ロータが、より技術的に実現可能であることが示された。

# RIAM International Joint Research

## General Information

**Grant No.** 18 21RE-8

**Title:** Analysis of Multi-Rotor System Wind Turbines

**Name of the research representative:** Assist. Prof. ISMAIEL, Amr Mohamed Metwally

**Affiliation:** Future University in Egypt (FUE)

**Email:** [amr.mohamed@fue.edu.eg](mailto:amr.mohamed@fue.edu.eg)

**Research subject field:** Renewable Energy

**Name of RIAM attendant:** Prof. Shigeo YOSHIDA

## Abstract:

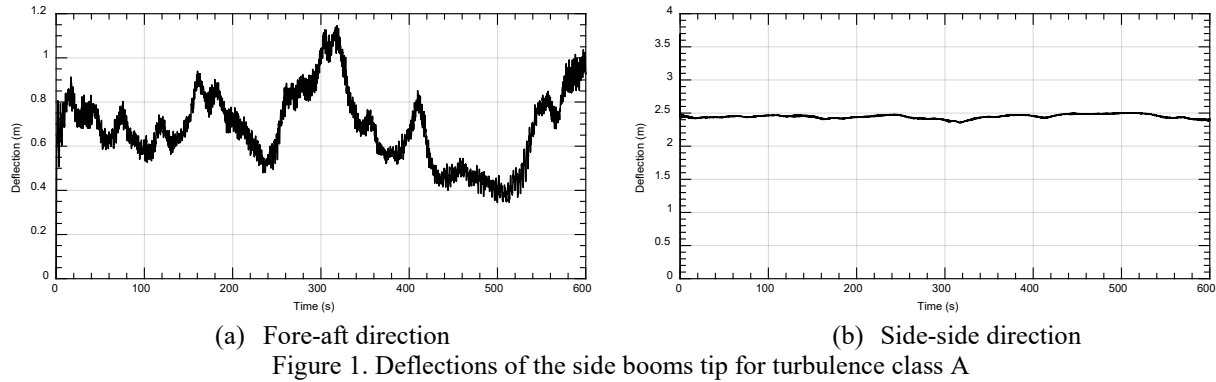
Multi-Rotor System (MRS) wind turbines can be a good alternative to large-scale wind turbines in terms of structural and logistic advantages. An in-house tool was developed in order to analyze the support structure of MRS wind turbines. The tool was verified by comparing the results of a single-rotor wind turbine to an equivalent analysis using the software tool FAST. Then, three different configurations of MRS were studied: including two, three, and four rotors. The tower dynamics were calculated for the main tower in each configuration, as well as the side-booms supporting the two rotors in the twin-rotor configuration. The analyses have shown that the natural frequencies are of big importance and are dominant over the loading regarding the tower dynamics. It has also shown that by comparing the tower dynamics of three and four-rotor configurations, the four-rotor configuration is more technically feasible. In the future, some of the assumptions which were used in developing the code will be removed, in order to get more realistic results and be able to analyze the wind turbine over all ranges of wind speeds.

## Research outcomes:

This research is an extension to a PhD thesis made by the research representative. In the PhD phase, aeroelastic analysis has been made for a twin-rotor configuration and compared to a single rotor which has been verified numerically [1].

As an extension, analysis for the side booms holding the rotors on the T-shaped tower has been conducted. Deflections of the side-boom tip in the fore-aft (Out of plane) and in the side-side (In plane) has been calculated for different turbulent wind fields of classes A, B, and C. Figure 1 shows the deflections for wind turbulence class A. Different diameters for the side booms were studied to determine the relation between the boom size and its structural behavior.

It was found that in the in-plane deflections are dominated by the weight of the rotors, regardless of the turbulence of the wind field, the deflection kept almost a constant value. While the out-of-plane deflections were dominated by the random behavior of the aerodynamic loads in the turbulent wind field and induced high, unfavorable vibrations. It was also found that the bending stiffness of the side-booms is directly proportional to its diameter and has a second-order relation with the mean deflection value [2].



The results of this work have also emphasized that the tower natural frequencies are dominant over the loads in regards of the tower dynamic responses, and hence the importance of the natural frequencies.

## Future Approach

In order to have a better judgment on the feasibility of the three-rotor compared to four-rotor wind turbines, more analyses should be conducted. Pitch control should be added and then compare different wind loads in the high-power region. Power output and cost of energy should also be taken into consideration for comparison.

Wind tunnel experiments and parametric analysis on the rotor spacing will be a great contribution to the field. Machine learning approach can be adopted to find an optimum rotor spacing for better performance.

## References

- [1] A. Ismaiel and S. Yoshida, "Aeroelastic Analysis of a Co-Planar Twin Rotor Wind Turbine," *Energies*, vol. 12, p. 1881, 2019.
  - [2] A. Ismaiel and S. Yoshida, "Aeroelastic Analysis for Side-Booms of a Coplanar Twin-Rotor Wind Turbine," *International Journal of Aerospace Engineering*, vol. 13, no. 4, pp. 135-140, 2020.